Characterization and loss analyses of passivated emitter and rear cells

Von der Fakultät für Mathematik und Physik
der Gottfried Wilhelm Leibniz Universität Hannover

zur Erlangung des akademischen Grades
Doktor der Naturwissenschaften
Dr. rer. nat.

genehmigte Dissertation von

M.Sc. Christian Nikolaus Kruse

2020

Referent:	Prof. Dr. Rolf Brendel
Korreferenten:	Prof. Dr. Rolf J. Haug
	Prof. Dr. Armin G. Aberle
Tag der Promotion:	13.07.2020

Abstract

This work presents characterization methods and simulation-based loss analyses for passivated emitter and rear (PERC) solar cells. Furthermore, it discusses possible ways of introducing poly-Si on thin inter-facial oxides (POLO) junctions into industrial solar cells.

Achieving a further efficiency increase of industrial PERC cells is becoming more and more difficult because the margin to the theoretical limit is reduced step by step. Identifying the major loss channel in terms of a potential efficiency gain, thus, plays an increasingly important role in solar cell optimization. The free energy loss analysis (FELA) [1] and the synergistic efficiency gain analysis (SEGA) [2, 3] as simulation-based loss analyses can address this task. The basis for both the FELA and the SEGA are numerical device simulations based on experimentally determined input parameters. The determination of most of these input parameters can be achieved with measurement and data analysis tools, which are commonly used in PV-research. The recombination at local metal contacts, however, has not been studied to the same extent and standard techniques do not apply.

In this work, we study the determination of contact recombination parameters. We first analyze the required sample structures and develop an analytical model to calculate the length scale on which regions of different charge carrier lifetimes affect each other. We find that a metallization pattern with three metallized and one non-metallized quarters fits our requirements best. In the analysis of suitable measurement setups we find that photoconductance-calibrated photoluminescence imaging is best suited because of the low uncertainty. For the extraction of contact recombination parameters we study the analytical model by Fischer and find an excellent agreement of better than 5% deviation with numerical device simulations, provided the assumptions of low level injection and either full line or periodic point contacts are fulfilled. For arbitrary contact layouts and for the full injection dependence we introduce an approach based on numerical device simulations. In this context, we develop a new model for injection dependent contact recombination currents. The model is based on the superposition of recombination at the Si-metal interface and within the highly doped layer underneath.

We use standard measurement and evaluation techniques and determine contact recombination parameters to perform a complete characterization of a PERC cell batch. In this characterization we determine all input parameters required for a SEGA along with the respective uncertainties. From the uncertainties of the input parameters we determine the uncertainties of the SEGA results using a Monte-Carlo simulation. We also analyze the differences between SEGA and FELA and introduce a graphical user interface for automatic SEGA simulations.

Finally we discuss different cell structures for integrating POLO junctions into industrial solar cells by means of SEGA simulations and hypothetical process flows. We identify cells featuring conventional screen-printed Al base contacts and n-type POLO (n-POLO) junctions as promising candidates for industrial integration in the near fu-

ture. A further development step are solar cells with POLO junctions for both polarities, which show an absolute efficiency benefit between 0.3% and 0.4% compared to similar cells with Al base contacts. However, further research in structuring POLO layers and screen-printed contacting of *p*-type POLO (p-POLO) is required. From the SEGA simulations and the hypothetical process flows a cell development roadmap was derived, in order to focus research activities on the most promising cell concepts.
Keywords: Silicon solar cells, loss analysis, device modeling

Zusammenfassung

Diese Arbeit präsentiert Charakterisierungsmethoden und SEGA Analysen (engl. synergistic efficiency gain analysis) für PERC Zellen (engl. passivated emitter and rear cells). Darüber hinaus wird die Einführung von POLO (engl. poly silicon on oxide) Schichten in industrielle Solarzellen diskutiert.

Eine weitere Leistungssteigerung von industriellen PERC-Zellen wird zunehmend anspruchsvoller, da der Abstand zum theoretischen Wirkungsgradlimit Schritt für Schritt reduziert wird. Die Identifizierung der vielversprechendsten Zellmerkmale im Hinblick auf einen potenziellen Effizienzgewinn spielt daher eine immer wichtigere Rolle bei der Solarzellenoptimierung. Die FELA (engl. free energy loss analysis) und die SEGA als simulationsbasierte Verlustanalysen können die Zellentwicklung bei dieser Aufgabe unterstützen. Die Grundlage für FELA und SEGA sind numerische Halbleitersimulationen, die auf experimentell bestimmten Eingangsparametern basieren. Die Bestimmung der meisten dieser Eingangsparameter kann mit etablierten Charakterisierungsmethoden erfolgen. Für die Rekombinationsrate an lokalen Metallkontakten gibt es jedoch kein Standardverfahren.

In dieser Arbeit untersuchen wir die Bestimmung von Kontaktrekombinationsparametern. Zuerst analysieren wir die erforderlichen Probenstrukturen und entwickeln ein analytisches Modell, um den Längenmaßstab zu berechnen, auf dem sich die Bereiche unterschiedlicher Lebensdauern gegenseitig beeinflussen. Wir stellen fest, dass ein Metallisierungsmuster mit 3 metallisierten und einem nicht metallisierten Viertel am besten zu unseren Lebensdauerproben passt. Bei der Analyse geeigneter Messverfahren stellen wir fest, dass die PC-PLI (engl. photo conductance calibrated photoluminescence imaging) aufgrund der geringen Unsicherheit am besten geeignet ist. Für die Extraktion von Kontaktrekombinationsparametern untersuchen wir das analytische Modell von Fischer und finden eine ausgezeichnete Übereinstimmung von unter 5% im Vergleich zu numerischen Halbleitersimulationen, vorausgesetzt, die Annahmen der Niedriginjektion und von durchgehenden Linien- oder periodischen Punkt-Kontakten sind erfüllt. Für beliebige Kontaktlayouts und zur Analyse der vollständigen Injektionsabhängigkeit der Kontaktrekombination führen wir eine Methode zur Bestimmung der Kontaktrekombination ein, die auf Halbleitersimulationen basiert. In diesem Kontext entwickeln wir ein neues Modell zur Beschreibung der injektionsabhängigen Kontaktrekombination, das auf der Überlagerung der Rekombinationsströme am Metall und innerhalb der hochdotierten Schicht darunter basiert.

Wir wenden die Techniken zur Bestimmung der Kontaktrekombination zusammen mit Standardmess- und Auswertetechniken für eine vollständige Charakterisierung einer PERC-Zellcharge an. In dieser Charakterisierung bestimmen wir alle für eine SEGA erforderlichen Eingangsparameter mit den entsprechenden Unsicherheiten. Aus den Unsicherheiten der Eingangsparameter ermitteln wir mit Hilfe einer Monte-Carlo-Simulation die Unsicherheiten der SEGA-Ergebnisse. Wir analysieren außerdem die Unterschiede zwischen SEGA und FELA und stellen eine grafische Benutzeroberfläche für automatische SEGA-Simulationen vor.

Abschließend diskutieren wir verschiedene Zellstrukturen zur Integration von POLO-Schichten in industrielle Solarzellen mittels SEGA-Simulationen und hypothetischen Prozessflüssen. Wir identifizieren Zellen mit konventionellen, siebgedruckten Al Kontakten und *n*-Typ POLO Schichten als vielversprechende Kandidaten für eine industrielle Integration in naher Zukunft. Ein weiterer Entwicklungsschritt sind Solarzellen mit POLO-Kontakten für beide Polaritäten, die im Vergleich zu ähnlichen Zellen mit Al Kontakten einen Wirkungsgradvorteil zwischen 0,3% und 0,4% aufweisen. Für diese Konzepte ist allerdings weitere Forschung zur Strukturierung von POLO-Schichten und zur siebgedruckten Kontaktierung von *p*-Typ POLO erforderlich. Aus den SEGA-Simulationen und den hypothetischen Prozessabläufen wurde eine Zellentwicklungsstrategie abgeleitet, um die Forschungsaktivitäten auf die vielversprechendsten Zellkonzepte zu fokussieren.
Schlagwörter: Silizium Solarzellen, Verlustanalyse, Bauteilsimulation

Contents

Acronyms

Al-BSF	Aluminum back surface field
AM1.5g	Air mass 1.5 spectrum according to the IEEE 60904-3 standard
ARC	Anti reflection coating
BJ	Back junction
BSF	Back surface field
CCD	Charge-coupled-device
CoBo	Conductive boundary model
Cz	Czochralski-grown
EL	Electroluminescence
FCA	Free carrier absorption
FELA	Free energy loss analysis
FJ	Front junction
FRC	Front and rear contacted cell
FSF	Front surface field
GUI	Graphical user interface
IBC	Interdigitated back contact
ILM	Infrared lifetime mapping
IR	Infrared
ISFH	Institute for solar energy research Hamelin
I-V	Current-Voltage
LCO	Laser contact opening
LED	Light emitting diode
LIA	Local impact analysis
n-POLO	Donator doped poly-silicon on oxide
PC-PLI	Photoconductance-calibrated photoluminescence imaging
PERC	Passivated emitter and rear cell
PERC+	Passivated emitter and rear cell with local rear side metallization
PERT	Passivated emitter and rear totally diffused cell
PL	Photoluminescence
PLI	Photoluminescence imaging
POLO	Poly-silicon on oxide

p-POLO	Acceptor doped poly-silicon on oxide
PV	Photovoltaics
QFL	Quasi-Fermi level
QSSPC	Quasi-steady-state photoconductance
SEGA	Synergistic efficiency gain analysis
SRH	Shockley-Read-Hall
SRV	Surface recombination velocity
SSPC	Steady-state photoconductance
STC	Standard testing conditions according to the IEEE 60904-3 standard
TLM	Transfer length method
TOPCon	Cell structure: "Tunnel oxide passivated contacts" with *n*-type poly-Si and a boron emitter

Symbols

α	Photon absorption coefficient
B_{rad}	Proportionality factor for radiative recombination
β	Inverse thermal voltage
C_{n}	Proportionality factor for the Auger process involving two electrons
C_{p}	Proportionality factor for the Auger process involving two holes
D	Diffusion constant
d	Contact width
d_{geom}	Geometrical contact width
d_{f}	Front contact width
d_{LCO}	LCO dash length
d_{opt}	Optical contact width
d_{r}	Rear contact width
d_{se}	Selective emitter width
Δn	Excess carrier density
$\Delta\phi$	Quasi Fermi level splitting
ΔV	Difference of two internal voltages
E_{G}	Band gap energy
E_{n}	Equality number for the comparsion of values with uncertainties
ϵ_0	Vacuum permitivity
ϵ_r	Material permitivity
$\dot{F}$	Free energy rate
$\dot{F}_{\mathrm{G}}$	Rate of generated free energy
$\dot{F}_{\mathrm{O}}$	Rate of free energy lost due to optical effects
$\dot{F}_{\mathrm{R}}$	Rate of free energy lost due to recombination
$\dot{F}_{\mathrm{T}}$	Rate of free energy lost due to charge carrier transport
f_{met}	Metalized area fraction
f_{opt}	Ratio between optical and geometrical front contact width
FF	Fill factor

g	Generation rate of excess charge carriers due to incident photons
η	Energy conversion efficiency
I_{PL}	Intensity of photoluminescence emission
iV_{OC}	Implied open circuit voltage
J_0	Saturation current density
$J_{0,\mathrm{Ag}}$	Saturation current density of silver contacts
$J_{0,\mathrm{Al}}$	Saturation current density of aluminum contacts
$J_{0,\mathrm{cont}}$	Saturation current density of metalized surfaces
$J_{0,\mathrm{e}}$	Saturation current density of the emitter
$J_{0,\mathrm{e,sel}}$	Saturation current density of the selective emitter
$J_{0,\mathrm{eff}}$	Effective saturation current density
$J_{0,\mathrm{pas}}$	Saturation current density of passivated surfaces
J_{Gen}	Photo-generated current density
J_{rec}	Recombination current density
J_{SC}	Short circuit current density
j_e	Local electron current
j_h	Local hole current
k	Recombination asymmetry factor
L_{D}	Diffusion length
L_{T}	Transfer length
Λ_{b}	Rear side lambertian factor
Λ_{f}	Front side lambertian factor
λ	Photon wavelength
μ_n	Electron mobility
μ_p	Hole mobility
N_{A}	Acceptor concentration
N_{D}	Donator concentration
N_{dop}	Dopant (acceptor or donator) concentration
n	Electron density
n_i	Intrinsic carrier concentration
ν	Real part of the refractive index
P	contact pitch
P_{f}	Front contact pitch
P_{LCO}	LCO dash pitch
P_{r}	Rear contact pitch
p	Hole density
ϕ_{el}	Electrostatic potential
ϕ_{n}	Electron quasi Fermi level
ϕ_{p}	Hole quasi Fermi level
q	Elementary charge
R	Resistance

R_{sheet}	Sheet resistance
$R_{\mathrm{sheet,e}}$	Sheet resistance of an emitter
$R_{\mathrm{sheet,e,sel}}$	Sheet resistance of a selective emitter
R_{series}	Series resistance
R_{spread}	Spreading resistance
$\mathcal{R}$	Reflectance
$\mathcal{R}_{\mathrm{b}}$	Rear-side reflectance
$\mathcal{R}_{\mathrm{f}}$	Front-side reflectance
$\mathcal{R}_{\mathrm{m}}$	Reflectance at Si-metal interface
r	Recombination rate
r_{Auger}	Recombination rate due to Auger recombination
r_{rad}	Recombination rate due to radiative recombination
r_{SRH}	Recombination rate due to Shockley-Read-Hall recombination
ρ	Resistivity
ρ_{b}	Resistivity of the silicon bulk
ρ_{c}	Contact resistivity
$\rho_{\mathrm{c,Ag}}$	Contact resistivity of a silver contact
$\rho_{\mathrm{c,Al}}$	Contact resistivity of an aluminum contact
$\rho_{\mathrm{l,Ag}}$	Line resistance of a silver finger
S	Surface recombination velocity
S_{cont}	Surface recombination velocity of metallized areas
S_{eff}	Effective surface recombination velocity
S_{front}	Surface recombination velocity of front surfaces
S_{pas}	Surface recombination velocity of passivated surfaces
S_{rear}	Surface recombination velocity of rear surfaces
σ_{L}	Light induced conductivity
σ_{n}	Electron conductivity
σ_{p}	Hole conductivity
T_{f}	Front side transmittance
τ	Carrier lifetime
τ_{Auger}	Carrier lifetime due to Auger recombination
τ_{bulk}	Carrier lifetime in the silicon bulk
τ_{eff}	Effective carrier lifetime
τ_{n0}	Minority carrier lifetime of a mid-gap Shockley-Read-Hall defect
τ_{p0}	Majority carrier lifetime of a mid-gap Shockley-Read-Hall defect
τ_{rad}	Carrier lifetime due to radiative recombination
τ_{SRH}	Carrier lifetime due to Shockley-Read-Hall recombination
τ_{surface}	Carrier lifetime due to surface recombination

V	Quasi Fermi level splitting or internal voltage
V_{OC}	Open-circuit voltage
V_{T}	Thermal voltage
W	Cell or sample thickness
$\vec{x}$	Position within the cell or sample
x_{c}	Coupling length between regions of different lifetime

Introduction

In 2019 industrial p-type silicon passivated emitter and rear cells (PERC) achieved record conversion efficiencies of over 24% [4]. The conversion efficiencies for inline production are around 22.5% [5] in 2018 with a learning curve of about 0.5% per year over the last few years [6]. The efficiency learning curve and reduced prices due to large-scale production translate to average module prices of 0.24 $US/Wp in 2018 [5]. The high conversion efficiency in combination with low production costs due to a lean process flow [6] make the PERC concept the main technology for new production lines nowadays. PERC has reached a market share of 35% in 2018 and is expected to reach a market share of 50% in 2019 [5]. Continuing on the 0.5% per year efficiency-learning curve gets, however, increasingly difficult because the efficiency gap to the theoretical efficiency limit of 29.56% [7] gets smaller. Therefore, and because research capabilities are limited, it is crucial to identify the most promising parts of the solar cell for improving the efficiency.

The ideal values for the short-circuit current density J_{SC}, the open-circuit voltage V_{OC} and the fill factor FF are 43.36 mA/cm^2, 763.3 mV and 89.31% for a single junction silicon solar cell with only intrinsic losses [7], respectively. The deviation of the measured I-V parameters to these ideal values gives a first impression on whether the cell is limited by optical performance (low J_{SC}), charge carrier recombination (low V_{OC}) or resistive properties (low FF). However, this approach does not reveal relative magnitudes between the power losses. In addition, the effects on the I-V parameters are not independent from each other. For example, a reduced charge carrier generation rate due to optical effects leads to reduced J_{SC} and V_{OC}, charge carrier recombination leads to a reduction of V_{OC} and FF and high series resistances can lead to a reduction in J_{SC} along with the FF reduction. Therefore, a more detailed break-down of power losses is desirable.

The synergistic efficiency gain analysis (SEGA) and the free energy loss analysis (FELA) are both simulation-based approaches for a breakdown of power losses in solar cells, which yield results in the same unit of measure (power per area) for all present loss channels. Using device simulations for analyzing power losses has the benefit that all aspects of cell operation (eg. spatially resolved current flows and generation) are taken into account and their respective impact on the I-V parameters can be calculated. The simulations are usually based on experimentally determined input parameters, which describe, for example, resistances and defect recombination of excess charge carriers. The determination of most of these parameters can be achieved with techniques that are well-established in the PV-community. For the determination of contact recombination parameters, however, no standard approach exists.

In the analysis of PERC cells often the charge carrier recombination at the contacts and diffused layers is found to be a major power loss [8]. Integrating passivating contacts using poly-crystalline silicon on thin inter-facial oxides (POLO) is a promising approach to further reduce recombination losses and, therefore, increase the solar cell efficiency. Solar cells from market-typical p-type Si featuring POLO contacts have already achieved high efficiencies of 26.1% [9] on lab-scale interdigitated back contact (IBC) devices. The integration of POLO junctions into industrial cells faces the challenge of processing cell structures with good quality POLO junctions and their metallization with lean, industrial process flows to compete with the low-cost PERC process. In this work we calculate the efficiency gain to be expected from specific concepts featuring POLO junctions. This helps the industry to evaluate the economic feasibility of these concepts.

The calculation of power losses in PERC solar cells and the estimation of the efficiency benefits when integrating POLO junctions into industrial Si solar cells is the main goal of this work. To this end, we also study the determination of contact recombination parameters. This includes finding appropriate test samples, measurement techniques and evaluation procedures.

Chapter 1 and 2 introduce the theoretical background for this work. In **chapter 1** we introduce the PERC cell concept and its various sources of power losses. We further introduce the SEGA and the FELA along with the conductive boundary approach for solving the semiconductor equations. In addition, we also introduce the basic recombination mechanisms and the concept of charge carrier lifetimes to lay the foundation for lifetime and recombination measurements. In **chapter 2** we introduce the I-V, resistance, reflectance and lifetime measurement methods and the approaches for the extraction of simulation input parameters from these measurements.

In **chapter 3** we analyze the determination of contact recombination parameters. To this end, we first discuss the requirements for the sample structures and the limitations for measurements setups that can be used for the measurement of these samples. We then discuss known analytical approaches for the extraction of recombination parameters and compare the models to numerical device simulations. We also introduce a method solely based on device simulations for the analysis of contact recombination. In this context we also introduce a new model for the injection dependency of contact recombination.

In **chapter 4** we discuss the difference between the SEGA and the FELA, which are commonly used approaches for analyzing power losses in silicon solar cells. We further introduce a simulation tool (SEGA-GUI) created in the context of this work to automatically perform SEGA simulations. We then apply the measurement and evaluation techniques from chapter 2 and 3 to the complete characterization of a PERC batch with the required reference samples. In the context of this characterization we also discuss the uncertainties for the determination of input parameters and how these translate to the uncertainties in the simulation results.

In **chapter 5** we discuss optimization routes for PERC when using POLO junctions. We analyze ten cell concepts featuring POLO junctions along with a PERC and a TOPCon reference, which is a cell structure with n-type poly-Si and a boron emitter

[10]. To this end, we introduce optical and electrical simulation setups based on input parameters aimed at comparable results for all analyzed cell concepts. Finally, from the simulation results and the discussion of potential ways to process each structure, a roadmap for further cell development is developed.

1 Theory and fundamentals

In this chapter we describe the passivated emitter and rear cell (PERC) concept as the current state-of-the-art industrial silicon solar cell. We then explain the power loss mechanisms present in such cells as well as the free energy loss analysis (FELA) and the synergistic efficiency gain analysis (SEGA) as approaches for the analysis of these losses. Because both approaches are based on device simulations, we further describe the conductive boundary (CoBo) model for solving the semiconductor equations in a solar cell. This model is based on experimentally determined input parameters. The determination of most input parameters is explained in chapter 2 except for the charge carrier recombination at the contacts. The determination of contact recombination is discussed in chapter 3 and, therefore, we also introduce the fundamental recombination properties in the silicon bulk and at the surfaces and their parameterization.

1.1 Passivated emitter and rear cells

The PERC solar cell concept [11] is shown on the left side of Fig. 1.1. The cell is based on an acceptor-doped (p-type) crystalline Si absorber (light green). In most cases this absorber is a Czochralski-grown (Cz) mono-crystal doped with boron. The front side of the cell features a highly donator-doped (n-type, usually phosphorus) layer called emitter and shown in red. This diffusion can be varied laterally (selective emitter) to optimize the recombination and resistive properties underneath the contacts and in the remaining area separately. The emitter is covered with silicon nitride (SiN) for surface passivation (see section 1.2.1) shown in blue. The SiN is simultaneously used as an anti-reflection coating (ARC) to enhance the fraction of light that enters the device. The front contacts are realized by screen-printing local silver contacts in a conventional H-pattern (shown in dark gray). The rear side features a stack of aluminum oxide (Al_2O_3) and SiN for surface passivation. This stack is opened locally using a laser. These laser contact openings (LCO) allow the screen-printed aluminum (dark gray) to form local aluminum back surface field (Al-BSF) contacts, which are shown in dark green. The passivation at the rear side reduces the charge carrier recombination and allows for a better optical performance due to the enhanced reflectivity of the Al_2O_3/SiN stack in comparison with conventional Al-BSF cells.

The right side of Fig. 1.1 shows a PERC+ cell [12] that differs from a PERC cell by using rear metal fingers instead of full area metallization and an optional rear surface texture. This design has several advantages over the conventional PERC design [12]:

The aluminum paste consumption is drastically reduced, the formation of the Al-BSF is improved and light incident on the rear side can be utilized. The main focus of this work is the analysis and simulation of PERC+ solar cells and improvements thereof.

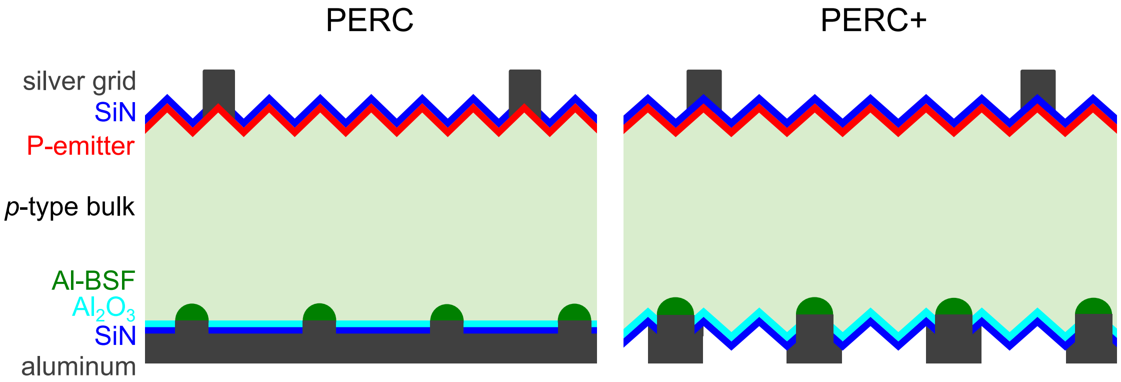

Figure 1.1: Schematic of a passivated emitter and rear cell (PERC) and a PERC+ cell with only partial rear-side metallization and rear texture. Both cell structures feature a front phosphorus doped emitter (red) with a SiN ARC and passivation (blue), a surface texture (not to scale) and silver contacts (gray). At the rear the screen-printed Al forms a local back surface field (green) while the remaining area is passivated with an Al_2O_3/SiN stack (teal and blue).

1.2 Loss analysis

A first estimate of losses can already be obtained by analyzing the I-V characteristics (see section 2.1 on page 16) of a solar cell. Here optical, recombination and transport losses are quantified by reductions in the short-circuit current J_{SC}, the open-circuit voltage V_{OC} and the fill factor FF, respectively. However, this approach does not allow for a quantitative comparison of different loss channels due to the different units of measure. In addition, a more detailed analysis of individual losses is crucial for the optimization process. Approaches that meet these requirements are often based on modeling the solar cells. Two examples are the free energy analysis (FELA) [1] and the synergistic efficiency gain analysis (SEGA) [2, 3]. Both yield results in the same unit of measure (power per area) for all loss channels. In this section we introduce sources of power losses, FELA and SEGA as well as the numerical modeling approaches used in this work. The difference between FELA and SEGA as loss and gain analyses, respectively is discussed in section 4.1.

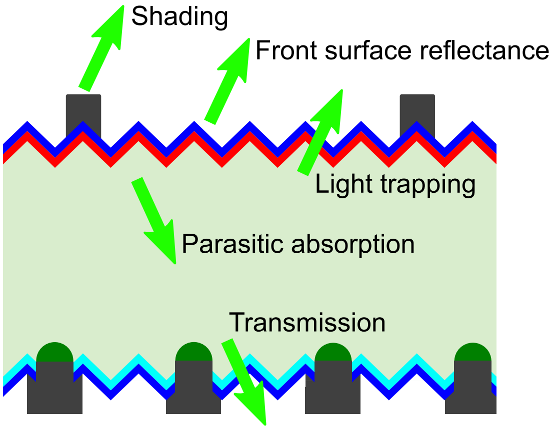

Figure 1.2: Schematic of a solar cell with non-intrinsic optical losses. The green arrows represent optical losses due to shading, an imperfect anti-reflection coating, parasitic absorption by free charge carriers, transmission through the cell and imperfect light trapping.

1.2.1 Power losses in solar cells

A solar cell converts a fraction of incident light into electrical energy. This fraction, the conversion efficiency η, is always limited by intrinsic losses such as thermalization of charge carriers to the band edges, optical losses due to non-absorbed photons and intrinsic recombination and transport losses. The maximum efficiency that can be achieved with a crystalline silicon solar cell is 29.56% [7] for a cell without doping and 98.1 μm thickness. In addition, a solar cell also always has non-intrinsic losses, which can, in principle, be avoided by optimized process characteristics. In this work we discuss characterization and simulation techniques with the goal to understand the origin of the dominant power losses in PERC solar cells. As we are interested in routes for further cell optimization, we focus on the non-intrinsic losses. These losses can be categorized into three different groups: optical, recombination and transport losses.

Optical losses

An ideal solar cell has a perfect ARC on the front side and a perfect mirror on the rear side. In addition, incident light is completely randomized to increase the path length. This ensures Lambertian light trapping, which is a widely accepted benchmark for the ideal optical performance [13].

An actual solar cell is, however, not perfect: Shading by metal contacts imposes losses on front and rear contacted (FRC) cells. This leads to the optical losses shown in Fig. 1.2. It should be noted that these losses differ for bare cells and cells integrated in a module. In this work we analyze bare cells for their losses, but this should be kept in mind when designing cells for module integration.

In FRC cells the metal on the front side leads to a shading of the absorber, which reduces the generated current. The relative current loss corresponds to the area fraction covered by metal. However, the shape of the finger can allow reflected photons to hit the cell surface and contribute to the generated current. Therefore, the optical width (or shading width) can be smaller than the geometrical finger width.

Another important loss is due to the reflectivity $\mathcal{R}$ at the front surface. The ARC on the front side is a dielectric layer with a suitable refractive index to reduce reflectivity. The reflectivity of a one layer ARC can only be fully reduced to zero for one wavelength λ as the optimal layer thickness for destructive interference is $\lambda/(4\nu)$ where ν is the refractive index of the ARC [14]. Most industrial solar cells feature a front surface texture with random pyramids. Due to the pyramids, most reflected photons hit the surface a second time thereby reducing $\mathcal{R}$ to $\mathcal{R}^2$. Further approaches to reduce reflectivity are a double- or multi-layer ARC [15] or adapted surface topologies such as black silicon [16] or macropores [17, 18].

Light that enters the solar cell through the front surface does not necessarily create an electron-hole pair. The photons can also be absorbed in surface layers or by free carriers in the device. This parasitic absorption cannot be utilized for generating electrical energy.

Photons with an energy close to the band gap energy have a long absorption length due to the low absorption probability. These photons have a chance to leave the cell through the rear side. These transmission losses can be avoided by increasing the reflectivity of the rear side either by a suitable dielectric layer stack or a mirror either external or directly applied to the dielectric stack.

The absorption probability for long-wavelength light can also be increased by suitable light trapping schemes. Lambertian light trapping, which serves as a benchmark in this work, assumes complete randomization when the light enters the cell. Any remaining fraction of specular light leads to optical losses, because the mean path of the light in the solar cell is typically shorter for specular light [13].

Recombination losses

The locations of non-intrinsic recombination are shown in Fig. 1.3. Recombination occurs at all surfaces and in the silicon bulk. Recombination at the surfaces can be reduced by a suitable coating, which is called passivation layer. An ideal passivation saturates the dangling bonds from the interrupted crystal lattice (chemical passivation) and contains fixed charges inducing an electric field, which reduces the minority carrier concentration at the surface (field effect passivation). At the metal contacts, however, the surface is not passivated leading to a large recombination current. In industrial solar cells the metallized area is, therefore, kept to a minimum. In addition, a highly doped area underneath the metal reduces the recombination as it reduces the minority carrier concentration. In chapter 5 we discuss the implementation of passivating contacts

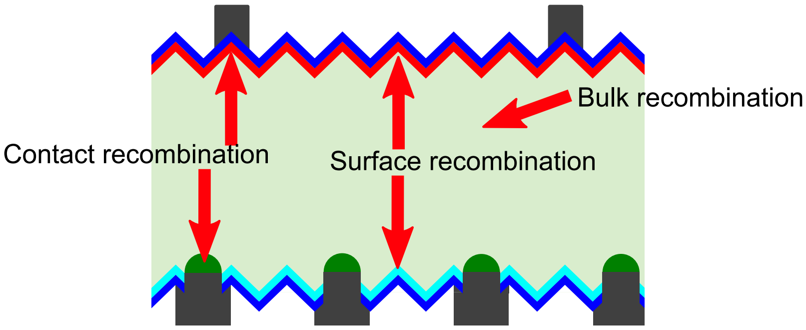

Figure 1.3: Schematic of a solar cell with non-intrinsic recombination losses. The red arrows represent recombination losses at the contacts, at the diffused and un-diffused surfaces and in the Si bulk.

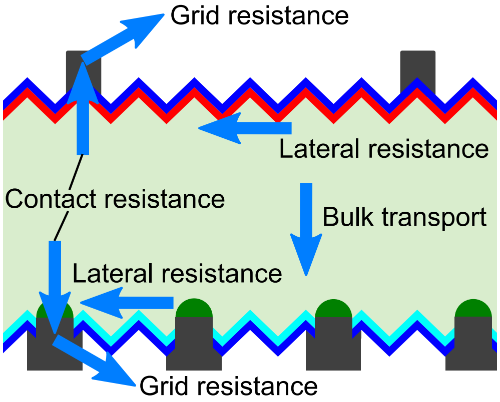

Figure 1.4: Schematic of a solar cell with non-intrinsic transport losses. The blue arrows represent transport losses due to the contact and metal grid resistances, the lateral resistance (sheet resistance) between the contacts and transport losses in the Si bulk.

(i.e. contacts, which simultaneously provide surface passivation underneath the metal) into industrial production lines to reduce recombination at metal contacts. To reduce recombination in the absorber, a better Si material with reduced impurities and defects can be used.

Transport losses

Electric currents flowing through a resistor lead to resistive heating. The power dissipated in the resistor is lost for delivering work in the circuit. Figure 1.4 shows the various resistances, which exist in a solar cell. The cell metallization, especially on the front side, features thin metal fingers leading to a resistive loss due to the metallization. In addition, the contact between metal and silicon inhibits a contact resistance. The metallization layout has to be optimized to balance the losses due to shading and recombination with those caused by the resistive losses at the contacts and in the metal grid. Furthermore, carrier transport in the silicon bulk also leads to power dissipation. Transport in the Si bulk can be divided into lateral and perpendicular transport. Both transport losses can be reduced by increasing the dopant concentration in the absorber. Furthermore, highly doped layers, for example the emitter diffusion, provide an increased lateral conductivity for one charger carrier type. In addition, the distances between the contacts (for lateral transport losses) and device thickness (for perpendicular transport losses) can be reduced. However, all approaches lead to a trade-off between recombination and optical losses and losses due to transport.

In the following sections we introduce approaches for analyzing all three groups of power losses in solar cells simultaneously.

1.2.2 Free energy loss analysis

The free energy loss analysis (FELA) [1] is a loss analysis for solar cells based on analyzing the free energy balance in a device. The photo-generation rate leads to a generation rate of free energy

$$\dot{F}_{\mathrm{G}} = q \int_{\mathrm{Vol.}} \Delta\phi(\vec{x}) g(\vec{x}), \tag{1.1}$$

where $\Delta\phi(\vec{x})$ is the local quasi Fermi level (QFL) splitting, $g(\vec{x})$ is the local generation rate at position $\vec{x}$ and q is the elementary charge.

This free energy can, however, not be completely extracted from the solar cell to deliver work to an external circuit. The diffusion-driven and/or field-driven transport leads to an increase of entropy and, hence, to a decrease of free energy. Recombination currents in a solar cell also lead to a reduction of free energy. We calculate the extracted power in terms of free energy rates as

$$P_{\mathrm{OUT}} = \dot{F}_{\mathrm{G}} - \dot{F}_{\mathrm{R}} - \dot{F}_{\mathrm{T}}. \tag{1.2}$$

Here $\dot{F}_{\mathrm{R}}$ is the rate of free energy lost by charge carrier recombination and $\dot{F}_{\mathrm{T}}$ is the rate of free energy lost by the transport of charge carriers through the solar cell. We calculate the free energy loss rates with the following equations:

$$\dot{F}_{\mathrm{R}} = q \int_{\mathrm{Vol.}} \Delta\phi(\vec{x}) r(\vec{x}), \tag{1.3}$$

$$\dot{F}_{\mathrm{T}} = \int_{\mathrm{Vol.}} \left(\frac{|j_e|^2}{\sigma_{\mathrm{n}}} + \frac{|j_h|^2}{\sigma_{\mathrm{p}}} \right), \tag{1.4}$$

with local recombination rate $r(\vec{x})$, local electron and hole currents j_e and j_h and electron and hole conductivities σ_{n} and σ_{p}, respectively. A detailed derivation of these equations

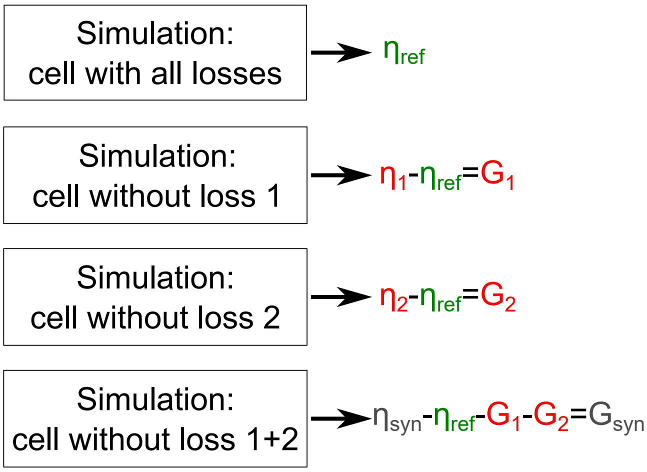

Figure 1.5: Schematic of the synergistic efficiency gain analysis. First the solar cell efficiency is simulated unchanged, which is referred to as η_{ref}. The gain corresponding to each loss channel is determined by an additional simulation in which the respective loss channel is switched off. The gain is the difference of the simulated efficiencies. Synergistic gains can be determined with the same approach by subtracting the reference efficiency and the individual gains from the simulated efficiency with multiple loss channels switched off.

can be found in Ref. 1. All quantities required for the calculation of free energy loss rates with equation 1.3 and 1.4 can be obtained by a single simulation of the solar cell at maximum power point. In Ref. 19 Greulich *et al.* extended the FELA to optical losses by calculating the additional free energy that could be created by un-absorbed photons. As these losses are wavelength dependent an additional integral over the wavelength λ is required

$$\dot{F}_{\text{O}} = q \int_{\text{Vol.}} \Delta\phi(\vec{x}) \int_{\lambda} g(\vec{x}, \lambda) X(\lambda), \tag{1.5}$$

where $X(\lambda)$ is the wavelength dependent loss mechanism, for example the front-side reflectivity (X=$\mathcal{R}$).

1.2.3 Synergistic efficiency gain analysis

The synergistic efficiency gain analysis (SEGA) [2, 3] is a gain analysis for solar cells based on simulations of the device with sequentially deactivated loss channels.

A schematic of the SEGA is shown in Fig. 1.5: First we simulate the solar cell as fabricated, which we will refer to as reference simulation. Next we switch off each loss channel individually and perform another device simulation to calculate the efficiency gain as the difference of the two simulated conversion efficiencies (switch-off minus reference). We do this for all individual loss channels in the solar cell. This means that we set the respective parameters such that recombination currents and resistances are zero and the optical performance is optimal as described in section 1.2.1. We then also switch off multiple loss channels simultaneously and calculate the synergistic gain as the efficiency that is gained in access of the sum of the individual gains. Thereby, the SEGA is able to break down the efficiency gap between the reference efficiency and the theoretical limit for this structure. It should be noted that this limit is not necessarily 29.56% as calculated in [7] because the cell thickness and doping may not have the required values.

1.2.4 Conductive boundary model

Both FELA and SEGA are based on modeling the solar cell. For cell modeling we apply the conductive boundary (CoBo) model [20], because it is based on easily accessible experimental input parameters and leads to low simulation times.

Electrical and chemical transport are described by the quasi Fermi level (QFL), one for the electrons and one for the holes. In addition, the Poisson equation for the electrostatic potential applies. This leaves us with three coupled differential equations, which have to be solved numerically using suitable boundary conditions

$$\nabla(\sigma_{\mathrm{n}}\nabla\phi_{\mathrm{n}}) = -q(g-r), \tag{1.6}$$

$$\nabla(\sigma_{\mathrm{p}}\nabla\phi_{\mathrm{p}}) = q(g-r) \tag{1.7}$$

and

$$\nabla(\epsilon_0\epsilon_r\nabla\phi_{\mathrm{el}}) = q(N_{\mathrm{D}}+p-N_{\mathrm{A}}-n), \tag{1.8}$$

where ϕ_{n} and ϕ_{p} are the QFLs for electrons and holes respectively, ϕ_{el} is the electrostatic potential and ϵ_0 and ϵ_r are the vacuum and material permittivity. N_{D} and N_{A} are the donator and acceptor concentration, respectively and n and p are the electron and hole density, respectively. The boundary conditions are defined by the surface recombination. Together with the detailed doping profiles, defect densities and a generation profile (see section 2.3 on page 19) the equations can be solved, for example by using software like COMSOL [21] or Sentaurus [22]. However, the input parameters for these simulations are often difficult to obtain and the simulations are time consuming due to the steep gradients of doping profiles near the surface. An alternative approach is the conductive boundary (CoBo) model [20] in which diffused layers are treated as conductive surfaces with no physical depth. These conductive boundaries are characterized by the recombination current density and a sheet resistance. The CoBo model, thus, has two advantages: The input parameters are relatively easy to obtain (see chapters 2 and 3) and the simulation time is drastically reduced because the steep gradients near the surface are avoided. In addition to the CoBo model, a second simplification holds in many cases: The Si bulk can be assumed to be quasi-neutral, i.e. there is not local net charge [23]. This assumptions holds in cases of small electric fields. However, in cases of large electric fields, as for example close to short-circuit conditions, this assumption breaks down. If quasi-neutrality applies, equation 1.8 can be neglected and only the two equations for the QFLs have to be solved. This further increases computational speed and numerical stability [23]. This concept is implemented in Quokka 2 [23], a freeware simulation tool, which we use throughout this work. The input parameters that we use for our PERC cells together with suitable methods for their determination are listed in Tab. 4.4 in chapter 4.

There are two special cases of simulations that are not possible in Quokka: As described above, the assumption of quasi-neutrality breaks down when the device is operated close to short-circuit conditions. Consequently, the short-circuit case can not be directly modeled in Quokka. The short-circuit current can, however, be determined by extrapolating the current from regions where the I-V characteristic is flat but quasi-neutrality still applies. This is possible when the cell is not limited by either a large series or a small shunt resistance. The second case is the modeling of (lifetime) samples, which have no emitter diffusion. The solver in Quokka requires contacts of both polarities to be defined. A good approximation can then be achieved, according to the Quokka manual [24], when defining the contact to cover only a few percent of the non-contacted side and, in addition, defining a high sheet resistance.

1.3 Recombination and charge carrier lifetime

Recombination effects reduce the average time between excitation and recombination of charge carriers, which is called effective lifetime τ_{eff}. We discuss the three fundamental recombination mechanisms. We further explain the parameterization of surface recombination and the relation between τ_{eff} and the individual recombination channels. We confine the scope of this section to the properties relevant for the further work. More elaborate information on carrier recombination and lifetime can be found, for example, in solar cell textbooks [14, 25].

1.3.1 Recombination mechanisms

Carrier recombination in semiconductors is caused by three mechanisms, namely radiative, Auger and Shockley-Read-Hall recombination. In the following we briefly explain the mechanisms and give parameterizations for the recombination rates used in this work.

The inverse process to the absorption of photons is radiative recombination. In this process an electron relaxes back to the valence band edge and emits a photon with an energy close to the band gap energy. The rate at which the recombination process occurs is proportional to the product of electron concentration n and hole concentration p. The recombination rate can be described by

$$r_{\text{rad}} = B_{\text{rad}}(np - {n_i}^2), \tag{1.9}$$

where n_i is the intrinsic carrier density and B_{rad} the proportionality factor for radiative recombination. In this work we use $B_{\text{rad}} = 4.82 \cdot 10^{-15}\ \text{cm}^3\text{s}^{-1}$ [26]. In indirect semiconductors like silicon, radiative recombination only plays a minor role due to the low probability of this process as it requires the involvement of a phonon.

The second intrinsic recombination is the Auger recombination. This process involves three particles, either two electrons and one hole or one electron and two holes. In this process one excited charge carrier relaxes back to the band edge by transferring energy to another excited carrier in the same band. That charge carrier then also quickly relaxes back to the band edges by transferring energy to the crystal lattice in form of thermal energy. The product of densities of the involved charge carriers is proportional to the probability of the respective process. The recombination rate of an Auger process can be described as the sum of the two processes:

$$r_{\text{Auger}} = C_{\text{n}} n^2 p + C_{\text{p}} n p^2, \tag{1.10}$$

with proportionality factors C_{n} and C_{p}. In reality however, the description of Auger recombination is more complex, because Coulomb enhancement of the recombination rate has to be considered, which depends on the dopant concentration and the injection level. Therefore, we employ the parameterization by Richter *et al.* [27] for modeling the intrinsic lifetime in this work, which is implemented in Quokka.

Shockley-Read-Hall (SRH) recombination describes recombination via trap states within the band gap. The SRH-recombination rate depends on the energy level of the trap-state. However, in most cases the injection dependent lifetime can be accurately modeled using a mid-gap SRH-defect. Therefore, we use a simplified model of the general SRH-expression in this work [28]

$$r_{\text{SRH}} = \frac{np - {n_i}^2}{(n + n_i)\tau_{\text{p0}} + (p + n_i)\tau_{\text{n0}}}, \tag{1.11}$$

with hole and electron lifetime parameters τ_{p0} and τ_{n0}, respectively.

1.3.2 Surface recombination

In addition to recombination in the silicon bulk, recombination also occurs at the surfaces. The surface recombination current J_{rec} is commonly described by either a saturation current density J_0 or a surface recombination velocity S:

$$J_{\text{rec}} = J_0 \left(\frac{np}{{n_i}^2} - 1 \right), \tag{1.12}$$

$$J_{\text{rec}} = S q \Delta n, \tag{1.13}$$

Parameter	**Value**
N_{dop}	$10^{16}\,\mathrm{cm}^{-3}$
W	0.02 cm
J_0	$6\ \mathrm{fA/cm}^2$
τ_{n0}	$3\times10^{-4}\,\mathrm{s}$
τ_{p0}	$3\times10^{-3}\,\mathrm{s}$

Table 1.1: Parameters for lifetime example in Fig. 1.6

where Δn is the excess carrier concentration. For surface recombination Δn is taken at the edge of the neutral Si bulk region. When Δn is much smaller than N_{dop} (low level injection) both models yield equal results with

$$S = J_0 \frac{N_{\mathrm{dop}}}{q{n_i}^2}, \tag{1.14}$$

where N_{dop} is the dopant density in the bulk. If the assumption of low level injection is not valid both descriptions show different dependencies on Δn. For the J_0-description J_{rec} is proportional to Δn^2 at high injection and for the S-description it is proportional to Δn.

This raises the question which model describes the physical recombination mechanism best. This question has been discussed by McIntosh *et al.* in Ref. 29. He found that the best model depends on the surface dopant density and the surface charge. When modeling PERC cells with the CoBo model we need to describe the recombination at four different surfaces: the surfaces dielectrically passivated by an Al_2O_3/SiN stack, the emitter passivated with SiN and the metallized electron and hole contacts. The J_0-description was originally used to describe recombination in a passivated emitter and, therefore, we employ the J_0-description for emitter surfaces. McIntosh *et al.* found that the J_0-description is also best suited to describe the recombination at the Al_2O_3/SiN stack over all relevant injection densities. Consequently, we use the J_0-description for the non-contacted surfaces, because it reproduces the injection dependency of J_{rec} best. Furthermore, J_0-values can be stated independent of the doping concentration and injection level and can be determined with the Kane-Swanson method (see section 2.4.4 on page 26) without knowledge of the precise bulk lifetime. The correct description of injection dependent contact recombination is more complicated and discussed in section 3.3.2 on page 45.

1.3.3 Charge carrier lifetime

For each recombination process with a recombination rate r there is an associated lifetime, which is defined as

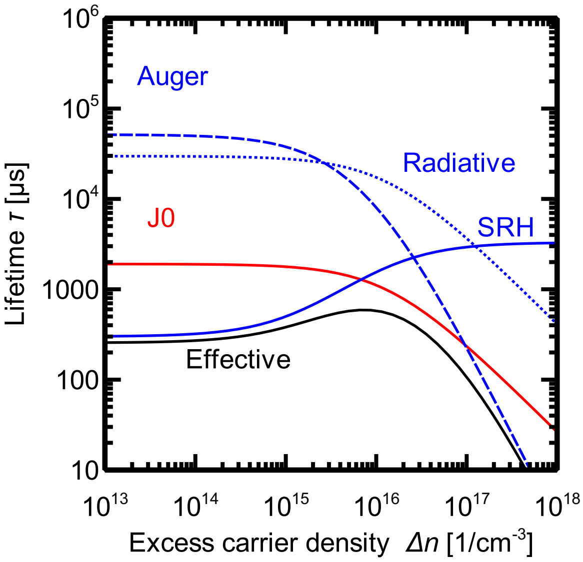

Figure 1.6: Individual lifetimes due to different recombination mechanisms and the resulting effective lifetime in an example device.

$$\tau = \frac{\Delta n}{r}. \tag{1.15}$$

It should be noted that surface recombination is a local process. Consequently, the impact on τ_{eff} depends on the transport of charge carriers to the surface. In general, this effect is considered using device simulations. when assuming that the recombination is not transport limited the respective lifetime is [30]

$$\tau_{\text{surface}} = \frac{qW{n_i}^2}{2J_0(N_{\text{dop}} + \Delta n)}. \tag{1.16}$$

The individual lifetimes for each process can be used to calculate the effective lifetime of the device

$$\frac{1}{\tau_{\text{eff}}} = \frac{1}{\tau_{\text{rad}}} + \frac{1}{\tau_{\text{Auger}}} + \frac{1}{\tau_{\text{SRH}}} + \frac{1}{\tau_{\text{surface}}}. \tag{1.17}$$

Figure 1.6 shows the injection dependent individual lifetimes as well as the resulting effective lifetime for an example device for which the parameters are shown in Tab. 1.1. The differences in the injection dependency of the individual lifetimes will later be used to separate the individual effects in a measurement of the effective lifetime (section 2.4).

2 Measurement methods

Modeling solar cells requires a number of experimental input parameters, as shown in the previous chapter. In this chapter we introduce the measurement techniques and methods used in this work for the determination of input parameters. The analysis of recombination under local metal contacts is discussed in chapter 3. Furthermore, the simulations of solar cells are often compared to measured I-V characteristics to evaluate the quality of the simulation. Therefore, we also briefly introduce I-V measurements and a few aspects that have to be kept in mind when using I-V measurements to verify simulation results.

2.1 Current-voltage characteristic

In an I-V measurement a solar cell is operated at different set voltages and the output current is measured (or vice versa). The cells maximum efficiency η under standard testing conditions (STC) according to the IEEE 60904-3 standard (illumination with AM1.5g spectrum, $100\ \mathrm{mW/cm^2}$ irradiation intensity and at 25°C) is the most important figure on which all solar cells are rated [14, 25]. In addition, the open-circuit voltage V_{OC}, the short-circuit current density J_{SC} and the fill factor FF provide valuable information on cell performance and limitation. Furthermore, and most important for this work, the I-V curve can be used to evaluate the quality of simulation results. Possible deviations in J_{SC}, V_{OC} and FF can help identifying the origin of the deviation.

In this work we use a LOANA cell tester [31] to measure the I-V curve. The cell is illuminated with a Xenon flash approximately reproducing the AM1.5g spectrum for the measurement of J_{SC}. During the measurement of the I-V characteristic the cell is illuminated with an LED array where the intensity is adjusted to reproduce the measured J_{SC}, thereby yielding approximately the same operating conditions as under AM1.5g illumination. The cell is contacted with a four-point probe setup using contacting probes in a configuration that neglects the busbar resistance as discussed in [32]. In the context of this work, it follows that the busbar resistance is not part of the bare cell analysis but should be considered for module integration.

2.2 Transfer length method

The transfer length method (TLM) [33, 34] determines the contact and sheet resistances of metal contacts on diffused semiconductors. It is based on four-point probe resistance

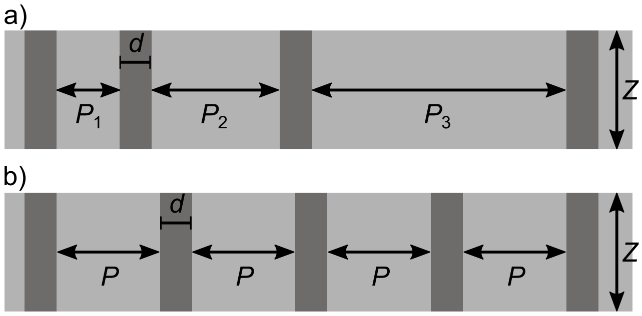

Figure 2.1: a) Conventional TLM sample with contacts of width d in different distances $P_1 - P_3$ to each other on a stripe with width Z. b) TLM sample as cut from a solar cell: All contacts are in the same distance P. The different measuring distances required for TLM are realized by measuring between different pairs of contacts.

measurements between pairs of contacts in different distances from each other. The contact and sheet resistance can be determined from the measured linear dependency between resistance and distance. In the following we briefly introduce TLM theory and discuss some special cases used in this work. For the measurements in this work we use the TLM-SCAN setup by pv-tools [35].

The resistance between two contacts on a thin diffused layer spaced by the distance P amounts to [34]

$$R = 2R_c + R_{\text{sheet}} \frac{P}{Z}, \tag{2.1}$$

where R_c is the contact resistance and R_{sheet} is the sheet resistance of the thin diffused layer underneath the contacts. Z is the width of the sample stripe. Thin in this context means that the diffused layer is much thinner than the contact width d. Measuring the resistance between the different contacts in Fig. 2.1 a) yields the resistance for different contact spacings. Using a linear regression both R_c and R_{sheet} can be determined from equation 2.1. For the determination of the specific contact resistivity ρ_{c} from R_c, current crowding, i.e. locally increased current densities, has to be considered by numerically solving [34, 36, 37]

$$R_c = \frac{\rho_{\text{c}}}{Z L_{\text{T}}} \coth\left(\frac{d}{L_{\text{T}}}\right), \tag{2.2}$$

with the transfer length

$$L_{\text{T}} = \sqrt{\frac{\rho_{\text{c}}}{R_{\text{sheet}}}}. \tag{2.3}$$

For the characterization of contact resistances on solar cells it is convenient to cut TLM samples directly from the solar cell rather than fabricating additional test structures. In

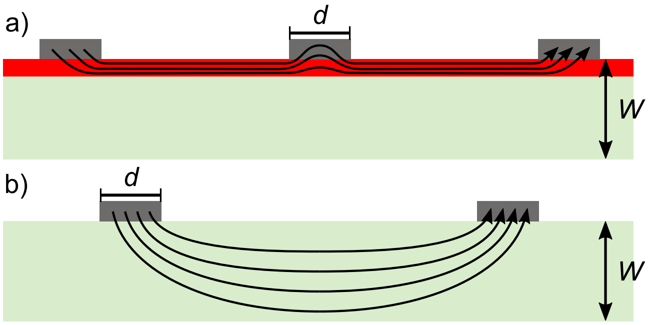

Figure 2.2: Cross sections of TLM samples: a) cross section of a TLM sample for contacts on an emitter diffusion with intermediate contacts and b) cross section of a TLM sample for contacts to the Si base. The arrows represent the current flow in the respective sample.

this case the different contact spacings are realized by measuring between different pairs of contacts, as shown in Fig. 2.1 b). However, this means that there are intermediate contacts between the two measuring points. These intermediate contacts reduce the resistance because part of the current flows through the metal as shown in Fig. 2.2 a). This effect can be accounted for by assigning an effective width to the contacted area, which is smaller than the width of the contact [38]

$$d_{\text{eff}} = 2L_{\text{T}} \tanh \frac{d}{2L_{\text{T}}}. \tag{2.4}$$

Classic TLM theory only applies to metal contacts on structures where the conductive layer thickness is small compared to the contact width. If the current spreading in the base, which is shown in Fig. 2.2 b), is neglected when analyzing contacts to the base, the contact resistivity is overestimated [39]. However, TLM can also be applied to contacts to the base using the empirical analytical model presented by Eidelloth and Brendel in Ref. 39. For this model a geometry factor is derived from the two limiting cases of very small sample thickness and very low contact resistivity:

$$G = 1 + \sqrt{(G_{\text{1D-TLM}} - 1)^2 + (G_{\text{CM}} - 1)^2}, \tag{2.5}$$

with

$$\begin{aligned}
&G_{\text{1D-TLM}} = \sqrt{\gamma}\coth(\sqrt{\gamma}),\\
&\gamma = \frac{d^2\rho_\text{b}}{\rho_\text{c}W},\\
&G_\text{CM} = 1 + \gamma + \gamma\frac{\delta}{\pi}\left(\ln 4 - \ln\left(e^{\frac{\pi}{\delta}} - 1\right)\right),\\
&\text{and}\\
&\delta = \frac{W}{d},
\end{aligned}$$

where ρ_b is the resistivity of the Si bulk. The contact resistivity is then determined from

$$G = \frac{b}{m}\frac{\rho_\text{b}d}{2\rho_\text{c}W}, \tag{2.6}$$

where m and b are the slope and intercept of the linear fit to the measured data, respectively. A detailed derivation and analysis of equations (2.5) and (2.6) can be found in Ref. 39.

2.3 Optical properties

Modeling solar cells requires a quantification of the optical generation of electron-hole pairs in the device, as described in section 1.2.4. This generation cannot be measured directly. Although different approaches for determining the optical generation exist, we employ two methods in this work: An analytical model, which is fitted to a measured reflectance spectrum and optical modeling based on ray-tracing. It should be noted that we confine the optical analysis to one-dimensional (average) generation profiles. This is sufficient in most cases, because usually lateral optical variations are small and diffusion lengths are large.

2.3.1 Analytical reflectance fit

The analytical model for optical generation used in this work is designed for analytically calculating the generation profile from a measured reflectance spectrum and was introduced in Ref. 3. While the concept of this model is straight-forward the resulting equations are tedious so we will explain the model using Fig. 2.3 but refrain from showing the final equations. A detailed derivation including the final equations can be found in Ref. 3.

The concept of this model is shown in Fig. 2.3. Specular (black, index s) and diffusive light (red, index d) are treated in separate channels. Furthermore, the intensities are separated into top (index t) and bottom (index b) as well as traveling upwards (index

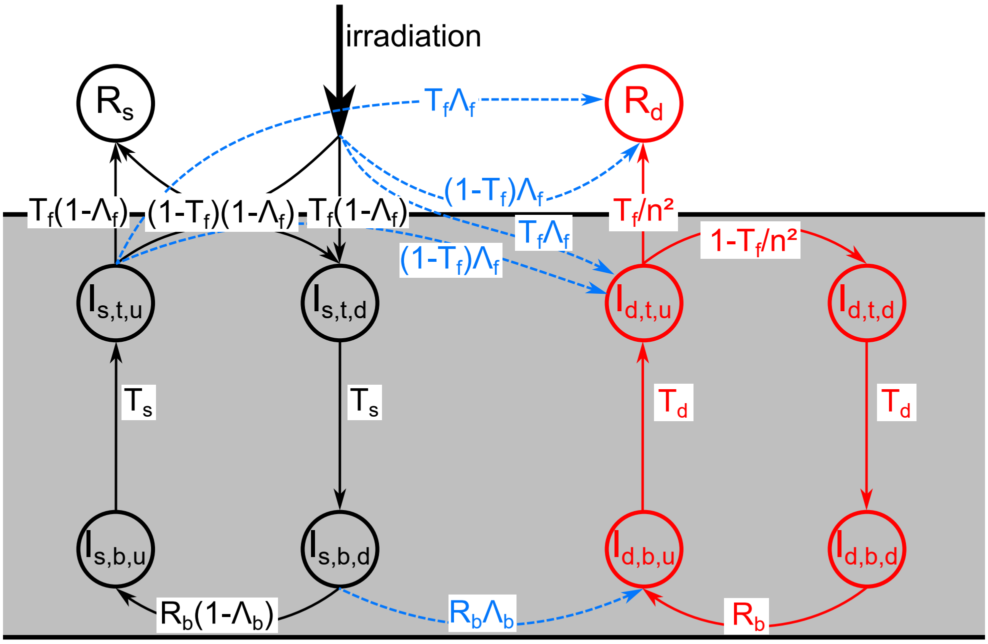

Figure 2.3: Schematic for the analytical optical model developed in Ref. 3. The ten circles represent the light intensity contributions analyzed in this model. The terms at the connection lines between the circles give the fraction of light that is transferred to the respective intensity. The black and red lines and circles represent specular and diffusive light, respectively. The blue dashed lines show the transition from the specular into the diffusive channel. Figure adapted from Ref. 3.

u) or downwards (index d). The terms for the transition from one intensity contribution to another are shown in Fig. 2.3. Transmission as well as reflection at both front- and rear-side leads to a partial randomization of light due to rough surfaces. The fraction of light that is randomized with each interaction (ie. enters the diffusive channel, blue dashed lines) is described by a Lambertian factor for each side (Λ_f and Λ_b in Fig. 2.3). Furthermore, the reflection probability of photons at the front and rear surface is described by $\mathcal{R}_\mathrm{f} = 1 - T_\mathrm{f}$ and $\mathcal{R}_\mathrm{b}$, respectively. Collecting all intensities and transmissions along the lines in Fig. 2.3 results in ten coupled linear equations for the eight intensities in the wafer as well as the specular and diffusive reflectance, each represented by a circle in Fig. 2.3. These equations can be solved to describe the measured reflectance, which is the sum of diffusive and specular reflectance, using Λ_f, Λ_b, $\mathcal{R}_\mathrm{f}$ and $\mathcal{R}_\mathrm{b}$ as well as the refractive index of silicon and the absorption coefficients for specular and diffusive light. The latter quantities are known from the literature. The other four quantities can be determined by fitting the model to a measured reflectance spectrum. For short wavelengths ($\lambda < 900$ nm) the measured reflectance is equal to $\mathcal{R}_\mathrm{f}$, because light entering the cell is quickly absorbed. For long wavelengths $\mathcal{R}_\mathrm{f}$ is extrapolated with a second-order polynomial fitted to the reflectance between 800 and 900 nm. The three remaining parameters can then be fitted to the measured reflectance using this model. However, both Λ_f and Λ_b have a very similar effect on the calculated reflectance. Therefore, it increases the numerical stability if one of the Lambertian factors is set to a fixed value. For textured samples we use $\Lambda_\mathrm{f} = 0.335$, which agrees well with the average path length enhancement by a pyramid texture.

The determined values for Λ_f, Λ_b, $\mathcal{R}_\mathrm{f}$ and $\mathcal{R}_\mathrm{b}$ can then be used for calculating the generation profile. The generation in an ideal solar cell can be calculated when assuming $\Lambda_\mathrm{f} = 1$, $\mathcal{R}_\mathrm{f} = 0$ and $\mathcal{R}_\mathrm{b} = 1$. Note that in this case Λ_b is irrelevant as all light directly enters the diffusive channel when entering the cell. It should be noted that this model also includes the effect of free carrier absorption (FCA) as described in Ref. 3. However, other forms of parasitic absorption, as for example in poly-Si layers, are not included in this model.

2.3.2 Ray tracing

The analytical model described above is well suited to analyze PERC cells and similar samples. However, the model does not include all optical aspects, which plays an important role for the analysis of poly-Si cell concepts in chapter 5. For this work the most important shortcomings are parasitic absorption other than FCA and lateral variations of optical properties. For these cases we use a ray-tracing approach for the determination of the generation profile. In this work we employ the program SUNRAYS [40] for the ray-tracing simulations. By simulating the involved unit cells and then area-averaging the results we gain the final generation profile.

Ray tracing determines the generation profile by simulating a large number of photons and tracing their path through the solar cell. It requires the knowledge of the geometrical properties (layer thickness etc.) and of the (complex) refractive index of all materials present in the solar cell. These refractive indices are determined once and do not need to be measured on each individual cell. Like the analytical model, ray-tracing is based on probabilities. Each photon is traced through the simulated structure and at every interface or pass through a layer the photon is either reflected, transmitted or absorbed based on the probability for the respective process. By simulating a large number of photons, the absorption distribution yields the generation profile.

2.4 Recombination properties

In this section we describe the determination of bulk and surface recombination properties. We first introduce the charge carrier lifetime measurement techniques used in this work, namely (quasi-)steady-state photoconductance ((Q)SSPC), photoconductance-calibrated photoluminescence imaging (PC-PLI) and infrared lifetime mapping (ILM). We then briefly introduce how to separate bulk and surface recombination from the measurement of the effective charge carrier lifetime τ_{eff}.

2.4.1 (Quasi-)steady-state photoconductance (Q)SSPC

(Q)SSPC [41] is a widely used technique in the PV-community as it allows for quick and precise determination of effective lifetimes in non-metallized samples. For the (Q)SSPC method a sample is illuminated with steady- or quasi-steady-state illumination and the conductivity of the wafer is determined by inductive coupling of the sample to a coil. The conductivity of a Si wafer is much lower than the conductivity of a metal layer or metal contact-pattern. Therefore, only non-metallized samples can be analyzed with (Q)SSPC. Quasi-steady-state means that the illumination intensity changes on a timescale much larger than the carrier lifetime. Which light source is used depends on the measurement setup, but does not affect the measurement theory. The quasi-steady-state illumination has the advantage that a wide range of injection densities can be analyzed on short timescales without significant sample heating. In this work we use a Sinton WCT-120 lifetime tester [42] as QSSPC setup for measuring lifetime samples and a SSPC setup for the calibration of photoluminescence images (see section 2.4.2).

A detailed derivation and description of the QSSPC measurement theory can be found in Ref. 41. By exploiting the balance of generation and recombination in a device under steady-state conditions and the knowledge of electron and hole mobilities μ_n and μ_p in silicon the effective lifetime can be expressed as [41]

$$\tau_{\mathrm{eff}} = \frac{\sigma_{\mathrm{L}}}{J_{\mathrm{Gen}}(\mu_n + \mu_p)}, \tag{2.7}$$

where σ_{L} is the measured conductivity increase due to illumination and J_{Gen} is the generated photo-current. Consequently, the determination of the effective lifetime only requires the knowledge of J_{Gen}, which can be determined via a reference cell and/or ray-tracing. In the WCT-120 lifetime tester and the SSPC setup in the PC-PLI system a reference cell is integrated and differences of J_{Gen} of the reference cell and the sample are considered using a suitable optical factor, which can be determined via ray-tracing or test measurements with solar cells.

2.4.2 Photoconductance-calibrated photoluminescence imaging

Photoluminescence imaging (PLI) is a widely used technique for analyzing Si lifetime samples and solar cells. PLI allows for a spatially resolved lifetime image by detecting the luminescence emission of a sample using a camera, in this work a Si- charge-coupled-device (CCD) camera. Since PLI raw images only yield the amount of detected luminescence, a calibration is required. The most practical and accurate approach is to use a SSPC setup within the PLI system to determine the lifetime under equal measurement conditions. This photoconductance-calibrated (PC-)PLI is described in Ref. 43. PC-PLI can only be used if part of the sample is not metallized to use the SSPC

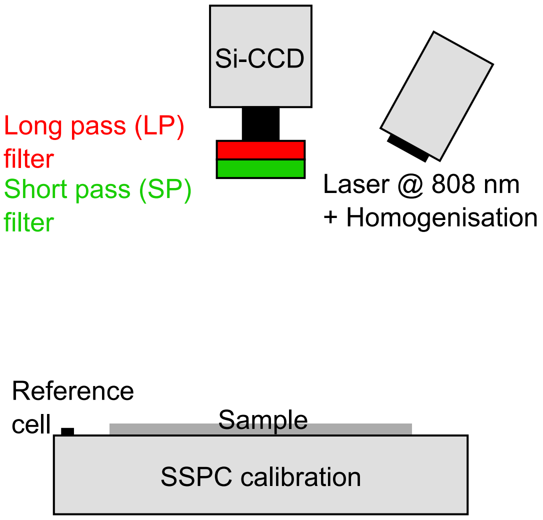

Figure 2.4: PC-PLI measurement setup used in this work. The sample is placed on a SSPC stage. The illumination is realized by a laser with a wavelength of 808 nm with suitable homogenisation. The luminescence emission is recorded with a Si-CCD camera. The reflected light as well as the luminescence emission reflected at the rear side of the sample are effectively blocked using a long and a short pass filter, respectively.

method in that area or if a non-metallized sample with an identical optical behavior is available. We analyze the application of PC-PLI and ILM (section 2.4.3) to partially metallized samples in chapter 3. Therefore, we briefly review the theory of PC-PLI. A more detailed description and derivation can be found in Ref. 43.

The luminescence emission of a lifetime sample or solar cell is proportional to the radiative recombination

$$I_{\mathrm{PL}} \propto r_{\mathrm{rad}} = B_{\mathrm{rad}} np \approx B_{\mathrm{rad}} \Delta n (\Delta n + N_{\mathrm{dop}}), \tag{2.8}$$

which leaves the determination of the proportionality factor as the only step for the determination of the effective lifetime with equation (1.15). For each illumination intensity we determine Δn using the integrated SSPC setup. We then area-average the PL intensity over the coil area and determine the coefficients a and b for the quadratic relation between the PL intensity and Δn

$$I_{\mathrm{PL}} = a\Delta n^2 + b\Delta n. \tag{2.9}$$

This calibration is valid for all samples or sample areas with the same optical behavior. If the optical generation is known, a lifetime image can be deduced from the Δn map

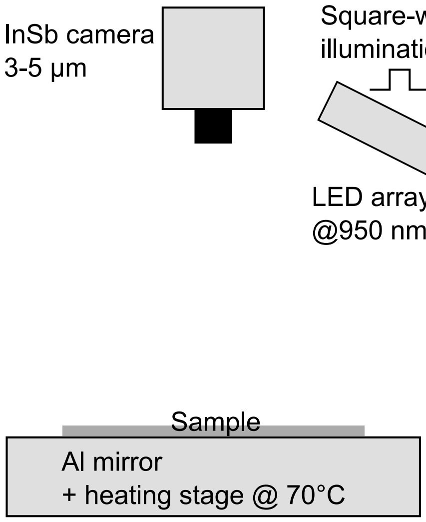

Figure 2.5: Measurement setup for ILM. The sample is placed on an Al mirror, which also heats the sample to 70 °C. It is illuminated with square-wave illumination at wavelength 950 nm using a LED array. The IR emission is recorded with an InSb camera sensitive at 3-5 μm wavelength.

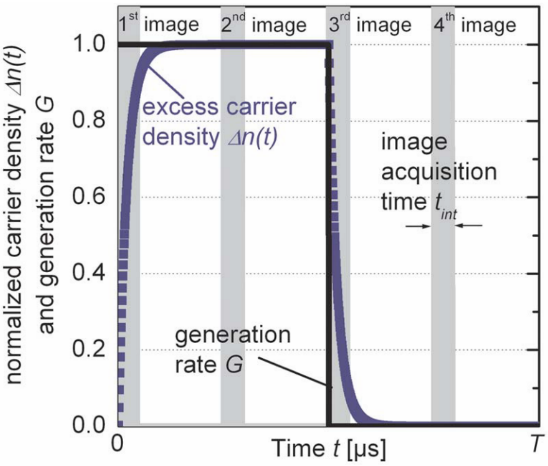

Figure 2.6: Normalized, time dependent generation rate and excess carrier density and image acquisition times for ILM measurements. Image reprinted from Ref. 47.

using equation 1.15 and the equality of carrier generation and recombination under steady-state conditions.

In chapter 3 we use PC-PLI to analyze partially metallized samples. In Ref. 44 Müller *et al.* showed that the metal on the rear affects the optical behavior of the sample and, therefore, makes the calibration in metallized areas invalid. However, this technique can still be applied by integrating an additional short-pass filter in the measurement setup to avoid light reflected at the rear-side metallization to enter the camera as shown in Ref. 44. The setup used in this work is described in Ref. 43 and Ref. 44 and shown in Fig. 2.4.

2.4.3 Infrared lifetime mapping

Infrared lifetime mapping (ILM) [45] utilizes the proportionality between infrared light (IR) emission and free charge carriers in a sample. We use the setup described in Ref. 46, which is shown in Fig. 2.5.

The sample is placed on an aluminum mirror, which also heats the sample to 70 °C.

The sample is illuminated with monochromatic square-wave illumination of wavelength 950 nm. The IR emission is recorded by an Indium-Antimonid (InSb) camera, which is sensitive in a wavelength range of 3-5 μm, using lock-in technique. The IR emission can be converted to lifetime mappings with two different approaches: static and dynamic ILM

Static ILM

For static ILM two images are recorded: the first after steady-state conditions are reached under illumination and the second after steady-state conditions are reached after switching off the illumination (image 2 and 4 in Fig. 2.6). The difference between both images already yields a relative lifetime map. To obtain absolute values the image has to be calibrated either by a QSSPC measurement or by the dynamic ILM approach presented below.

Dynamic ILM

For dynamic ILM [47] four images are recorded as shown in Fig. 2.6: The first directly after the illumination is switched on, the second after steady-state conditions are reached, the third after the illumination is switched off and the fourth after steady-state conditions are reached in the dark. It should be noted that the second and fourth image are those needed for static ILM so static ILM comes with no additional measurement effort.

The four images are multiplied with sine and cosine coefficients, which are in phase with the excitation. The summation of these images yields a sine and a cosine correlated image, which are the differences between image 2 and 4 and 1 and 3, respectively

$$S_{\sin} = S_2 - S_4, \tag{2.10}$$

$$S_{\cos} = S_1 - S_3. \tag{2.11}$$

The quotient of these two images yields a phase and, with the knowledge of the camera integration time, the lifetime can be determined from this phase via

$$\Phi = \arctan\left(\frac{S_{\sin}}{S_{\cos}}\right) = \arctan\left\{\frac{t_{\text{int}} - 2\tau_{\text{eff}}\left[\exp\left(-\frac{T}{4\tau_{\text{eff}}}\right) - \exp\left(-\frac{T+4t_{\text{int}}}{4\tau_{\text{eff}}}\right)\right]}{t_{\text{int}} - 2\tau_{\text{eff}}\left[1 - \exp\left(-\frac{t_{\text{int}}}{\tau_{\text{eff}}}\right)\right]}\right\}, \tag{2.12}$$

where T is the length of one lock-in period and t_{int} is the camera integration time. A detailed derivation of equation 2.12 can be found in Ref. 47. Except for τ_{eff}, equation 2.12 contains only the known parameters t_{int} and T and the measured phase Φ. Consequently, τ_{eff} can be determined without any calibration.

Although the calibration-free method has its advantages, the emitted infrared light travels large lateral distances up to about 50 times the wafer thickness leading to a strong blurring effect. This effect is especially critical for the dynamic evaluation approach as the time signal from high lifetime regions dominates over the signal from adjacent low lifetime regions as shown in Ref. 46. In addition, the analysis of lifetimes below 50 μs yields large uncertainties due to multiple effects in the setup (for a detailed discussion and analysis see Ref. 46). It is, therefore, recommended to use the dynamic ILM approach to calibrate the static ILM image in high lifetime regions. The application of the ILM approach to partially metallized samples is discussed in section 3.2.

2.4.4 Bulk and surface recombination

The measurement setups introduced in the previous section yield the injection-dependent effective lifetime of a sample. For solar cell modeling a more detailed breakdown of this lifetime into all recombination channels is desirable. In section 1.3 we introduced the recombination channels relevant for solar cells and their respective injection-dependent lifetimes, which are shown in Fig. 1.6. The intrinsic lifetime can be accurately modeled using the dopant density. This leaves the separation of the SRH and surface recombination as the only remaining step for accurate modeling. In this section we show how to separate bulk and surface recombination and introduce the samples needed for a complete characterization.

Kane-Swanson method

In this work we use the method introduced by Kane and Swanson [30] for the separation of bulk and surface recombination. The "Kane-Swanson" method and improvements thereof are a widely used approach in the PV community and, for example, readily implemented in the WCT-120 Sinton lifetime tester used in this work. We briefly review the concept to understand the implications for the necessary lifetime samples.

For the separation of SRH and surface recombination we first correct the measured τ_{eff} for intrinsic recombination according to equation 1.17

$$\frac{1}{\tau_{\text{corr}}} = \frac{1}{\tau_{\text{eff}}} - \frac{1}{\tau_{\text{rad}}} - \frac{1}{\tau_{\text{Auger}}}. \tag{2.13}$$

Following from equations 1.17 and 1.16 the derivative with respect to Δn of the inverse corrected lifetime reads

$$\frac{d}{d(\Delta n)}\left(\frac{{n_i}^2}{\tau_{\text{corr}}}\right) = \frac{J_0}{qW} + \frac{d}{d(\Delta n)}\left(\frac{{n_i}^2}{\tau_{\text{SRH}}}\right). \tag{2.14}$$

The intrinsic carrier concentration is injection dependent if band gap narrowing is considered. In high injection the dependence of τ_{SRH} on Δn can be neglected and J_0 of the equal surfaces can be determined from the slope of $1/\tau_{\text{corr}}$. However, this approach employs assumptions and models, which limit the accuracy of the approach. It was shown in Ref. 48 that the accuracy of the J_0 determination depends on the injection level at which the measurement is evaluated. Kane and Swanson already proposed that

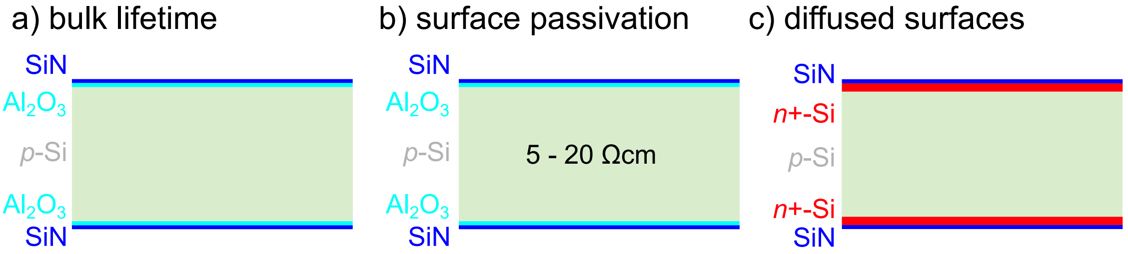

Figure 2.7: Test structures for the determination of a) the bulk lifetime, which has to be processed as closely to the cell process as possible and on the same wafer material, b) the recombination at the passivated surfaces processed on high resistivity Si to ensure a higher accuracy of the J_0 determination and c) the diffused surfaces featuring a symmetric emitter diffusion.

the assumption of a uniform carrier density breaks down for high injections densities. However, injection densities larger than the dopant concentration are required for the separation of SRH and surface contributions. Consequently, a sample with low dopant density yields a higher accuracy for the determination of J_0.

Samples for the determination of charge carrier lifetimes

The recombination properties except for the contacts can be determined when using a test structure, which undergoes the entire cell process except the metallization. However, the highest accuracy is achieved when using separate, symmetric reference samples for the bulk lifetime, the passivated and the diffused surfaces as shown in Fig. 2.7. In addition, the samples for the characterization of surface recombination should be processed on high resistivity (5-20 Ωcm) material to increase the accuracy of the separation of bulk and surface recombination. The accuracy is increased because high injection conditions, where the surface is dominating, are reached at lower Δn.

Especially boron-doped Si, which is the basis for most industrial solar cells, contains recombination active boron-oxygen defects [49]. The recombination activity of these defects strongly depends on the temperature budget, hydrogen introduction and other process characteristics. In addition to boron-oxygen defects, other impurities contained in the silicon can contribute to the charge-carrier recombination. Recombination defects in silicon are still vividly discussed in solar cell research and not all defects in a solar cell are identified. For measuring bulk recombination precisely it is important to fabricate the test structure as similar to the solar cell as possible. This includes the temperature budget during e.g. the diffusion and layer deposition steps.

3 Recombination at metallized surfaces

The quantification of contact recombination is essential for device modeling of solar cells as shown in chapter 4. In this work a contact is defined as the interface between metal and silicon along with the highly diffused layers underneath. This has the advantage that the resulting contact properties can be directly used in Quokka. The determination of recombination properties of the contacted areas in a solar cell must consider the multi-dimensional current flow. Deriving $J_{0,\mathrm{cont}}$ from lifetime measurements, which measure an effective charge carrier lifetime τ_{eff}, can be achieved using analytical or numerical approaches as discussed in section 3.3. The challenge is to correctly account for the recombination currents in the non-contacted parts of the sample and to account for the internal resistances. Although different models for the determination of these parameters exist, their accuracy and the applicability of underlying assumptions has not been tested for analyzing contact recombination. In addition, all models are restricted to specific metallization layouts (periodic point or full line contacts) and measurement conditions (low injection). Furthermore, the applicability of different measurement approaches to partially metallized samples, which are required for the analysis of contact recombination, has not been tested so far. Therefore, we compare different sample structures, measurement techniques and evaluation methods for determining the contact recombination in this chapter.

3.1 Sample structures

In this section we discuss the requirements for the sample structures. The analysis of contact recombination is based on comparing charge carrier lifetimes measured on samples with different metallization fractions and/or no metallization (a detailed discussion follows in section 3.3). The different metallization fractions can be either realized on one or multiple samples. A general requirement for these samples is that the recombination in the remaining parts of the sample should be reduced as far as possible, to ensure a high sensitivity. In this work, we analyze the local Al-BSF and Ag on P-diffusion contacts present in PERC cells. For the Al-BSF contacts the sample features equal Al_2O_3/SiN passivation layers on both sides and local Al-BSF contacts on the rear as shown in Fig. 3.1 (a). For the Ag contacts the sample, shown in Fig. 3.1 (b), features an equal P-diffusion on both sides and can be either based on *n*- or *p*-type Si, as discussed in section 3.1.2. The contacts are applied to the rear side with selective doping underneath if it is also used for the cells. In both cases the contact geometry is that used in the cell except for the finger pitch that may be varied. In addition, in case of boron-doped silicon the boron-oxygen defects should be deactivated by illuminating the sample at elevated temperatures after processing [50]. This minimizes the impact of the bulk recombination.

For the analysis of charge carrier lifetime variations due to different metallization fractions on one wafer, the lateral inhomogeneity of the lifetime over the wafer area and the interaction of charge carriers between regions of different lifetimes must be considered. Therefore, we discuss implications rising from an inhomogeneous lifetime and coupling between different regions for partially metallized samples before we discuss the metallization patterns that can be employed for the $J_{0,\mathrm{cont}}$-analysis.

3.1.1 Inhomogeneities

A homogeneous bulk lifetime and passivation quality over the analyzed area of the sample is essential to the determination of $J_{0,\mathrm{cont}}$ values. Any inhomogeneity contributes to the uncertainty of the analysis. If the lifetime deviation due to the inhomogeneity of the bulk lifetime or the passivation quality is of the same order of magnitude as the changes due to the metallization or even larger, the determination of meaningful $J_{0,\mathrm{cont}}$-values is not possible. As an example, Fig. 3.2 shows a PL image of a sample with local Al-BSF contacts with 16 differently metallized areas. The contact opening width is 64 μm for the entire wafer and the metallization fraction is varied using different contact pitches, which are shown in the image. For this sample it is obvious that areas with identical metallization (eg. fields 9 and 11) yield very different lifetimes. Because changes of the lifetime are dominated by the inhomogeneity rather than the different metallization

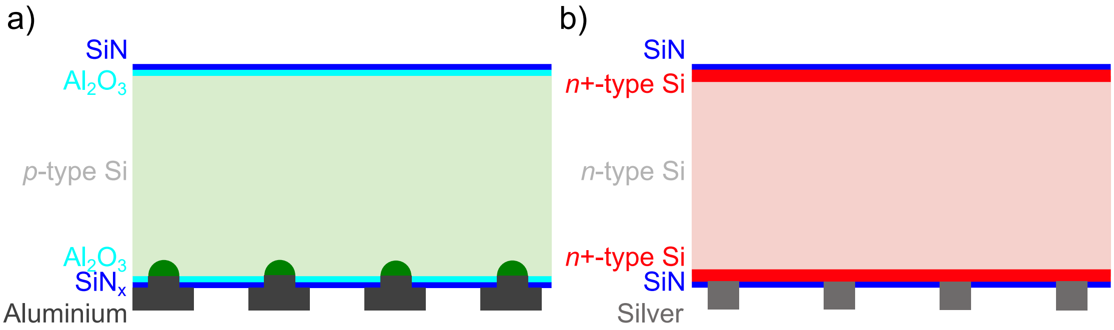

Figure 3.1: Schematics for the test structures for contact recombination. a) Sample with Al_2O_3/SiN passivation on both sides of the p-type wafer and Al-BSF contacts on the rear. b) Sample with $n+$ diffusion on both sides of the n-type wafer and Ag contacts on the rear.

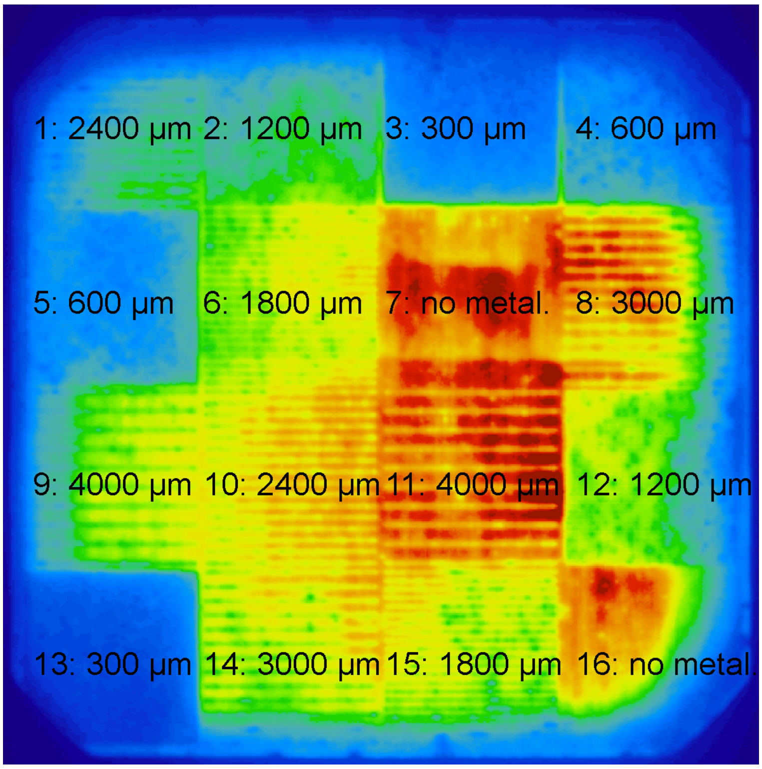

Figure 3.2: PL image (not calibrated) of an inhomogeneous lifetime sample. The different areas are metallized with Al with contact lines of 64 μm width. The pitch is given in the image for each field. Here areas with equal metallization yield very different lifetimes (compare e.g. field 9 and 11).

fractions, the determination of $J_{0,\mathrm{cont}}$ values is not possible with this sample.

Reduction of inhomogeneities in the bulk lifetime and the surface passivation must, thus, be a primary concern when designing $J_{0,\mathrm{Ag}}$-samples. However, inhomogeneity can not be completely avoided. In many cases the inhomogeneity shows systematic and statistic features. Examples for systematic inhomogeneity are low lifetimes at the wafer edges, rings of different lifetime due to varying defect concentrations in the bulk (Cz-rings) and side-to-side or mid-to-edge lifetime gradients due to varying passivation quality. As these effects can hardly be avoided completely, the metallization pattern (see section 3.1.3) should be designed to reduce the systematic effect. For example, the effect of mid-to-edge gradients and/or defect rings in the bulk can be reduced by applying a central symmetric metallization pattern. The effect of low lifetime wafer edges can be reduced by designing the metallization pattern such that the edges are not relevant for the $J_{0,\mathrm{cont}}$ analysis. Statistic variations of the lifetime should be of much shorter length scales than the areas of the metallization pattern and evenly distributed over the wafer to ensure that these deviations are averaged out in the analysis.

3.1.2 Coupling between regions of different lifetime

Different metallization fractions on one wafer lead to regions of different lifetime, which are not fully independent from one another. However, the analysis of these samples (see section 3.3) is based on the assumption that these regions can be treated as independent. In this section we analyze the coupling between regions of different lifetime in order to estimate the length-scale on which the QFLs and Δn are affected, in the following called coupling length x_c.

We fabricate samples for which a cross section is shown in Fig. 3.3. The sample features a 1.5 Ωcm, 160 μm thick p-type Si wafer with an n-type diffusion on both sides with a sheet resistance R_sheet of 140 $\Omega/\square$ passivated with SiN. The left side of the cross section is not contacted whereas the right side features 40 μm-wide Ag line contacts with 0.45 mm pitch. Consequently, the left side features a higher effective lifetime and will in the following be referred to with index *hl* (high lifetime) whereas the right side will be referred to with index *ll* (low lifetime). We measure the QFL splitting, also called internal voltage V, of the sample using PC-PLI. A line scan of this measurement at two illumination intensities is shown in the bottom part of Fig. 3.3 as green and red circles for strong and weak illumination, respectively. The photo-generation currents are $J_\mathrm{g,strong} = 25\,\mathrm{mA/cm^2}$ and $J_\mathrm{g,weak} = 1.8\,\mathrm{mA/cm^2}$ as determined by the Quokka fit introduced below. It is centered around the interface between both regions and extending 10 mm into each region. We see that the voltage shows a continuous decrease from the high to the low lifetime region. Furthermore, we see that x_c depends on the illumination density.

We also simulate this sample using Quokka. We describe all recombination channels in each region with a lumped $J_\mathrm{0,eff}$ to simplify the analysis. We determine the respective $J_\mathrm{0,eff}$-values to $J_\mathrm{0,hl} = 25\,\mathrm{fA/cm^2}$ and $J_\mathrm{0,ll} = 90\,\mathrm{fA/cm^2}$ by fitting the simulated lifetime to the measurement in both regions. It should be noted that it is not possible to define emitters at both surfaces within Quokka. To obtain the same lateral conductivity provided by the two 140 $\Omega/\square$ emitters we use one 70 $\Omega/\square$ emitter in Quokka. The simulation results for strong and weak illumination are shown in the bottom part of Fig. 3.3 as green and red line, respectively. We see that the simulation using the lumped J_0 and R_sheet values describes the experiment well using the stated parameters. When planning sample structures for $J_\mathrm{0,cont}$ determination we could, in principle, simulate the device using this approach to estimate x_c. However, this approach requires a good knowledge of the sample before it is fabricated. In addition, the physical background behind the coupling and the impact of sample properties on x_c remain unclear in this simulation based approach. Therefore, we analyze the coupling analytically using a linear approximation for the voltage.

Here we analyze the coupling in the high lifetime region (between $-x_\mathrm{c}$ and 0). However, the effect is symmetric around the interface between both regions and the same arguments and equations apply for the low lifetime region. For the analysis of the coupling length we are interested in the distance from the interface at which the QFLs are

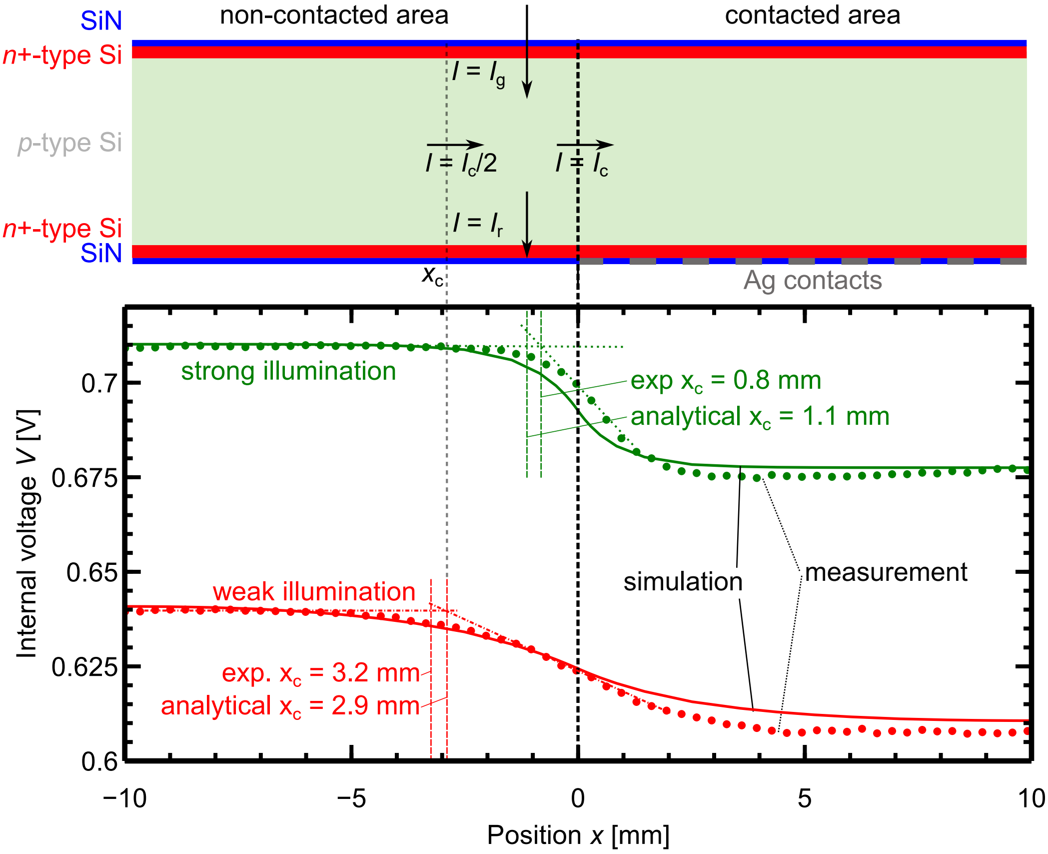

Figure 3.3: Top: sample cross section with symmetric $n+$ diffusions on a p-type wafer for the analysis of coupling between regions of different lifetime. The left side is not contacted and, therefore, has a higher lifetime, whereas the right side features 40 μm-wide Ag line contacts with 450 μm pitch and has a lower lifetime. Bottom: Measured (dotted line) and simulated (solid line) internal voltage for strong (green) and weak (red) illumination with the respective calculated and graphically determined coupling lengths x_c.

approximately equal to their values far away from the interface. For the definition of the linear voltage approximation we use two boundary conditions: The voltage at x_c from the interface equals the voltage far away from the interface (V_hl) and the voltage reduction at the interface equals half the total voltage difference (ΔV) between both regions

$$\begin{aligned} V(-x_{\mathrm{c}}) &= V_{\mathrm{hl}} \\ V(0) &= V_{\mathrm{hl}} - \frac{\Delta V}{2} \\ \Rightarrow V(x) &= -\frac{\Delta V}{2x_{\mathrm{c}}}(x + x_{\mathrm{c}}) + V_{\mathrm{hl}} \end{aligned} \tag{3.1}$$

To calculate x_{c} we employ the current balance in the region between the interface and $-x_{\mathrm{c}}$. At $-x_{\mathrm{c}}$ the derivatives of the QFLs are discontinuous. Therefore, we take the average of the derivatives left and right of $-x_{\mathrm{c}}$ for the calculation of the current through the interface, which yields half the current through the interface at $x = 0$. The minority and majority current through the interface at $x = 0$ are equal because there is no external electric field and no charge accumulation and hence no net current. Consequently, the coupling current density (line current density in units of A/m) through the interface between both regions can be calculated using the gradient of either QFL and the corresponding conductivity:

$$J_c = -\sigma_{\mathrm{n}} \frac{d}{dx}\phi_{\mathrm{n}} = \sigma_{\mathrm{p}} \frac{d}{dx}\phi_{\mathrm{p}} \tag{3.2}$$

As we analyze the coupling using an approximation for the voltage we require an expression of the current through the interface in terms of the voltage. Here we employ the equality of majority and minority current and the fact that the voltage gradient can be calculated as the difference of the QFL gradients:

$$\begin{aligned} \sigma_{\mathrm{n}} \frac{d}{dx}\phi_{\mathrm{n}} &= -\sigma_{\mathrm{p}} \frac{d}{dx}\phi_{\mathrm{p}} \\ \Rightarrow \frac{d}{dx}\phi_{\mathrm{n}} - \frac{d}{dx}\phi_{\mathrm{p}} &= \frac{\sigma_{\mathrm{n}} + \sigma_{\mathrm{p}}}{\sigma_{\mathrm{p}}} \frac{d}{dx}\phi_{\mathrm{n}} \\ \frac{d}{dx}\phi_{\mathrm{n}} - \frac{d}{dx}\phi_{\mathrm{p}} &= \frac{d}{dx}V = -\frac{\Delta V}{2x_{\mathrm{c}}} \\ \Rightarrow J_c &= \frac{\Delta V \sigma_{\mathrm{n}} \sigma_{\mathrm{p}}}{2x_{\mathrm{c}}(\sigma_{\mathrm{n}} + \sigma_{\mathrm{p}})} \end{aligned} \tag{3.3}$$

During a measurement we also have generation and recombination currents in the sample. In the regions far away from the interface these currents are equal because we do not extract charge carriers from the device. In the region between x_{c} and the interface the generation current is balanced by recombination and the coupling current (see Fig. 3.3 top):

$$\begin{aligned} I_g &= I_r + I_c - \frac{I_c}{2} \\ \Rightarrow J_{\mathrm{Gen}} x_{\mathrm{c}} &= \int_{-x_{\mathrm{c}}}^{0} J_{\mathrm{rec}} \mathrm{d}x + \frac{J_c W}{2} \end{aligned} \tag{3.4}$$

The integral over the recombination current is necessary because the recombination current depends on the voltage, which is decreasing towards the interface. Using the description with J_0 values we can solve the integral:

$$\begin{aligned}\int_{-x_c}^{0} J_{\mathrm{rec}}\mathrm{d}x &= \int_{-x_c}^{0} J_{0,\mathrm{hl}} e^{\frac{V(x)}{V_\mathrm{T}}}\mathrm{d}x \\ &= J_{0,\mathrm{hl}} e^{\frac{V_\mathrm{hl}}{V_\mathrm{T}}} \int_{-x_c}^{0} e^{\frac{-\Delta V}{2x_\mathrm{c}V_\mathrm{T}}(x+x_c)}\mathrm{d}x \\ &= J_{\mathrm{Gen}} \frac{2x_\mathrm{c}V_\mathrm{T}(1-e^{\frac{-\Delta V}{2V_\mathrm{T}}})}{\Delta V} \end{aligned} \tag{3.5}$$

where we used the equilibrium relation $J_\mathrm{rec} = J_{0,\mathrm{hl}}e^{V_\mathrm{hl}/V_\mathrm{T}} = J_\mathrm{Gen}$ far away from the interface. From this equilibrium condition for both regions we further derive an expression for ΔV:

$$\begin{aligned} J_{0,\mathrm{hl}} e^{\frac{V_\mathrm{hl}}{V_\mathrm{T}}} &= J_{0,\mathrm{ll}} e^{\frac{V_\mathrm{ll}}{V_\mathrm{T}}} \\ \Rightarrow \Delta V = V_\mathrm{hl} - V_\mathrm{ll} &= V_\mathrm{T} \ln\left(\frac{J_{0,\mathrm{ll}}}{J_{0,\mathrm{hl}}}\right) \end{aligned} \tag{3.6}$$

Using equations (3.3) to (3.6) we can now calculate the coupling length:

$$\rightarrow x_\mathrm{c} = \sqrt{\frac{V_\mathrm{T}\sigma_\mathrm{n}\sigma_\mathrm{p}W\ln\left(\frac{J_{0,\mathrm{ll}}}{J_{0,\mathrm{hl}}}\right)}{4J_\mathrm{Gen}(\sigma_\mathrm{n}+\sigma_\mathrm{p})\left(1-2\frac{\left(1-\sqrt{\frac{J_{0,\mathrm{hl}}}{J_{0,\mathrm{ll}}}}\right)}{\ln\left(\frac{J_{0,\mathrm{ll}}}{J_{0,\mathrm{hl}}}\right)}\right)}} \tag{3.7}$$

We see that the coupling length increases with decreasing illumination intensity. In case of low level injection, where the coupling length is largest, the conductivity of the majority carriers dominates and we have:

$$\sigma_\mathrm{p} = \frac{1}{\rho_\mathrm{b}} \tag{3.8}$$

$$\sigma_\mathrm{n} = \frac{1}{R_\mathrm{sheet}W} \tag{3.9}$$

The coupling is limited by the smaller lateral conductivity for either holes or electrons. Therefore, a sample with either only hole or only electron conducting wafer and layers shows very small coupling lengths. In case of our example we calculate x_c to 1.1 mm and 3.2 mm for strong and weak illumination, respectively. These values agree well with the values graphically determined from the measurements of 0.8 mm and 2.9 mm, respectively as shown in Fig. 3.3. Hence, any metallization pattern for this sample must allow a lifetime evaluation at least 3.2 mm away from every interface between

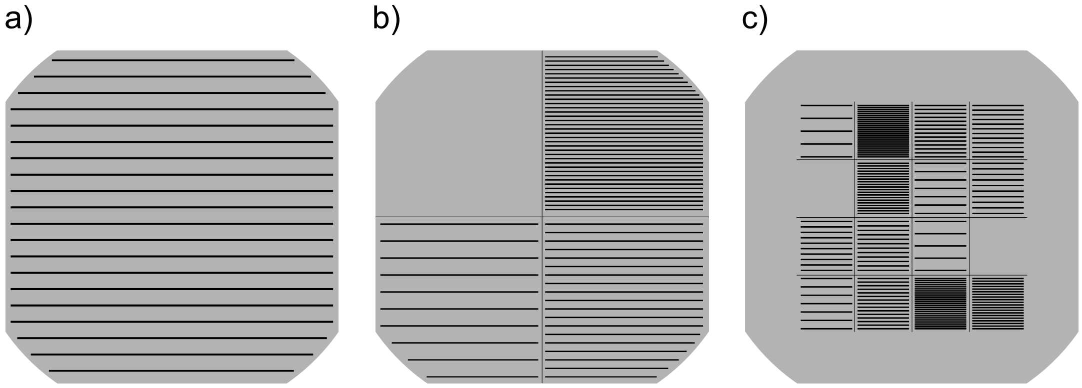

Figure 3.4: Schematics for different metallization patterns for the test structures for analyzing contact recombination. The black lines represent silver or aluminum contacts shown in Fig. 3.1. a) Full area cell metallization, b) Four areas with different metallization fractions (one without metallization) and c) 16 areas with different metallization fractions (two of each, two without metallization) and non-metallized edges.

metallization patterns. If the evaluation is performed at lower generation currents than $J_{\mathrm{Gen}} = 1.8\,\mathrm{mA/cm^2}$ the distance to the interfaces must be increased accordingly.

To avoid coupling and the resulting implications for the samples we recommend using n-type diffusions in n-type wafers or p-type diffusions in p-type wafers. This approach is used for the characterization in this work. However, often one type of material leads to a much higher lifetime or reduced inhomogeneities on the sample. In this case it is often beneficial to use the higher lifetime material and avoid the coupling by designing a metallization pattern that allows an evaluation further away from the interface than x_{c}.

3.1.3 Metallization patterns

There are three possibilities for the comparison of differently metallized samples: i) we can use samples with full area metallization patterns and compare multiple samples with different metallization fractions, ii) we can print areas with different metallization fractions on one wafer or iii) we can use the cell contacting geometry on one wafer and etch back the metallization after the measurement and then re-passivate the wafer. However, for the latter method we cannot ensure that the etch-back and re-passivation steps do not change recombination properties other than at the contacts. Therefore, we focus our analysis on the first two options.

There is no general answer to what the best metallization pattern is. The best choice depends on the lifetime of the sample and the corresponding inhomogeneities. Figure

3.4 shows three metallization patterns for determining the contact recombination. Using full area metallization as in Fig. 3.4 a) is preferable when lateral inhomogeneities of the effective lifetime are larger than the deviations between different samples, because we can then average over the entire wafer area. While this reduces the impact of lateral inhomogeneities it increases the uncertainty by using different samples on which the average lifetimes vary due to slightly different process characteristics. In addition, we have to process multiple samples. This argument gains a large impact when a screening of different printing properties (pastes, screens, firing temperature etc) is performed, because then a large number of samples has to be processed.

The pattern in Fig. 3.4 b) has four different areas each covering one quadrant of the wafer. This ensures that rotationally symmetric inhomogeneities (eg. Cz-rings) are averaged out in the analysis. Furthermore, evenly distributed, small scale inhomogeneities are also averaged out by the large areas of this pattern. For other systematic and symmetric inhomogeneities the pattern should be adapted such that the inhomogeneity is canceled out by averaging over the individual areas.

The pattern in Fig. 3.4 c) features 16 small fields with 7 different contact pitches and two non-metallized fields and non-metallized edges, which is similar to the pattern used in Fig. 3.2. This pattern allows for obtaining many data points to analyze the contact recombination and the corresponding uncertainty. The wafer edges are excluded from this pattern as the wafer edge often yields a low lifetime due to edge recombination or insufficient passivation quality. This pattern can only be used if the inhomogeneity of the sample is small. Also it does not allow for the correction of any symmetric inhomogeneities.

In this work we exclusively use the metallization pattern b) with four areas each covering one quadrant of the sample. We have found this pattern to suit our lifetime samples best, as our main concern are systematic rotational symmetric deviations due to Cz-rings and mid-to-edge passivation gradients. In addition, the large areas of the pattern have the benefit that most statistical inhomogeneities average out in the analysis.

3.2 Measurement techniques

For the analysis of recombination currents we have to measure the injection-dependent effective lifetime of partially, fully or non-metallized samples. The metallization prevents us from using QSSPC measurement for the entire analysis (see section 2.4.1 on page 22 for details). In addition, measurement systems with a spatial resolution are preferred, because areas with different metallization fractions on one wafer can be analyzed with a single measurement. Two camera-based approaches are PC-PLI (section 2.4.2 on page 22) and ILM (section 2.4.3 on page 24). It should be noted that the PC-PLI setup requires a short pass filter when measuring metallized samples (see section 2.4.2). In the following we compare PC-PLI, static ILM and dynamic ILM measurements for their applicability to partially metallized samples.

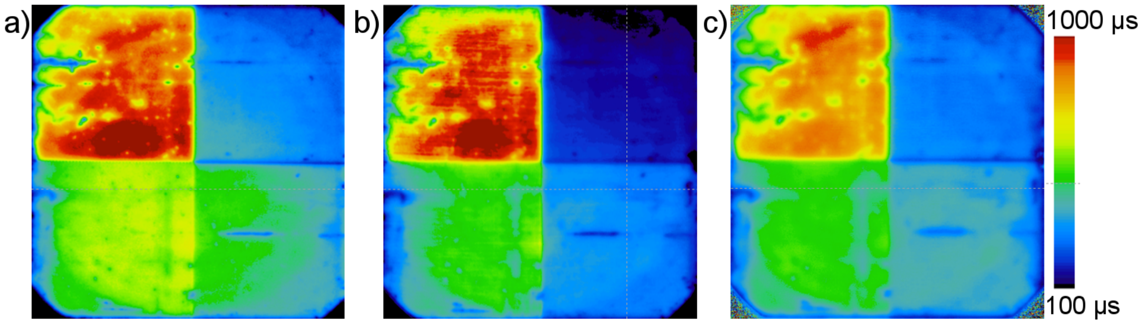

Figure 3.5: a) PC-PLI image, b) dynamically calibrated, static ILM image and c) dynamic ILM image of a partially metallized reference sample (metallization pattern Fig. 3.4 b)) for Al-BSF contacts (cross section Fig. 3.1 a)).

As an example for the comparison of measurement systems, we use a symmetric sample with Al_2O_3/SiN passivation on both sides. After opening contact lines with a width of $d = 64\,\mu$m, we print Al contacts in a metallization pattern shown in Fig. 3.4 b) with 4 areas, one non-metallized and the other three featuring contact pitches of 810 μm, 450 μm and 300 μm. Figure 3.5 shows the lifetime images of the sample measured with a) PC-PLI, b) dynamically calibrated, static ILM and c) dynamic ILM. The lifetime images show systematic differences, which we discuss in the following sections to identify the most suitable measurement system for the analysis of partially metallized samples.

3.2.1 PC-PLI measurement

The PC-PLI technique yields lifetime images, which are calibrated using SSPC measurements. The SSPC calibration in the PC-PLI setup used in this work is frequently cross-checked with a WCT-120 lifetime tester and, therefore, assumed to be correct in the non-metallized area. For the measurement of metallized samples a short-pass filter has to be employed (see section 2.4.2 on page 22). Consequently, the excess charge carriers near the front surface of the samples contribute stronger to the measured signal than those at the rear. In the non-metallized areas the filter has no effect on the measured lifetime, because the SSPC calibration Δn is uniformly distributed over the sample depth. The impact of the filter in the metallized areas has to be analyzed. To this end, we compare the excess carrier density at the front of the sample (measured by PC-PLI) to that averaged over the entire depth of the sample (measured by SSPC). For this comparison we employ a Monte-Carlo simulation with input parameters randomly chosen with uniform distribution from the respective range given in Tab. 3.1. We run 1000 simulations of the excess carrier density and compare the value of Δn directly at the front of the sample to that averaged over the depth of the sample. The excess carrier concentration at the front deviates by up to 8% from the concentration averaged over the depth of the sample. For metallization fractions smaller than 50% the maximum

Table 3.1: Input parameters for the Monte-Carlo simulation to evaluate the applicability of PC-PLI measurement to partially metallized samples.

Parameter	Value
W	150 to 250 μm
f_{met}	0 to 1
d	5 to 100 μm
ρ_{b}	1 to 20 Ωcm
τ_{bulk}	50 to 500 μs
$J_{0,\mathrm{pas}}$	0 to 100 fA/cm^2
$J_{0,\mathrm{cont}}$	$J_{0,\mathrm{pas}}$ to 1500 fA/cm^2
J_{Gen}	1 to 41 mA/cm^2

deviation is below 5%. In the PC-PLI measurement also light from deeper regions than directly at the surface contributes to the measured signal. Consequently, the Δn measured with PC-PLI lies between the value directly at the front, which we used in the simulation, and Δn averaged over the depth of the sample. Therefore, 5% deviation is a worst-case estimate for the uncertainty of the PC-PLI calibration in metallized areas for metallization fractions smaller than 50%.

3.2.2 Difference of dynamic and static measurement

Both static measurements shown in Fig. 3.5 a) and b) show a very similar distribution of τ_{eff} in the passivated area in the top left corner, whereas the dynamic lifetime image shows a deviating lifetime distribution. As discussed in Ref. 46, the dynamic approach raises certain deviations to static measurements:

1. The heat signal (i.e. the emission due to the temperature of the sample) varies due to the time dependent generation. This effect can be corrected by measuring the heat signal separately. This effect has a significant impact on the measurement for lifetimes below 50 μs.

2. Injection dependent lifetimes affect the time dependence of the Δn. This effect leads to an overestimation of τ_{eff} by the dynamic measurement up to 30% for $\tau_{\mathrm{n0}}/\tau_{\mathrm{p0}} \leqq 22$ with a maximum at $\tau_{\mathrm{n0}}/\tau_{\mathrm{p0}} = 15$.

3. Blurring has a large impact on dynamic measurements since the signal amplitude and hence the time dependence of high lifetime areas dominates over the small lifetime areas. In an example in Ref. 46, two adjacent areas of the same size one with $\tau_{\mathrm{eff}} = 10\,\mu$s and one with $\tau_{\mathrm{eff}} = 1000\,\mu$s yield a dynamic average lifetime of 685 μs while static approaches yield 505 μs.

The combination of these effects allows the consistent explanation of the slightly different lifetime distribution in the dynamic measurement in Fig. 3.5 c) as compared to the static measurements in a) and b). The different lifetime distribution together with the limitations for small lifetimes, the blurred signal and the deviation for injection dependent lifetimes limits the use of dynamic ILM measurements for the analysis. Therefore, we recommend using a steady-state measurement approach.

3.2.3 Difference of static ILM and PC-PLI

The comparison of the static approaches PC-PLI and static ILM in Fig. 3.5 a) and b) shows that the measured lifetime decreases stronger with the metallization fraction in the static ILM measurement. Figure 3.6 shows the normalized ratio (black crosses) between the lifetimes determined by PC-PLI and static ILM for the measurement shown in Fig. 3.5. For the highest metallization fraction of 21.3% the lifetime determined by static ILM is about 50% lower than the lifetime determined by PC-PLI. In section 3.2.1 we showed that the calibration of PLI images is correct within an uncertainty of 5%. This fails to explain the 50% difference between PC-PLI and static ILM and, therefore, we analyze the applicability of the static ILM approach to partially metallized samples in this section.

The static ILM approach relies on the calibration of the image to obtain lifetime values. For this calibration to work, the emission probability for the IR light created within the sample has to be the same for all sections of the sample. In the following we discuss how the metal contacts affect the emission probability for IR from the sample.

The free carriers in the sample created by the 950 nm illumination emit IR light in random directions. For our analysis we assume that half of the light power flux is traveling upwards (index u) and the other half traveling downwards (index d):

$$I_\mathrm{u} = I_\mathrm{d} = 0.5 I_0 \tag{3.10}$$

To estimate the change of emitted IR by the metallization we estimate the emission probability of an IR photon using Fig. 3.7.

At every interaction with a surface the photon is either reflected or transmitted based on the probability for the respective process. At the front side this probability is described by the internal reflectance $\mathcal{R}_\mathrm{f}$. At the rear side, which is contacted, the reflection probability differs for the metallized and the non-metallized area. In the non-metallized area we assume perfect reflectivity due to the external Al mirror. In the metallized area two effects reduce the reflectivity: 1) free carrier absorption in the highly doped region underneath the contacts (in this case the BSF) and 2) a reduced reflectivity at the Si metal interface. Both effects yield an effective reflectivity $\mathcal{R}_\mathrm{m,eff}$ of the metal contact. The reflectivity of the entire rear side $\mathcal{R}_\mathrm{b}$ can thus be composed of two area-averaged contributions

$$\mathcal{R}_\mathrm{b} = f_\mathrm{met} \mathcal{R}_\mathrm{m,eff} + 1 - f_\mathrm{met}, \tag{3.11}$$

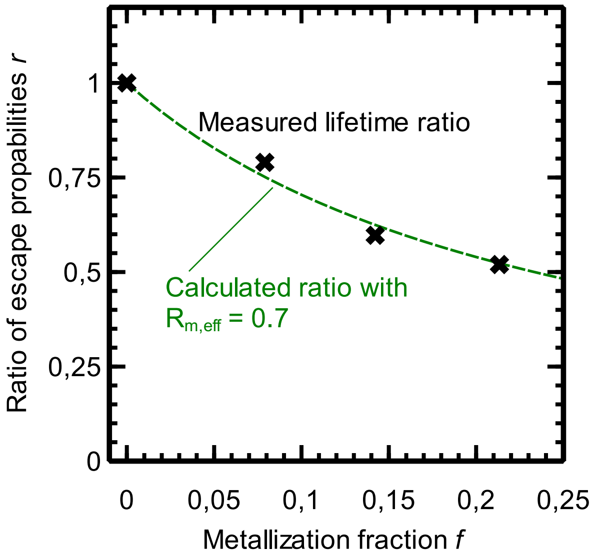

Figure 3.6: Measured (black crosses) and calculated (green dashed line) ratio of the IR photon escape probabilities for different metallization fractions compared to a non-metallized sample.

where f_{met} is the metallization fraction. As the IR photon energy (wavelength 3 μm to 5 μm) is smaller than the Si band gap and the dopant concentration is low compared to the highly doped regions we assume no IR absorption in the Si bulk.

We now calculate the emitted intensities due the IR light initially traveling up- and downwards. For this we collect intensities in a geometrical series first for the photons initially traveling upwards as shown in Fig. 3.7:

$$I_{\mathrm{em,u}} = I_{\mathrm{u}}(1-\mathcal{R}_{\mathrm{f}})\sum_{i=0}^{\infty}\mathcal{R}_{\mathrm{b}}{}^{i}\mathcal{R}_{\mathrm{f}}{}^{i} = \frac{I_{\mathrm{u}}(1-\mathcal{R}_{\mathrm{f}})}{1-\mathcal{R}_{\mathrm{b}}\mathcal{R}_{\mathrm{f}}} \tag{3.12}$$

The intensity from the light initially traveling downwards can be calculated similarly, but the first interaction is with the rear surface:

$$I_{\mathrm{em,d}} = \frac{I_{\mathrm{d}}\mathcal{R}_{\mathrm{b}}(1-\mathcal{R}_{\mathrm{f}})}{1-\mathcal{R}_{\mathrm{f}}\mathcal{R}_{\mathrm{b}}} \tag{3.13}$$

The total emitted intensity is the sum of both contributions:

$$I_{\mathrm{em}} = I_{\mathrm{em,u}} + I_{\mathrm{em,d}} = 0.5I_0(1-\mathcal{R}_{\mathrm{f}})\frac{1+\mathcal{R}_{\mathrm{b}}}{1-\mathcal{R}_{\mathrm{b}}\mathcal{R}_{\mathrm{f}}} \tag{3.14}$$

Because we are interested in relative changes rather than absolute intensities we calculate the ratio r of the emitted intensity and the intensity in a non-metallized area ($\mathcal{R}_{\mathrm{b}} = 1$),

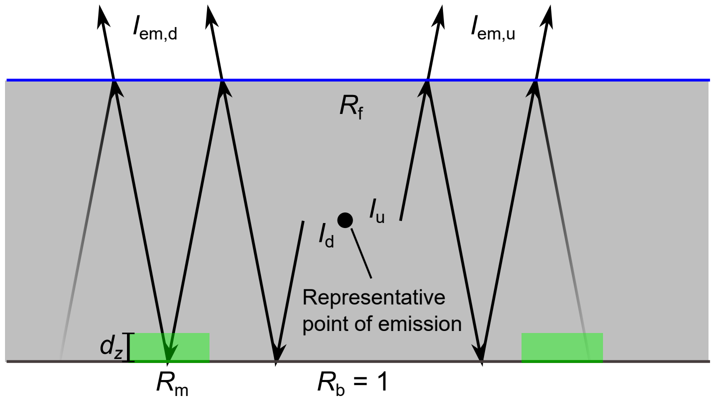

Figure 3.7: Schematic for the calculation of escape probabilities of IR photons in an ILM measurement. IR photons are emitted traveling upwards and downwards with equal intensities I_u and I_d. The escape probabilities are calculated using a geometrical series and an effective rear-side reflectivity.

where the calibration is correct:

$$r = \frac{I_{em}}{I_{em,f=0}} = 0.5(1 - \mathcal{R}_f)\frac{1 + \mathcal{R}_b}{1 - \mathcal{R}_b\mathcal{R}_f} \tag{3.15}$$

For the sample analyzed in this section we determine $\mathcal{R}_f$ to 0.93 with a ray-tracing simulation for diffusive light with a wavelength of 4000 nm. A fit of the calculated to the measured ratio yields $\mathcal{R}_{m,eff} = 0.7$ for the Al-BSF contacts on this sample, as shown in Fig. 3.6 with a green dashed line. The reduced reflectivity of the contacts can be explained by either a reduced reflectivity at the Si metal interface $\mathcal{R}_m$, by free carrier absorption or, most likely, by a combination of both effects. In the latter case we can calculated $\mathcal{R}_{m,eff}$ with:

$$\mathcal{R}_{m,eff} = \mathcal{R}_m e^{-2\alpha d_z} \tag{3.16}$$

where α is the absorption coefficient due to FCA in the highly doped areas and d_z is the thickness of the highly doped area. Both FCA and a reduced $\mathcal{R}_m$ can lead to a $\mathcal{R}_{m,eff} = 0.7$. If no FCA is present $\mathcal{R}_m = \mathcal{R}_{m,eff} = 0.7$. If $\mathcal{R}_m = 1$ the fit of term $e^{-2\alpha d_z} = 0.7$ for FCA yields $N_{dop} = 4.5 \cdot 10^{18}\,\mathrm{cm}^{-3}$, $\lambda = 4000\,\mathrm{nm}$ and $d_z = 9\,\mu\mathrm{m}$ using the parameterization for α at long wavelength from Schroder *et al.* [51]. Most likely, both effects contribute to $\mathcal{R}_{m,eff}$ with adapted parameters. The separation of the effects is, however, not possible.

In conclusion, the calibration of the static ILM measurement in the non-metallized areas is invalid due to the reduced effective reflectivity of the metal contacts. This reduced reflectivity can be explained by a combination of reduced reflectivity of the metal-Si interface and FCA in the highly doped regions underneath the contact.

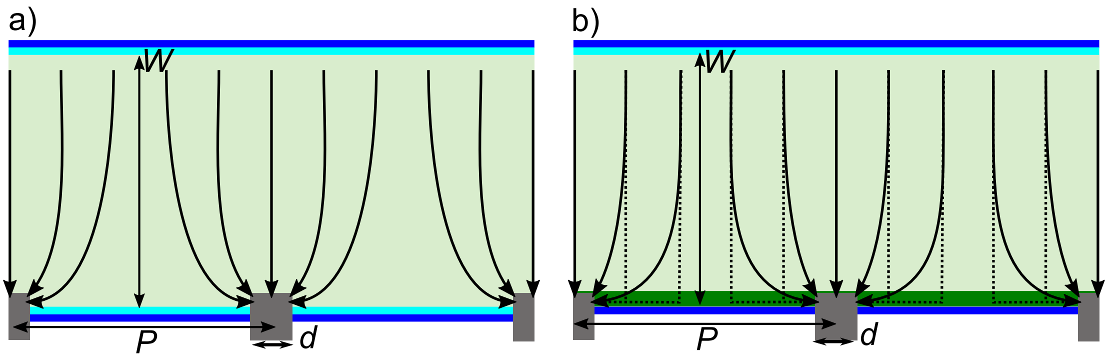

Figure 3.8: Current flow due to higher recombination at the contacts compared to the surrounding surface passivation in rear contacted test samples without highly diffused layers (a) and with a diffusion layer of the same polarity as the Si bulk underneath the contacts (b).

3.3 Evaluation methods

Extracting the contact recombination from the measured effective lifetime requires a description of the multi-dimensional current flow, internal resistances and recombination currents in other parts of the solar cell. Figure 3.8 shows a schematic for the internal current flow due to higher recombination at the contacts compared to the surrounding passivation without a diffused layer (a) and with a diffused layer underneath the contacts (b). There is no analytical solution of the semiconductor equations and, consequently, either a numerical simulation or analytical simplifications to the transport equations are required for extracting the contact recombination parameters.

3.3.1 Analytical description

The simplest analytical approach is to neglect all lateral inhomogeneities of Δn and of the current flow. In this case the Kane-Swanson evaluation method of QSSPC measurements (see section 2.4.4 on page 26) can be used to determine an average surface recombination and the contact recombination can be determined by the area-weighted subtraction of the surface recombination in the non-contacted areas. However, in Refs. 52 and 53 Dumbrell *et al.* compared the slope-based methods by Blum *et al.* [54] and the improvement proposed by Kimmerle *et al.* [55] to numerical Quokka simulations and showed that the assumption of a homogeneous Δn in partially metallized samples leads to an error in the determination of $J_{0,\mathrm{cont}}$ of up to a factor of 5 depending on the sample details. Therefore, this approach is not suited to extract $J_{0,\mathrm{cont}}$ values and a more suitable analytical description has to contain a description of the multi-dimensional current flow.

Such an approach was originally introduced by Fischer [56]. A detailed derivation of

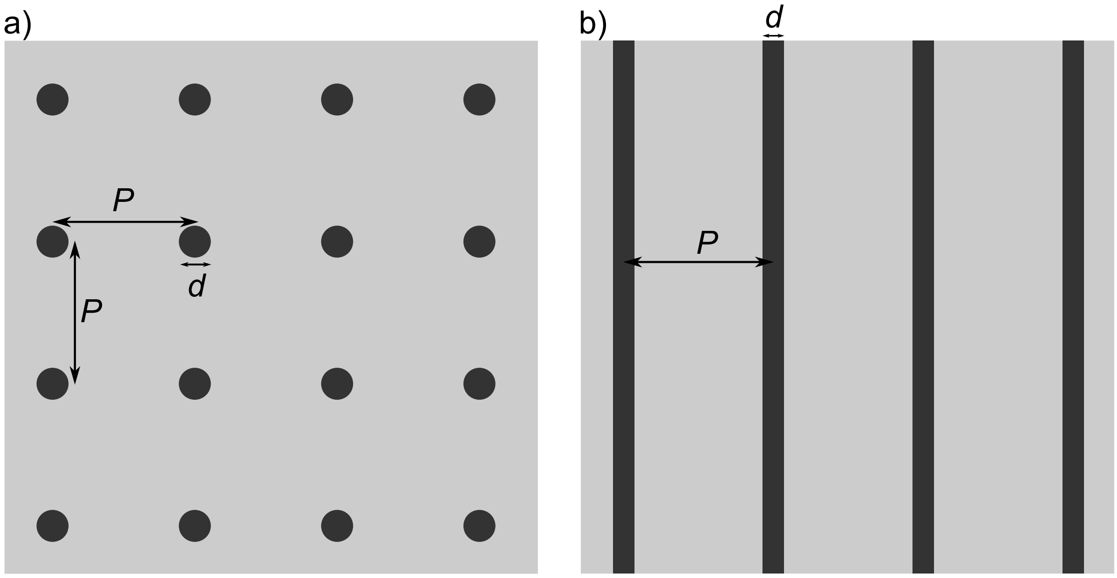

Figure 3.9: Schematics for the contact geometries that can be analyzed with an analytical approach: a) periodic arrangement of circular contacts with a distance P to the nearest contacts and a diameter d and b) full line contacts with a spacing P and a width d.

Fischer's model can be be found in Ref. 56. Here we are interested in the underlying assumptions and restrictions of the model and their consequences for determining contact recombination parameters. We are further interested in the accuracy of the model.

The derivation of Fischer's model can be divided into three steps: i) the simplification of the 3-D carrier transport to a 1-D model, ii) the calculation of an effective SRV $S_{\mathrm{eff,rear}}$ required for the 1-D model and iii) the calculation of the series resistance R_{series} required for $S_{\mathrm{eff,rear}}$. The calculation of $S_{\mathrm{eff,rear}}$ requires the calculation of the diffusion constant D, which can only be done analytically in low level injection. The calculation of $S_{\mathrm{eff,rear}}$ is further based on the assumptions that the diffusion length is much larger than the cell thickness. This requirement is usually met in today's mono-crystalline Si. It also requires a constant QFL splitting over the front surface. This requirement is fulfilled if we have sufficiently thick devices (over 150 μm) in combination with diffusion length much larger than the cell thickness, as is the case for our samples. The calculation of R_{series} has been done in various studies in the literature. All models are, however, restricted to either full line contacts [57, 58, 59] or a periodic arrangement of point contacts [56, 59, 60], which are shown in Fig 3.9 a) and b), respectively. The analysis of arbitrary contact geometries is, therefore, not possible in an analytical approach. If highly conductive diffusions are present, as for example in emitter structures or passivated emitter and rear totally diffused (PERT) cells, the models for R_{series} have to be adapted as shown in Ref. 61 for PERT structures with full line contacts. For contact geometries other

Table 3.2: Input parameters for Monte-Carlo simulation

Parameter	Value
W	150 to 250 μm
P	10 to 100 μm
f_{met}	0.0001 to 0.2
ρ_{b}	1 to 10 Ωcm
τ_{bulk}	200 to 1200 μs
S_{cont}	2 to 1000 cm/s
S_{pas} front	2 to 100 cm/s
S_{pas} rear	2 to 100 cm/s

than lines this adaption is not as straight forward, because the similarity to TLM theory can not be exploited. This imposes further restrictions on the structures that can be analyzed with this approach.

We check the accuracy of Fischer's model for analyzing contact recombination in PERC cells using a Monte-Carlo simulation with Quokka. We run 1000 simulations of the effective lifetime with parameters chosen randomly (with uniform distribution) from the ranges given in Tab. 3.2 and compare the results to Fischer's analytical model. The parameter ranges are chosen to represent modern PERC cells. We find an excellent agreement of Fischer's model and the Quokka simulations with deviations below 5%. This proves the applicability of Fischer's model for determining contact recombination parameters in PERC cells with either full-line contacts or point contacts arranged in a square pattern, provided low injection conditions are fulfilled.

3.3.2 Numerical evaluation of contact recombination

In this section we introduce an evaluation method solely based on Quokka. This allows an evaluation where the requirements of full line or point contacts and/or low level injection for Fischer's model are not fulfilled. This is the case for the PERC+ cells analyzed in section 4.3, because they feature dashed line contacts. We also want to study the injection dependency of contact recombination parameters for which we also need the numerical evaluation method.

For numerical modeling we need to define the sample under test within Quokka. The geometrical (thickness, contact width, etc.) and resistive properties (wafer and sheet resistances) are known from the sample processing or can be measured with the respective approaches described in chapter 2. For the optical definition we use a set of homogeneous generation currents to compute the injection dependency of the lifetime. The respective values have to be adapted to the measurement conditions used in the lifetime measurement, but we typically use 10 to 15 values in the range of 1 mA/cm^2 to 45 mA/cm^2.

All recombination parameters, the lifetime parameters for the Si bulk, the surface recombination parameter for the passivated surface $J_{0,\mathrm{pas}}$ and the contact recombination parameter $J_{0,\mathrm{cont}}$, have to be determined in a fitting routine. We model the bulk lifetime using a mid-gap SRH defect with corresponding lifetimes τ_{n0} and τ_{p0} or an injection independent lifetime τ_{bulk} (see section 1.3 on page 12). We first fit the lifetime parameters for the Si bulk and $J_{0,\mathrm{pas}}$ in the non-metallized area. The high lifetime in this area allows for a high accuracy of the determined parameters and are, except for inhomogeneities, representative for the entire sample. We then fit the measured lifetime curves in the metallized areas with an individual $J_{0,\mathrm{cont}}$ for each metallization fraction. We, therefore, obtain three $J_{0,\mathrm{cont}}$-values for the three metallized areas of our sample (see section 3.1.3 on page 35). We also determine a $J_{0,\mathrm{cont}}$-value that yields the best fit on all three areas. The comparison of these values gives us an impression of the uncertainty with which $J_{0,\mathrm{cont}}$ was determined. By comparing the measured and simulated lifetime curves for the determined $J_{0,\mathrm{cont}}$ we can further asses the quality of the $J_{0,\mathrm{cont}}$ determination. An application example of this method is given in section 4.3.

Correct description of injection dependent contact recombination

One advantage of the numerical approach described above is that the contact recombination can be analyzed over the entire measured injection range. Here we analyze a sample, which consists of n-type Si with a symmetric n-type diffusion with Ag contacts on a selective diffusion on one side. The contact lines are 40 μm wide with a pitch of 450 μm. Figure 3.10 shows a measurement of the effective lifetime (black crosses) along with simulations of the effective lifetime using the J_0-model (blue line) and the S-model (green line)(see equations 1.12 and 1.13 on page 13 for details on the J_0- and S-description). It is apparent that neither the J_0-description nor the S-description is suited to describe the injection dependency of the contact recombination in this case. In the following we discuss the physical reason why neither model describes the injection dependency correctly and propose an improved parameterization using two parameters.

As discussed in section 1.3.2 the recombination in a highly diffused layer can be described using the J_0-model. However, such a layer is usually passivated and, consequently, the recombination at the surface of the diffused layer is small when compared to the recombination within the layer. However, when a metal is applied, the recombination at the surface may contribute significantly to the total recombination. For our model we assume that the recombination at the Si-metal interface can be described by the S-model (i.e. is injection independent), because the recombination relies on the SRH-defects at the surface and is in low level injection due to the large dopant concentration in the diffused layer. The total recombination into the boundary is the sum of the recombination within the diffused layer and the recombination at the surface:

$$J_{\mathrm{rec}} = J_{\mathrm{rec,diff}} + J_{\mathrm{rec,surf}} \tag{3.17}$$

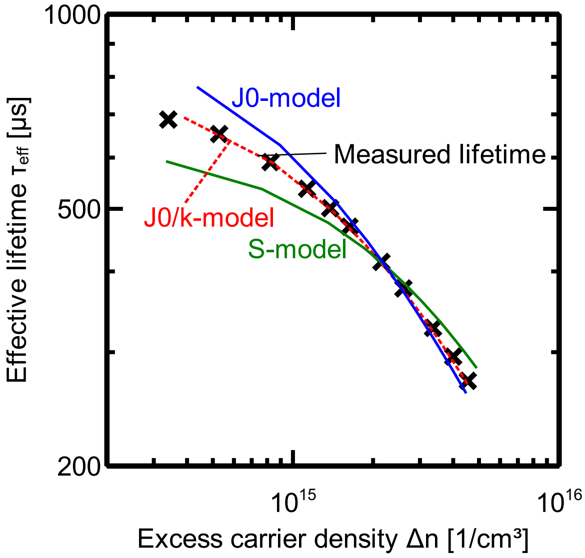

Figure 3.10: Measured (black crosses) and simulated lifetime curves of a sample contacted with Ag contacts. The colored lines show the simulated lifetimes for the J_0-model (blue line), the S-model (green line) and the J_0/k-model (red dashed line) developed in this work for modeling contact recombination.

The recombination within the diffused layer can be described by the J_0-model:

$$J_{\text{rec,diff}} = J_0 \frac{np}{{n_i}^2} = J_0 \frac{\Delta n N_{\text{dop}} + \Delta n^2}{{n_i}^2} \tag{3.18}$$

It should be noted that the carrier and dopant densities are taken at the interface of the Si bulk and the diffused layer. The recombination at the surface is described by:

$$J_{\text{rec,surf}} = Sq\Delta n_{\text{surf}} \tag{3.19}$$

here the relevant excess carrier density is that at the Si-metal interface. This Δn_{surf} depends on the recombination within the diffused layer or, more precisely, the thickness and the diffusion length of the diffused layer. As the depth of the diffused layer is not resolved in Quokka, we approximate this value using a linear interpolation between both extreme cases of $L_{\text{Ddiff}} << W_{\text{diff}}$ and $L_{\text{Ddiff}} >> W_{\text{diff}}$. When $L_{\text{Ddiff}} << W_{\text{diff}}$ we have strong recombination within the highly diffused layer and $\Delta n_{\text{surf}} \approx 0$. When $L_{\text{Ddiff}} >> W_{\text{diff}}$ we have very little recombination and the QFLs are approximately flat, which means that the np-product is approximately constant

$$\begin{aligned} n_{\text{surf}} p_{\text{surf}} &= np \\ \implies N_{\text{surf}} \Delta n_{\text{surf}} + \Delta n_{\text{surf}}^2 &= N_{\text{dop}} \Delta n + \Delta n^2, \end{aligned} \tag{3.20}$$

where N_{dop} is the dopant concentration in the wafer and N_{surf} is the dopant concentration in the highly diffused layer. In low injection we have

$$\Delta n_{\text{surf}} = \frac{N_{\text{dop}}}{N_{\text{surf}}} \Delta n. \tag{3.21}$$

For the interpolation between both extreme cases we calculate Δn_{surf} as

$$\Delta n_{\text{surf}} = \Delta n \frac{N_{\text{dop}} L_{\text{Ddiff}}}{N_{\text{surf}}(L_{\text{Ddiff}} + W_{\text{diff}})}. \tag{3.22}$$

Consequently, we determine the total recombination to:

$$\begin{aligned} J_{\text{rec}} &= J_0 \frac{\Delta n N_{\text{dop}} + \Delta n^2}{{n_i}^2} + Sq\Delta n \frac{N_{\text{dop}} L_{\text{Ddiff}}}{N_{\text{surf}}(L_{\text{Ddiff}} + W_{\text{diff}})} \\ &= J_0 \left(\left(\frac{Sq{n_i}^2}{J_0} \frac{L_{\text{Ddiff}}}{N_{\text{surf}}(L_{\text{Ddiff}} + W_{\text{diff}})} + 1 \right) \frac{N_{\text{dop}} \Delta n}{{n_i}^2} + \frac{\Delta n^2}{{n_i}^2} \right) \\ &= J_0 \frac{(k N_{\text{dop}} \Delta n + \Delta n^2)}{{n_i}^2}. \end{aligned} \tag{3.23}$$

Here we introduce the asymmetry factor

$$k = \frac{Sq{n_i}^2}{J_0} \frac{L_{\text{Ddiff}}}{N_{\text{dop}}(L_{\text{Ddiff}} + W_{\text{diff}})} + 1, \tag{3.24}$$

which is a parameter describing the deviation in the injection dependency of the contact recombination from the J_0-description. It contains three relevant factors: 1.) the ratio between J_0 and S, 2.) the dopant density in the highly doped layer and 3.) the ratio between diffusion length and thickness of the diffused layer. Consequently, the surface recombination is negligible in three cases: 1.) The recombination within the diffused surface is much stronger than at the surface (as is the case for e.g. a passivated surface), 2.) A high dopant density in the diffused layers reduces the excess carrier density at the surface to negligible values or 3.) The diffused layer is much thicker than the diffusion length within the layer. In these cases k equals 1 and the total recombination into the boundary can be accurately described by the J_0-model.

In our measurement evaluation we use k as a second fit parameter besides J_0. The red dashed line in Fig. 3.10 shows a fit with the J_0/k-model to the measurement and we see an excellent agreement with the measurement. We determine a value of 2.5 for k and 600 fA/cm^2 for J_0. To check whether this value agrees with eq. 3.24, we calculate k with eq. 3.24 using estimated values. The dopant concentrations in the highly diffused selective emitter underneath the metal is approximately $10^{20}\,\text{cm}^{-3}$. With an emitter thickness of less than 1 μm and a diffusion length in the emitter of 10 μm to 20 μm we can assume $L_{\text{Ddiff}} >> W_{\text{diff}}$. For J_0 we take the fitted value of 600 fA/cm^2 and for S at the Si-metal interface we take a value of 10^7 cm/s. For n_i we take $9 \cdot 10^9\,\text{cm}^{-3}$.

Inserting these values in eq. 3.24 yields $k \approx 3$, which agrees reasonably well with fitted $k = 2.5$, given the rough estimate for the parameters. In this example, the Si-metal interface causes additional recombination in low injection that is 1.5 times higher than the recombination in the highly diffused layer (60% of the total recombination). This value seems to be reasonable, because the recombination in the highly diffused layer is reduced significantly in low injection and the Si-metal interface is expected to contribute a large fraction of the contact recombination.

3.4 Summary: Determination of contact recombination parameters

The extraction of contact recombination parameters from lifetime measurements is a challenging task. In general this challenge is met by comparing the lifetimes for different metallization fractions. We analyzed samples structures, measurement techniques and evaluation methods for their applicability to this task. The best choice for a metallization pattern depends on the lifetime sample used. In this work we use a pattern with four areas, one not metallized and three with different metallization fractions. We found this pattern to be best suited for our lifetime samples, which have moderate inhomogeneities, which are, to a large fraction, rotational symmetric. If both electron and hole conducting layers are present the coupling between regions of different lifetime must be considered. To this end, we derived an analytical formula to estimate the length scale on which the coupling affects the respective lifetimes. In this work we use n-type diffusions in n-type wafers or p-type diffusions in p-type wafers.

For the measurement of partially metallized samples three methods were compared in this chapter: PC-PLI, static ILM and dynamic ILM. We found PC-PLI to be best suited for this task because of the low uncertainty of the static measurement. The dynamic ILM approach yields similar results but with higher uncertainties due to deviation of the dynamic approach caused by injection dependent, inhomogeneous or low lifetimes. The static ILM yields wrong results with a deviation of up to 50% due to the reduced emission of photons for higher metallization fractions. This can be explained with the enhanced IR absorption at the Si-metal interface and/or FCA in the highly doped regions underneath the contact.

For the extraction of recombination parameters from spatially resolved lifetime measurements the internal resistances of the sample must be considered. A simple area averaging approach yields results wrong by up to a factor of 5 [29]. We found the model by Fischer to be accurate within 5% provided the assumptions of low level injection and long diffusion lengths are fulfilled. Furthermore, the model is restricted to either full line or point contacts arranged in a square pattern. Because the cells we investigate in section 4.3 have dashed line contacts, we also introduced a numerical evaluation approach based on Quokka. The recombination properties other than those at the contacts are determined in a non-contacted field. The contact recombination parameters are then determined in the remaining fields by fitting the measured lifetime with individual $J_{0,\mathrm{cont}}$ for each field. This also yields an estimate for the uncertainty of the determined value. Using this method, we found that in some cases the injection dependency of the contact recombination can be neither described with the J_0-model nor with the S-model. We identified the origin for this deviation in the combination of two recombination currents: the recombination in the highly diffused layer, which follows the J_0-model and the recombination at the Si-metal interface, which can be accurately described with the S-model. We derived a new parameterization, the J_0/k-model, which uses two parameters to accurately describe the contact recombination.

4 Application of loss analyses to industrial solar cells

In this chapter we show the application of modeling-based loss and gain analyses to state-of-the-art PERC+ cells. We analyze the differences between SEGA as a gain and FELA as a loss analysis. We further present a simulation tool, which was created in the context of this work and automatically performs SEGAs and parameter variations. We then show the complete analysis of an industrial-type PERC+ solar cell starting with the test structures and characterization of the cell batch including an analysis of the expected uncertainties. We further show how these input parameters are used to calculate a SEGA and how the uncertainties in the input parameters translate to uncertainties in the simulation results.

4.1 Comparison of FELA and SEGA

The content presented in this section was previously published in Ref. 62.

FELA and SEGA are both simulation-based analyses to identify routes for further cell improvements and both quantify optical losses, transport losses and recombination losses in units of power per area. However, there also is an import difference between both approaches. The SEGA is a gain analysis whereas the FELA is a loss analysis. A gain is defined as the efficiency that is gained if a loss channel is deactivated. A loss, on the other hand, is a loss of a specific quantity at the operating point of the solar cell under test. In case of the FELA this quantity is the rate of free energy. In other words, the SEGA calculates the efficiency loss at the maximum power point relative to a cell without that loss, whereas the FELA calculates the free energy loss rate. Both analyses are frequently used in solar cell optimization [63, 64, 65, 66], which raises the question of possible differences in the results. In solar cell optimization, researchers are always interested in the efficiency gain that can be achieved by optimizing a specific cell property. This gain is determined by the SEGA. However, the FELA is considerably faster as only one simulation is needed for all loss channels. Here we analyze the differences of both approaches.

Figure 4.2 shows the results of a SEGA (a) and a FELA (b) for a 21%-efficient PERC cell shown in Fig. 4.1 both expressed in $\mathrm{mW/cm^2}$. The optical, recombination and resistive losses are shown with green, red and blue bars, respectively. The optical and resistive losses calculated by both approaches agree well with less than 0.02 $\mathrm{mW/cm^2}$

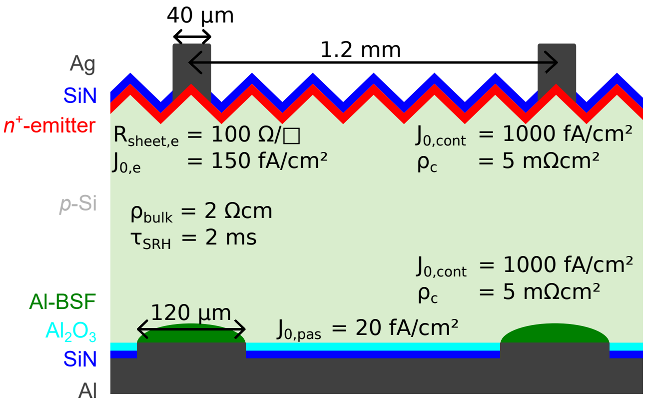

Figure 4.1: PERC schematic with input parameters for the comparison of FELA and SEGA in Fig. 4.2. Figure reprinted from Ref. 62.

difference. However, the optical losses due to rear surface reflection, lambertian light trapping and free carrier absorption calculated in the SEGA are not determined in the FELA, because the required wavelength dependent generation is not available in our simulation. The recombination losses show larger deviations especially for the largest recombination channel, which, in this case, is the emitter recombination. The loss due to emitter recombination is 0.75 mW/cm^2 as calculated with the SEGA, with the FELA the loss results to only 0.56 mW/cm^2. The sum of all recombination losses amounts to 1.31 mW/cm^2 in the SEGA and 1.13 mW/cm^2 in the FELA. In addition, the SEGA calculates synergistic gains, which amount to 3.21 mW/cm^2 for the recombination losses. For the optical losses the synergy amounts to 0.09 mW/cm^2 while for the resistive losses the synergy is negligible. There are also synergy effects between the three groups, which amount to 0.56 mW/cm^2 shown as a black bar. The sum of the 21% reference efficiency and all efficiency gains yields 28.94% efficiency, which is the efficiency limit for the cell thickness of 170 μm and a base resistivity of 2 Ωcm.

4.1.1 Monte-Carlo simulation for recombination channels

From the comparison in Fig. 4.2 it is clear that the SEGA and FELA can yield different results for the recombination channels. To better understand the magnitude and origin of these deviations we run a Monte-Carlo simulation with random recombination parameters with values from the ranges given in Tab. 4.1. The remaining parameters are chosen as shown in Fig. 4.1.

The results are shown in Fig. 4.3. The FELA yields smaller losses in cases of large recombination at the front side of the cell (red data points). For recombination loss channels located at the rear side of the solar cell (green data points), the FELA yields larger losses for power losses up to 0.5 mW/cm^2. The FELA also yields larger losses for recombination in the absorber (blue data points).

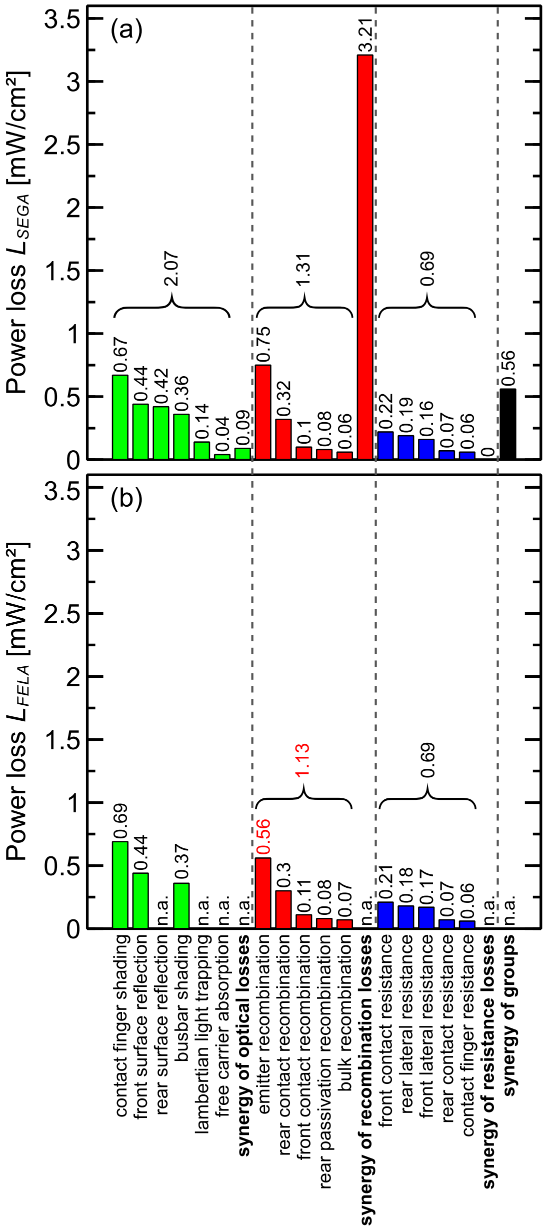

Figure 4.2: SEGA (top) and FELA (bottom) for an example PERC test structure shown in Fig. 4.1. Optical losses are shown in green, recombination losses in red and resistive losses in blue. Figure reprinted from Ref. 62

The dashed lines in Fig. 4.3 show a 20 % deviation of the FELA loss compared to the SEGA gain. Most data points for the power loss due to rear-side and absorber recombination show less than 20 % deviation for power losses up to 0.8 mW/cm^2 as calculated with the FELA. For power losses at the front side the deviation between

Table 4.1: Ranges from which each recombination parameter is chosen for the comparison of FELA and SEGA in Fig. 4.3

Recombination parameter	Range
Bulk carrier lifetime	55 to 2000 μs
Emitter recombination	4 to 1000 fA/cm^2
Front contact recombination	4 to 35000 fA/cm^2
Rear passivation recombination	4 to 600 fA/cm^2
Rear contact recombination	4 to 20000 fA/cm^2

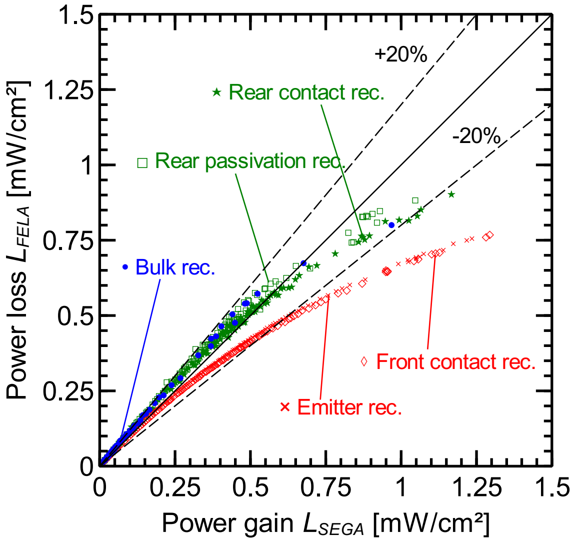

Figure 4.3: Comparison of SEGA and FELA results for random recombination properties in a PERC solar cell structure. Front-side losses are shown in red, rear-side losses in green and bulk losses in blue. Figure reprinted from Ref. 62.

FELA and SEGA is only within 20 % for FELA losses up to 0.4 mW/cm^2. It should be noted, however, that the relative deviation of FELA losses can amount up to 40 % as rear-side and bulk losses are determined larger while front-side losses are determined smaller. Deviations of this magnitude could possibly lead to major differences in the strategy for further cell improvements and should, therefore, be understood.

4.1.2 Analytical description

In this section we employ the analytical description of FELA and SEGA losses to understand the origin of the deviation between both approaches. The power loss per area as calculated with the SEGA in terms of free energy follows from equation (1.2):

$$\begin{aligned}L_{\mathrm{SEGA}} = &\ (\eta_{\mathrm{nl}} - \eta_{\mathrm{wl}})P_{\mathrm{IN}} \\ = &\ (\dot{F}_{\mathrm{G,nl}} - \dot{F}_{\mathrm{R,nl}} - \dot{F}_{\mathrm{T,nl}}) \\ &-(\dot{F}_{\mathrm{G,wl}} - \dot{F}_{\mathrm{R,wl}} - \dot{F}_{\mathrm{T,wl}}).\end{aligned} \tag{4.1}$$

The indices nl and wl stand for the simulations with no loss and with loss, respectively. We simplify (4.1) by neglecting any differences in the power losses due to charge carrier transport. The differences of the generated power and the power lost due to recombination sum up to the SEGA power loss

$$L_{\mathrm{SEGA}} = (\dot{F}_{\mathrm{G,nl}} - \dot{F}_{\mathrm{G,wl}}) - (\dot{F}_{\mathrm{R,nl}} - \dot{F}_{\mathrm{R,wl}}). \tag{4.2}$$

We calculate all terms in (4.2) by multiplying the generation or recombination current with the local Fermi level splitting in the respective simulation (nl or wl). The photogenerated current J_{Gen} is equal in both simulations. We calculate the recombination current J_{rec} in the i-th recombination channel using equation (1.12), which yields $J_{\mathrm{rec}} = J_{0,i}e^{\beta\Delta\phi}$, where β is the inverse thermal voltage. It should be noted that the Fermi level splitting $\Delta\phi$ depends on the location within the cell. Consequently, the calculation of the total recombination current requires an integral over the volume of interest. However, to simplify the further calculations, we neglect the local character of the Fermi level splitting and take the average Fermi level splitting (internal voltage) V as an approximation.

Let the analyzed loss channel be channel one such that $J_{0,i,\mathrm{nl}} = J_{0,i,\mathrm{wl}} = J_{0,i}$ for all $2 \leq i \leq N$, where N is the total number of recombination channels. Then we can write (4.2) as

$$\begin{aligned}L_{\mathrm{SEGA}} = &\ J_{\mathrm{Gen}}(V_{\mathrm{nl}} - V_{\mathrm{wl}}) \\ &- \sum_{i=2}^{N} J_{0,i}(V_{\mathrm{nl}}e^{\beta V_{\mathrm{nl}}} - V_{\mathrm{wl}}e^{\beta V_{\mathrm{wl}}}) \\ &+ J_{0,1}V_{\mathrm{wl}}e^{\beta V_{\mathrm{wl}}}.\end{aligned} \tag{4.3}$$

The last term $J_{0,1}V_{\mathrm{wl}}e^{\beta V_{\mathrm{wl}}}$ in (4.3) is the power loss L_{FELA} as calculated by the FELA. The deviation between the power losses calculated with both approaches is thus

$$\begin{aligned}L_{\mathrm{SEGA}} - L_{\mathrm{FELA}} = &\ J_{\mathrm{Gen}}(V_{\mathrm{nl}} - V_{\mathrm{wl}}) \\ &- \sum_{i=2}^{N} J_{0,i}(V_{\mathrm{nl}}e^{\beta V_{\mathrm{nl}}} - V_{\mathrm{wl}}e^{\beta V_{\mathrm{wl}}}).\end{aligned} \tag{4.4}$$

Table 4.2: Recombination parameters for the PERC cell analyzed in Fig. 4.4

Recombination parameter	Value
Bulk carrier lifetime	55 μs
J_0 emitter recombination	1000 fA/cm^2
J_0 front contact recombination	35000 fA/cm^2
J_0 rear passivation recombination	600 fA/cm^2
J_0 rear contact recombination	20000 fA/cm^2

V is larger for the cell with less recombination. To simplify (4.4) further, we introduce $\Delta V = V_{\mathrm{nl}} - V_{\mathrm{wl}}$. We write (4.4) as

$$\begin{aligned} L_{\mathrm{SEGA}} - L_{\mathrm{FELA}} &= J_{\mathrm{Gen}} \Delta V \\ &\quad - \sum_{i=2}^{N} J_{0,i} V_{\mathrm{wl}} e^{\beta V_{\mathrm{wl}}} ((1 + \frac{\Delta V}{V_{\mathrm{wl}}}) e^{\beta \Delta V} - 1), \end{aligned} \tag{4.5}$$

and because the difference of the internal voltages ΔV is usually small compared to V we can write

$$\begin{aligned} L_{\mathrm{SEGA}} - L_{\mathrm{FELA}} &\approx J_{\mathrm{Gen}} \Delta V \\ &\quad - \sum_{i=2}^{N} L_{\mathrm{FELA},J_{0,i}} \cdot (e^{\beta \Delta V} - 1), \end{aligned} \tag{4.6}$$

where we used $L_{\mathrm{FELA},J_{0,i}} = J_{0,i} V_{\mathrm{wl}} e^{\beta V_{\mathrm{wl}}}$. We see that the difference $L_{\mathrm{SEGA}} - L_{\mathrm{FELA}}$ between both analyses rises solely from an increase of the internal voltage, which does not show up in the FELA approach. This increase of the internal voltage leads to an increase of generated free energy as described by the first term in (4.6). In contrast, the second term describes the increased recombination losses in other channels due to the increased internal voltage when eliminating a specific loss. While the increase of generated free energy contributes to an underestimation of the losses by the FELA with respect to SEGA, the increased losses in other recombination channels contribute to an overestimation. Depending on which of these terms is dominating, the FELA can either over- or underestimate the implied power gain.

In our derivation of equation (4.6) we approximated the Fermi level splitting $\Delta\phi(\vec{x})$ by the average Fermi level splitting V. While this approximation is useful for understanding the origin of the under- and overestimation, it fails to explain the differences between front- and rear-side losses. Figure 4.4 shows the Fermi level splitting increase ΔV in the non-contacted area of an example cell simulated without emitter recombination (red line) and without recombination at the rear-side passivation (green line). The

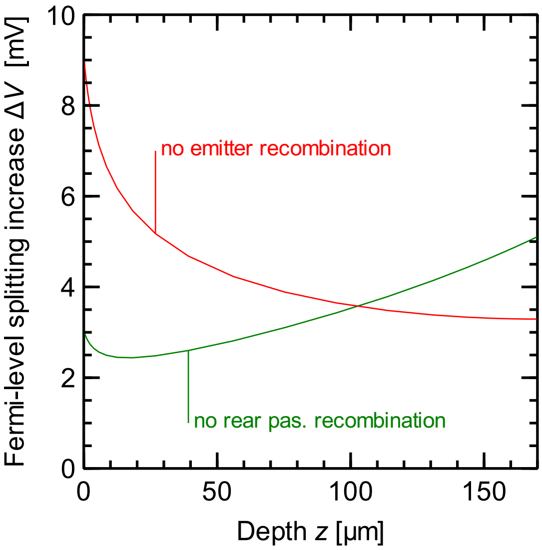

Figure 4.4: The increase of the Fermi level splitting in the non-contacted area of an example cell with strong recombination in all loss channels. The recombination parameters of this cell can be found in Tab. in 4.2. The red line shows the Fermi level increase when avoiding the emitter recombination. The green line shows the increase for avoiding recombination at the rear-side passivation. The front side is at $z = 0$.

differences of the Fermi levels are more pronounced for larger recombination currents within the cell. To improve the clarity of the qualitative analysis of the Fermi levels we use exaggerated recombination parameters, which can be found in Tab. 4.2. All other parameters are the same as in Fig. 4.1. It should be noted that the SEGA gains due to recombination within the emitter and at the rear-side passivation are approximately the same (0.340 mW/cm^2 versus 0.334 mW/cm^2, respectively) for this cell. In comparison, the FELA losses show large differences and a different ranking of the losses (0.309 mW/cm^2 versus 0.429 mW/cm^2). We see that avoiding the emitter recombination affects the change of the local Fermi level differently than avoiding recombination at the rear-side passivation. Avoiding the emitter recombination leads to a strong increase of the Fermi level splitting at the front side of the cell, which rapidly decreases with the cell depth. This leads to a stronger increase of generated free energy compared to the increased losses in other recombination channels (at the back) and, consequently, an underestimation of the implied gain by the FELA. For the ideal rear passivation the increase of the Fermi level is more evenly spread over the cell depth leading to a stronger increase of free energy losses in other recombination channels (at the front) when compared to the increase of generated free energy. This corresponds to an overestimation of the implied gain by the FELA.

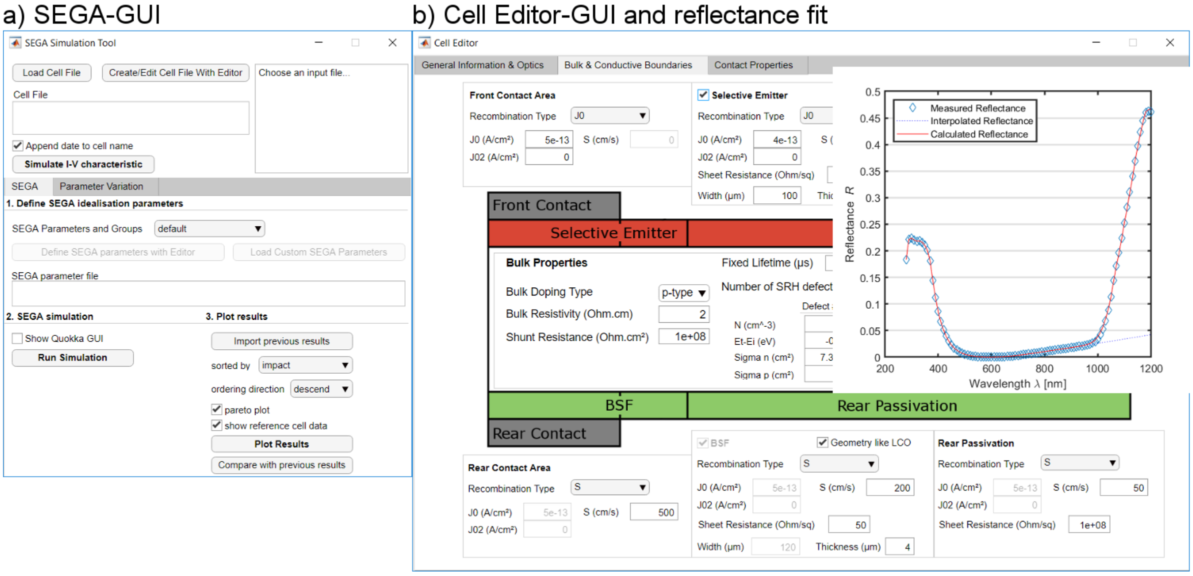
a) SEGA-GUI

b) Cell Editor-GUI and reflectance fit

☑ Append date to cell name

SEGA Parameters and Groups: default ▼

☐ Show Quokka GUI

sorted by: impact ▼

ordering direction: descend ▼

☑ pareto plot

☑ show reference cell data

Front Contact Area
Recombination Type: J0 ▼
J0 (A/cm²): 5e-13
S (cm/s): 0
J02 (A/cm²): 0

☑ Selective Emitter
Recombination Type: J0
J0 (A/cm²): 4e-13
J02 (A/cm²): 0
Width (µm): 100

Bulk Properties
Bulk Doping Type: p-type ▼
Bulk Resistivity (Ohm.cm): 2
Shunt Resistance (Ohm.cm²): 1e+08
Fixed Lifetime (µs)
N (cm^-3)
Et-Ei (eV)
Sigma n (cm²): 7.3
Sigma p (cm²)

Rear Contact Area
Recombination Type: S ▼
J0 (A/cm²): 5e-13
S (cm/s): 500
J02 (A/cm²): 0

☑ BSF
☑ Geometry like LCO
Recombination Type: S ▼
J0 (A/cm²): 5e-13
S (cm/s): 200
J02 (A/cm²): 0
Sheet Resistance (Ohm/sq): 50
Width (µm): 120
Thickness (µm): 4

Rear Passivation
Recombination Type: S ▼
J0 (A/cm²): 5e-13
S (cm/s): 50
J02 (A/cm²): 0
Sheet Resistance (Ohm/sq): 1e+08

Figure 4.5: a) Screenshot of the SEGA-GUI for a fully automatic SEGA, b) GUI for entering the input parameters and automatically fitting a measured reflectance to the optical model in section 2.3 (inset). The blue diamonds show the measured reflectance and the red solid line the fitted model.

In summary, the FELA is a useful tool for obtaining a quick overview over the losses present in the analyzed solar cell. For the PERC cells discussed here resistive losses as well as small recombination losses calculated by the FELA can be used as good estimates for the implied efficiency gain potential of the respective loss channel. However, large individual recombination losses can be under- or overestimated considerably by the FELA. Thus, in a cell with multiple recombination loss channels of comparable magnitude, the SEGA quantifies more reliably the potential for efficiency improvements by each loss channel.

4.2 SEGA-GUI

Performing a SEGA analysis requires about 20 individual device simulations. To reduce the required amount of work that has to be put into such an analysis a graphical user interface (GUI), shown in Fig. 4.5 a), was designed in this thesis that automatically carries out all of the SEGA simulations. It further allows for automatic parameter variations. This SEGA-GUI has implemented various important cell structures such as PERC, passivated emitter rear totally diffused back junction cells (PERT-BJ), interdigitated back contact cells (IBC) and variations of these cell designs such as front and rear contacted cells bi-facial cells.

For a SEGA simulation the user first enters all necessary experimental input parameters and then the SEGA-GUI creates the required set of input files. The SEGA-GUI then performs the simulations by running Quokka 2 and displays the results. Programming knowledge is not required. The SEGA-GUI was designed to help the user in finding options for efficiency improvements. It further features a GUI for creating the required input files, which is shown in Fig. 4.5 b). This GUI allows to input values for geometric properties, lifetimes, including different defect and recombination models, and resistive properties. It further allows to automatically fit the optical model presented in section 2.3 to a measured reflectance curve. An example for a reflectance fit created by this GUI is also shown in Fig. 4.5 b). The measured reflectance spectrum is shown with blue diamonds along with the extrapolated front surface reflectance in the near infrared spectral range (blue dotted line) and the fitted modeled reflectance (red line). We made the SEGA-GUI available for the scientific community [8]. The SEGA-GUI can be downloaded for free from the ISFH website: `http://www.isfh.de/tools/SEGA-GUI`.

4.3 Application example: PERC+ solar cell

In this section we apply the measurement and simulation techniques introduced before for a complete characterization and SEGA analysis of a PERC+ cell batch.

4.3.1 Processing cells and test structures

For the characterization of the PERC+ cell batch we require six types of test structures: 1) "iV_{OC}-samples", which are samples that are not metallized and haves no LCOs but are otherwise identical to the cells, 2) "$J_{0,\mathrm{e}}$-samples" for determining the emitter recombination, 3) "$J_{0,\mathrm{Ag}}$-samples" for determining recombination at the front Ag-contacts, 4) "τ_{bulk}-samples" for determining the bulk lifetime, 5) "$J_{0,\mathrm{pas}}$-samples" for determining recombination at the surface passivation and 6) "$J_{0,\mathrm{Al}}$-samples" for determining recombination at the rear Al-contacts. The iV_{OC}-samples contain all recombination channels except for the contacts. They are not necessarily required for the characterization in this work but serve as redundancy in case the $J_{0,\mathrm{e}}$-, τ_{bulk}- or $J_{0,\mathrm{pas}}$-samples show faults. More information on the requirements for the test structures can be found in chapters 2 and 3.

Figure 4.6 shows the process sequences for the cell and all test structures. The solar cells (first column in Fig. 4.6) are processed on 0.9 Ωcm B-doped Cz-material with a thickness of 161 μm. After initial cleaning a protective SiN layer is deposited as an etch barrier onto the rear side. Front-side texturing and shallow phosphorus diffusion follow. Then the designated contact areas are laser-doped for forming the selective emitter. After that the protective SiN-layer is removed and a SiN-layer for anti-reflection and passivation is applied to the front side. Next the Al_2O_3 and SiN for the rear-side passivation are applied using atomic layer deposition and plasma enhanced chemical vapor deposition, respectively. The last step is applying the contacts by first opening

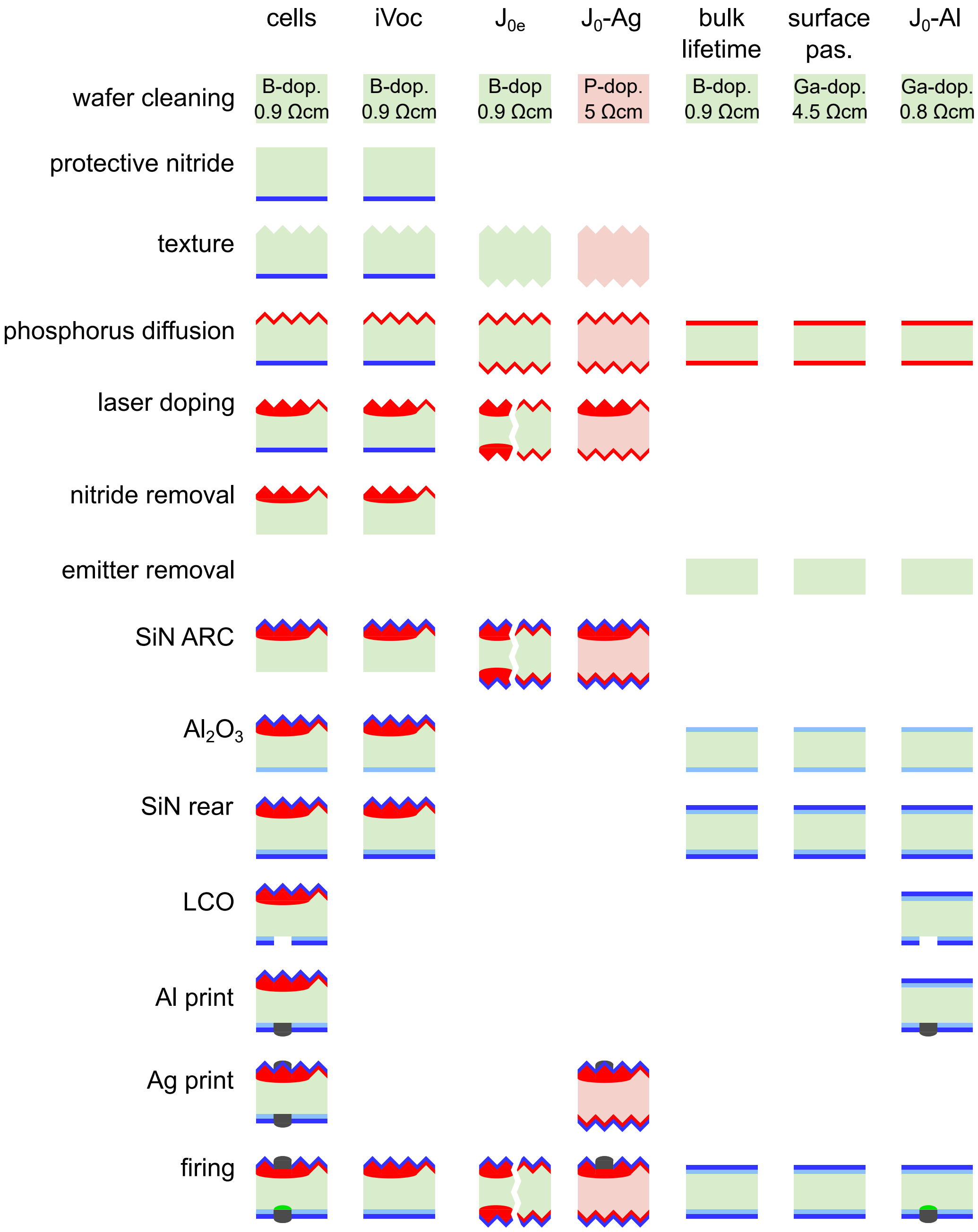

Figure 4.6: Process sequences for the analyzed PERC+ cells and the required test structures. From top to bottom each image represents a process step for which the label is shown on the left. A missing image means that the process step is not required for the respective sample. The columns show the sequences for the cell and the six different types of test structures. The $J_{0,e}$-samples in the third column receive laser-doping only for two of the four quarters, which is indicated by the separation of the two sample areas.

the contact areas on the rear side using a laser (LCO) and then screen-printing an Al grid on the rear- and an Ag grid on the front side. After that the cells are treated with a short term anealing step called firing to form the contacts. The iV_{OC}-samples (second column in Fig. 4.6) are manufactured the same as the cells except for the LCO and metallization steps, which are omitted.

The $J_{0,\mathrm{e}}$-samples (third column in Fig. 4.6) are processed without protective SiN leading to a symmetric texture and phosphorus diffusion. The samples are divided into quarters, two with full area laser-doping on both sides and two without laser-doping. The surfaces are passivated with SiN and then fired. The $J_{0,\mathrm{Ag}}$-samples (fourth column in Fig. 4.6) are processed on 5 Ωcm P-doped Cz-material to avoid lateral coupling as discussed in section 3.1.2 on page 31. The samples are processed symmetrically by omitting the protective SiN, the rear passivation and the rear metallization steps. The Ag-contact pattern consists of 4 areas as shown in Fig. 3.4 b). The respective contact pitches are 450 μm, 900 μm and 1350 μm. Laser doping is only applied to the areas underneath the contacts.

The τ_{bulk}-samples (fifth column in Fig. 4.6) and the $J_{0,\mathrm{pas}}$-samples (sixth column in Fig. 4.6) are processed identically but on different bulk-materials. The τ_{bulk}-samples are processed on the same 0.9 Ωcm boron-doped material as the cells. The material for the $J_{0,\mathrm{pas}}$-samples is Ga-doped with 4.5 Ωcm because the higher resistivity enhances the accuracy of the Kane-Swanson analysis as described in section 2.4.4 on page 26. Both types of samples receive a phosphorus emitter diffusion, which is removed in the next step, in order to getter impurities from the bulk into the highly diffused layer. After that an $\mathrm{Al_2O_3}$/SiN passivation is applied to both sides of the samples, which are then fired. The $J_{0,\mathrm{Al}}$-samples are processed identical to the τ_{bulk}-samples and $J_{0,\mathrm{pas}}$-samples but on 0.8 Ωcm Ga-doped material because it provides the best lifetime of our available p-type material. After the passivation steps, LCOs and metal are applied on the rear side of the samples, which are then fired. The metallization pattern is again that shown in Fig. 3.4 b) with contact pitches of 300 μm, 450 μm and 810 μm. The LCOs are 46 μm-wide dashed lines with 300 μm dash length and 900 μm dash pitch as shown in Fig. 4.7.

For the estimation of process-related uncertainties in the determined values we process multiple samples of each type: 10 solar cells, 4 iV_{OC}-samples, 3 $J_{0,\mathrm{e}}$-samples, 4 $J_{0,\mathrm{Ag}}$-samples, τ_{bulk}-samples, 5 $J_{0,\mathrm{pas}}$-samples and 5 $J_{0,\mathrm{Al}}$-samples. It should be noted that we aimed at 10 solar cells and 5 of each test structure, but some samples did not survive the cell process. The processing was undertaken by members of the group "Industrial solar cells" at ISFH and not by the author of this work.

4.3.2 Characterization and cell geometry

We list the characterization results in four groups: geometric, optical, resistance, and recombination. For the analysis of the uncertainty of the SEGA-simulation results we are interested in the variation of the determined values. The minimum and maximum

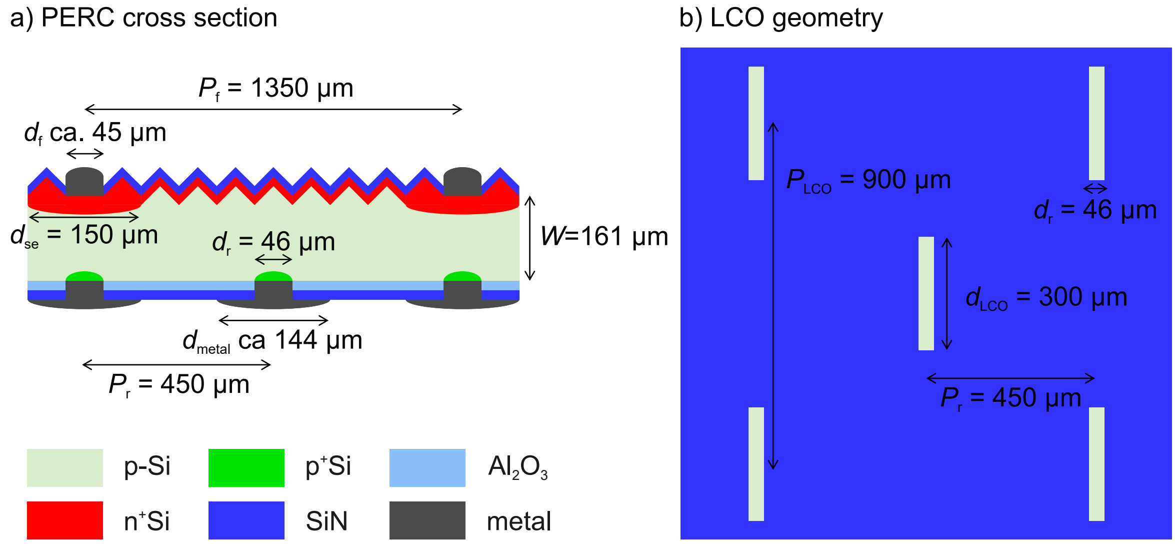

Figure 4.7: a) Cross section for the PERC+ cell analyzed in this section along with the values for the geometry definition. b) Schematic of the LCO dash geometry. The LCOs are shown in light green, the un-opened passivation in blue.

values along with the used measurement technique are given in Tab. 4.3.

Geometry

The cross-section of the cell and the LCO-geometry are shown in Fig. 4.7 a) and b), respectively. The thickness W is measured on the iV_{OC}-samples and determined to 161 μm. The contact pitches P_{f} and P_{r} are known from the screens used for printing and are 1350 μm and 450 μm for front and rear, respectively. The LCO-layout and selective emitter width d_{se} are known from the respective laser processes, which are very precise and only negligible variations occur. The front Ag fingers are smeared out and the small spots of silver next to the finger are only visible in overexposed images. This makes the definition of the width for the Ag-fingers d_{f} difficult and somewhat arbitrary. We choose to take the geometrical widths determined with the built-in microscope (not overexposed) of the TLM-Scan setup for measuring contact resistances. This assures that the specific contact resistances are determined with respect to the correct finger width in the TLM-Scan. We determine values between 27 μm and 42 μm for d_{f}.

Optics

Figure 4.8 shows the measured reflectance of two cells as green crosses and circles. Both curves show minimal deviation from each other, which also holds for the other measured cell reflectance spectra, which are not shown here. The green line shows the average of all

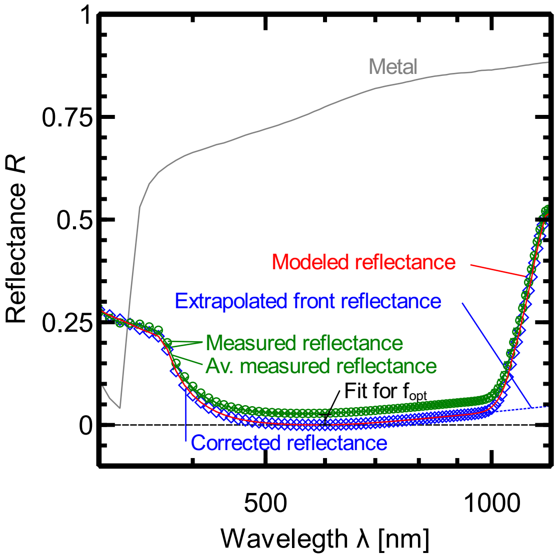

Figure 4.8: Measured reflectance of two cells (green crosses and circles) and average measured average reflectance (green line). The blue diamonds show the measured reflectance corrected for the reflectance of the metal fingers. The reflectance of the metal (Ag) is shown in gray. The red line shows the fit of the optical model presented in section 2.3. The blue dotted line shows the extrapolated front surface reflection.

measured reflectance spectra. The minimum of the measured reflectance is not zero as would be expected for a cell with ARC. The non-zero reflectance is caused by the metal fingers, which are in the analyzed area. From the offset between the minimal reflectance and zero and the separately measured reflectance of the metal, which is shown is gray, we determine an optical metallization fraction. This metallization fraction yields the optical width d_{opt} of the metal fingers, which can differ from the geometrical width d_{f} due to either light being reflected from the finger onto the active cell area or shading by small spots of silver paste, which are not visible in the optical microscope. The ratio of geometrical and optical width is described by an optical factor f_{opt} such that

$$d_{\mathrm{opt}} = f_{\mathrm{opt}} d_{\mathrm{geom}}. \tag{4.7}$$

We determine values between 1.167 and 1.841 for f_{opt}, which shows that a large fraction of light is reflected at small silver sports that are not visible in the microscope. The remaining optical parameters are determined by fitting the optical model described in section 2.3 on page 19 to the corrected reflectance, which is shown as blue diamonds. The extrapolated front surface reflectance $\mathcal{R}_{\mathrm{f}}$ is shown with a blue dotted line. The fitted model is shown with a red line and we see an excellent agreement between modeled and measured, corrected reflectance.

Resistance

The resistivity of the Si bulk ρ_b is determined by measuring the conductivity in the dark using the QSSPC setup and the fact that no other conducting layers are present in our lifetime samples. We determine values between 0.89 Ωcm and 0.96 Ωcm for ρ_b. The sheet resistances $R_\mathrm{sheet,e}$ and $R_\mathrm{sheet,e,sel}$ of the shallow and selective emitter, respectively, are determined using four-point probe measurements in the respective quarters of the $J_\mathrm{0,e}$-samples. In this measurement two outer probes inject a current into the sample and the voltage drop due to the sheet resistance of the sample is measured by two inner probes. We determine values between 70 Ω/□ and 74 Ω/□ for $R_\mathrm{sheet,e}$ and 114 Ω/□ and 118 Ω/□ for $R_\mathrm{sheet,e,sel}$. The contact resistances are determined with the TLM-approach described in section 2.2 on page 16 with the fully automatic TLM-Scan setup by pv-tools. For the rear Al contacts the method by Eidelloth and Brendel [39](see section 2.2) is applied. For the Al contacts we determine resistances between 1.33 mΩcm^2 and 1.34 mΩcm^2. For the front contacts we see a large variation in the determined resistances, which lie between 1.9 mΩcm^2 and 17.2 mΩcm^2. The finger line resistance $\rho_\mathrm{l,Ag}$ is determined by measuring the resistance between two busbars, which yields the parallel resistance of all fingers between the busbars. From this we calculate average $\rho_\mathrm{l,Ag}$ values for all cells, which lie between 1.38 Ω/cm and 1.64 Ω/cm.

Recombination

For finding the J_0-values of the rear-side passivation $J_\mathrm{0,pas}$ and the bulk lifetime parameters τ_n0 and τ_p0, we perform QSSPC measurements at five different positions on each of the respective lifetime samples. We determine $J_\mathrm{0,pas}$ using the Kane-Swanson analysis (section 2.4.4 on page 26) and find values between 0 fA/cm^2 and 2 fA/cm^2. For the bulk lifetime we correct the measured effective lifetime for the intrinsic lifetime using the parameterization by Richter *et al.* [27] and for the surface recombination using $J_\mathrm{0,pas}$ and equation 1.16. The resulting lifetime is that corresponding to the SRH defects in the bulk to which we fit with a mid-gap SRH defect represented by equation 1.11. We determine values between 103 μs and 253 μs for τ_n0 and 705 μs and 1114 μs for τ_p0. For the J_0-values $J_\mathrm{0,e}$ and $J_\mathrm{0,e,sel}$ of the shallow and selective emitter, respectively, we perform one QSSPC measurement in each of the respective quarters of the $J_\mathrm{0,e}$-samples and use the Kane-Swanson analysis to extract the J_0-values. We find values between 26 fA/cm^2 and 30 fA/cm^2 for $J_\mathrm{0,e}$ and values between 119 fA/cm^2 and 129 fA/cm^2 for $J_\mathrm{0,e,sel}$.

For the analysis of contact recombination we perform injection-dependent PC-PLI measurements of the respective samples. Figure 4.9 shows the lifetimes in the non-metallized and the three metallized areas for two out of four $J_\mathrm{0,Ag}$-samples (blue and red). The measured lifetimes are shown as crosses, asterisks, circles and squares for the non-metallized area and the metallized areas with metallization fractions of 2.7%, 4% and 8%, respectively. We fit the measured lifetimes using Quokka with the procedure described

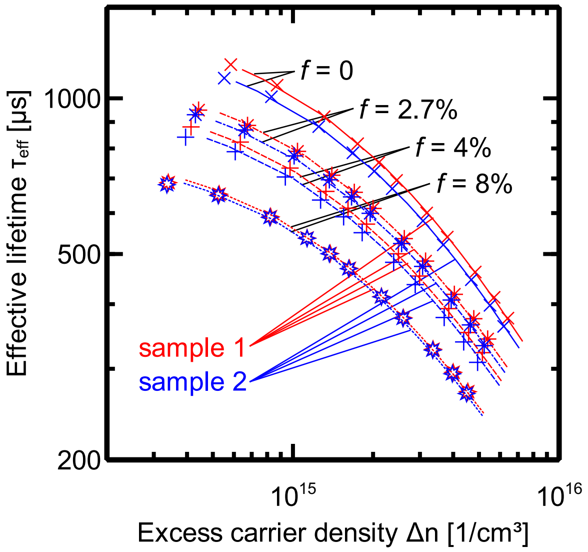

Figure 4.9: Lifetime curves for two out of four $J_{0,\mathrm{Ag}}$-samples (red and blue). The measured data are shown as crosses, asterisks, pluses and stars for metallization fractions of 0%, 2.7%, 4% and 8%. The simulated lifetime curves with the best overall $J_{0,\mathrm{Ag}}$- for the respective sample are shown as solid, dash, dash-dotted and dotted lines for the four areas of the sample.

in section 3.3.2 on page 44. For the fits we use J_0/k-model introduced in section 3.3.2 and find that $k = 2.5$ reproduces the injection dependency of the contact recombination well for all our $J_{0,\mathrm{Ag}}$-samples. For the first sample shown in red we find $J_{0,\mathrm{Ag}}$-values of 460 fA/cm^2, 440 fA/cm^{2}and 480 fA/cm^2 for the three metallized areas. The best fit for all three areas with one $J_{0,\mathrm{Ag}}$-value is achieved with 460 fA/cm^2. The simulated lifetime-curves for $J_{0,\mathrm{Ag}} = 460\,\mathrm{fA/cm^2}$ are shown in Fig. 4.9 as red solid, dashed, dash-dotted and dotted line for no metallization and the the three metallized areas, respectively. For this sample we see an excellent agreement of the three determined $J_{0,\mathrm{Ag}}$-values and consequently an excellent agreement between the measured and simulated lifetime curves. For the second sample shown in blue we use the same procedure and determine $J_{0,\mathrm{Ag}}$-values of 510 fA/cm^2, 570 fA/cm^2 and 510 fA/cm^2 for the respective fields. The best overall $J_{0,\mathrm{Ag}}$-value is 510 fA/cm^2 for which the simulated lifetimes are shown in Fig. 4.9. We see a good agreement with a slightly higher deviation between simulation and measurement for this sample, which is caused by inhomogeneities on the sample. We perform the same analysis also for the two remaining samples. Overall we find $J_{0,\mathrm{Ag}}$-values between 460 fA/cm^2 and 700 fA/cm^2 for the four samples. We apply the same approach to the rear Al contacts and find a value of $k = 1$ and $J_{0,\mathrm{Al}}$-values between 600 fA/cm^{2}and 700 fA/cm^2. It should be noted that $k = 1$ means that the rear Al contacts are well described with the unmodified J_0-model.

Table 4.3: Parameters of the PERC+ cell batch with minimum and maximum values and the respective measurement technique that was used for the determination.

Parameter	Minimum value	Maximum value	Meas. technique
d_f [μm]	27	42	opt. microscope
T_f	See Figure 4.8		Fitted to reflectance
$\mathcal{R}_\mathrm{b}$	0.924	0.927	Fitted to reflectance
Λ_b	0.882	0.892	Fitted to reflectance
f_opt	1.167	1.841	Fitted $\mathrm{R}_\mathrm{min} = 0$
ρ_b [Ωcm]	0.89	0.96	QSSPC
$R_\mathrm{sheet,e}$ [$\Omega/\square$]	114	118	4-point-probe
$R_\mathrm{sheet,e,sel}$ [$\Omega/\square$]	70	74	4-point-probe
$\rho_\mathrm{c,Al}$ [mΩcm^2]	1.33	1.34	TLM
$\rho_\mathrm{c,Ag}$ [mΩcm^2]	1.9	17.2	TLM
$\rho_\mathrm{l,Ag}$ [Ω/cm]	1.38	1.64	Busbar to busbar
τ_n0 [μs]	103	253	QSSPC
τ_p0 [μs]	705	1114	QSSPC
$J_\mathrm{0,pas}$ [fA/cm^2]	0	2	QSSPC
$J_\mathrm{0,e}$ [fA/cm^2]	26	30	QSSPC
$J_\mathrm{0,e,sel}$ [fA/cm^2]	119	129	QSSPC
$J_\mathrm{0,Ag}$ [fA/cm^2]	460	700	PC-PLI
k_Ag	2.5		PC-PLI
$J_\mathrm{0,Al}$ [fA/cm^2]	600	700	PC-PLI
k_Al	1		PC-PLI

4.3.3 Uncertainty analysis for the input parameters

The estimation of measurement uncertainties is a complex task, because all quantities, which contribute to the uncertainty have to be well-known. This includes statistical variations as well as systematic effects, the precision of the involved measurement equipment, the precision of used models and correlations between measured variables. Furthermore, some of these values are not available because they cannot be measured with justifiable effort. In addition, many of these uncertainties do not contribute significantly to the uncertainty of the final result, in this case the simulated solar cells conversion efficiency. A standard approach in the analysis of uncertainties is to first assume worst-case scenarios for all parameters and then analyze which of these parameters contribute significantly to the overall uncertainty. To identify the parameters that contribute significantly to the uncertainty of the simulated conversion efficiency U_sim, we perform a sensitivity analysis with Monte-Carlo device simulations using Quokka. For this Monte-Carlo sensitivity analysis we randomly choose the input parameters for the device simulations with a uniform probability distribution between the experimentally determined minimum and maximum values for each parameter. The values have been determined in the previous

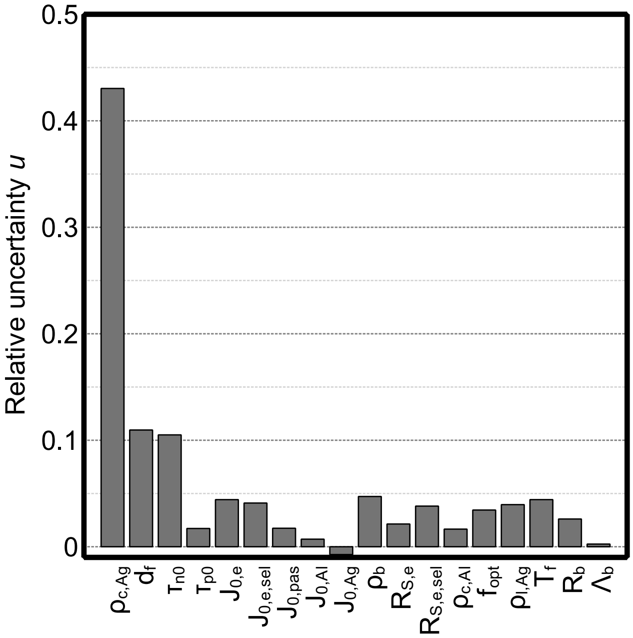

Figure 4.10: Sensitivity analysis of the uncertainty of the simulated efficiency. The gray bars show the relative uncertainty reduction for each parameter when the uncertainty of the respective parameter is set to zero.

section and are shown in Tab. 4.3. For the front-side transmission we randomly choose one of the measured transmission spectra with equal probabilities. We take the uniform distributions between minimum and maximum value as a worst-case scenario for the parameter distributions. This distribution is a worst-case assumption, because the values at the edges of the distribution (often outliers or extreme values) are chosen with the same probability as the values in the middle of the distribution.

We first calculate U_{sim} using all parameters with their respective uncertainties. We then calculate the relative uncertainty reduction u_x when the uncertainty of parameter x $(x = d_{\mathrm{f}}, \rho_{\mathrm{b}}, \tau_{\mathrm{n0}}, ...)$ is set to zero

$$u_x = \frac{U_{\mathrm{sim}} - U_{\mathrm{sim}}(U_x = 0)}{U_{\mathrm{sim}}}. \tag{4.8}$$

We use 500 device simulations in the Monte-Carlo analysis for U_{sim} and each u_x.

Figure 4.10 shows u_x for each parameter in Tab. 4.3, except for the k-values, which we did not vary. Small u_x mean that the uncertainty of the respective input parameter plays no significant role for U_{sim} of the analyzed PERC+ cell. All parameters except for the front contact resistance $\rho_{\mathrm{c,Ag}}$, the front finger width d_{f} and the minority carrier lifetime τ_{n0} contribute less than 5% to the overall uncertainty $(u_x < 0.05)$. Therefore, the worst-case assumptions for the uncertainties of these parameters are sufficiently precise

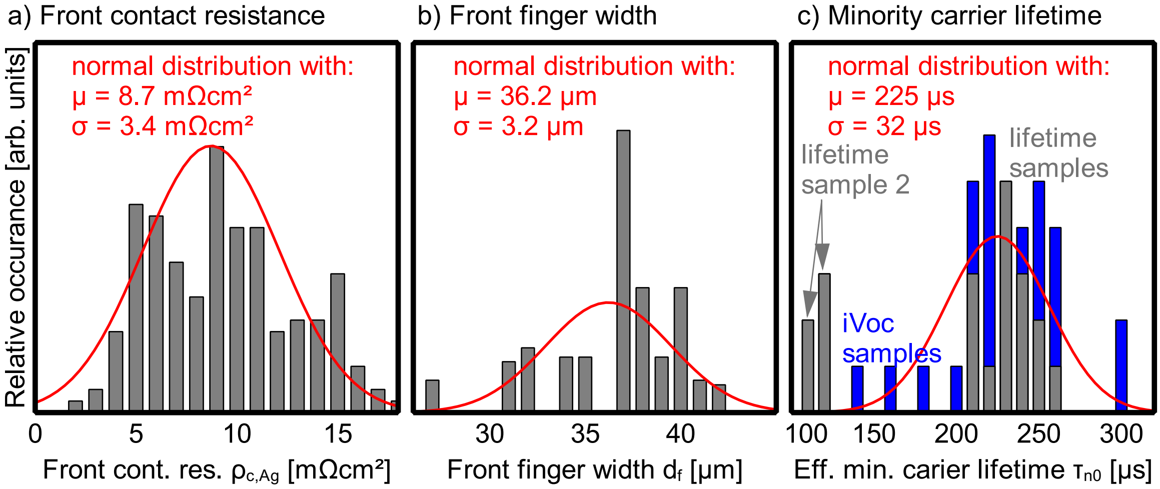

Figure 4.11: Distribution of the measured values for a) the front contact resistance, b) the front finger width and c) the minority carrier lifetime (gray) and the respective normal distributions fitted to the data (red). For the measurements of the minority carrier lifetime the blue bars show the measurement on the iV_{OC}-samples.

and we refrain from a further discussion of these parameters at this point.

We now take a closer look at the measurements for the parameters contributing significantly to U_{sim}. A complete uncertainty analysis for the measured parameters is beyond the scope of this work. However, the statistical variations between different samples and measurements are expected to exceed uncertainties due to, for example, instrument or model precision by far. Therefore, we take a look at the distribution of the measured values, which are shown in Fig. 4.11. For $\rho_{\mathrm{c,Ag}}$ (a) and d_{f} (b) we see that the measured values can be accurately described with a normal distribution shown in red. For $\rho_{\mathrm{c,Ag}}$ this distribution has a mean value of $\mu = 8.7\,\mathrm{m\Omega cm^2}$ and a standard deviation of $\sigma = 3.4\,\mathrm{m\Omega cm^2}$, which we take as the uncertainty for this parameter. Similarly, the normal distribution for d_{f} yields $\mu = 36.2\,\mu\mathrm{m}$ and $\sigma = 3.2\,\mu\mathrm{m}$. For the four measured lifetime samples (Fig. 4.11 c)) we see that three yield τ_{n0} in the range of 200-250 μs, while one sample ("lifetime sample 2") yields τ_{n0} of 100-120 μs. To analyze whether this deviation represents the width of the distribution or lifetime sample 2 is an outlier due to errors in processing or handling damage, we also include the iV_{OC}-samples in the analysis. In general the lifetime on iV_{OC}-samples is lower because more significant recombination channels exist, especially recombination within the P-diffusion. However, in low injection, where the τ_{n0} is dominating, the surface recombination has a lower impact than in high injection. Therefore, we can use the measurements on iV_{OC}-samples for the analysis of τ_{n0}, but the uncertainty of this measurement will be higher than the measurement on the lifetime samples. Here we see that all iV_{OC}-samples yield lifetimes of 150-300 μs with a mean value of about 220 μs, proving that lifetime sample

Table 4.4: Parameters and uncertainties for the PERC+ cell batch. For a uniform distribution the distribution width is the difference between max. and min. value. For a normal distribution the distribution width is the standard deviation.

Parameter	Value	Distribution	Distribution width
τ_{n0} [μs]	225	normal	32
τ_{p0} [μs]	910	uniform	410
J_0 rear surf. [fA/cm^2]	1	uniform	2
J_0 shallow em. [fA/cm^2]	28	uniform	4
J_0 sel. em. [fA/cm^2]	124	uniform	10
J_0 front cont. [fA/cm^2]	655	uniform	290
J_0 rear cont. [fA/cm^2]	850	uniform	200
ρ_{b} [Ωcm]	0.925	uniform	0.07
R_{sheet} shallow em. [$\Omega/\square$]	116	uniform	4
R_{sheet} sel. em. [$\Omega/\square$]	72	uniform	4
$\rho_{\mathrm{c,Ag}}$ [mΩcm^2]	8.7	normal	3.4
$\rho_{\mathrm{c,Al}}$ [mΩcm^2]	1.337	uniform	0.012
Av. finger res. [Ω/cm]	1.51	uniform	0.52
$\mathcal{R}_{\mathrm{b}}$	0.9253	uniform	0.0034
Λ_{b}	0.8867	uniform	0.0096
d_{f} [μm]	36.2	normal	3.2
f_{opt}	1.504	uniform	0.674

2 is indeed an outlier and will be eliminated from the further analysis. The remaining measurements can be accurately fitted with a normal distribution shown in red with $\mu = 225\,\mu$s and $\sigma = 32\,\mu$s, which we take as the uncertainty for τ_{n0}.

The final uncertainties, which we will use for the calculation of the SEGA uncertainty, are shown in Tab. 4.4

4.3.4 SEGA

With the uncertainties shown in Tab. 4.4 we now run a Monte-Carlo SEGA simulation with 160 SEGA simulations to determine the I-V parameters and potential efficiency gains with their respective uncertainties. We take the standard deviations of the simulated results as the uncertainty of the I-V-parameters and SEGA-gains.

The simulated I-V parameters are shown in Tab. 4.5 along with the measured I-V parameters and their respective uncertainties. A common way of comparing two values with uncertainties is by using the equality E_{n} of these values [67]. E_{n} is defined by

$$E_{\mathrm{n}} = \frac{x_{\mathrm{sim}} - x_{\mathrm{meas}}}{\sqrt{U_{\mathrm{sim}}^2 + U_{\mathrm{meas}}^2}}, \tag{4.9}$$

Table 4.5: Simulated and measured I-V parameters with their respective uncertainties and the E_n-values for the equality of the parameters.

	η	J_SC	V_OC	FF
Simulation	$21.5 \pm 0.2\%$	39.8 ± 0.3 mA/cm^2	675 ± 2 mV	$80.1 \pm 0.7\%$
Measurement	$20.4 \pm 0.4\%$	39.7 ± 0.2 mA/cm^2	674 ± 5 mV	$76.2 \pm 1.2\%$
E_n value	2.5	0.28	0.28	2.8

where x_sim and x_meas are the two values, in this case the simulated and measured I-V parameter, respectively and U_sim and U_meas are the respective uncertainties. Two values are considered equal within their uncertainties when

$$|E_\mathrm{n}| \leq 1. \tag{4.10}$$

The E_n-values for the I-V parameters are also shown in Tab. 4.5. We see an excellent agreement between simulation and measurement for J_SC and V_OC with E_n-values of 0.28 for both values. The FF, however, and consequently the efficiency, show E_n-values of 2.8 and 2.5, respectively, which shows the large deviations between simulation and measurement for these figures. In absolute terms the FF-deviation is about 4% while the uncertainties are only 0.7% and 1.2% for simulation and measurement, respectively.

To analyze the origin of the FF-deviation, we perform series resistance imaging of the cells using PL-imaging at low illumination densities at short-circuit and maximum power point conditions and at high illumination densities at open-circuit and short-circuit conditions. From these images we calculate an image of the series resistance using the approach by Trupke *et al.* [68]. Figure 4.12 shows the resulting image of the series resistance. The local stripes of high series resistance are caused by finger interruptions. These regions lead to a severe FF-loss, because they contribute significantly less current at the maximum power point of the cell. In addition, an inhomogeneous distribution of the contact resistance leads to areas with an increased series resistance, which show up in the image as lighter "cloudy" areas. The inhomogeneity of the series resistance is, however, not considered in the unit cell simulation that we perform. The Quokka simulation employs average values for the contact and grid resistances. To analyze whether this inhomogeneous series resistance explains the discrepancy between unit cell simulation and measurement, we employ a local impact analysis (LIA) [69] in which the solar cell is locally described with two-diode models for each pixel. We extract all parameters required for the two-diode model from a fit to the measured I-V-curve except for the series resistance for which we import the spatially resolved series resistance image shown in Fig. 4.12. The LIA calculation yields a FF of 76.32%, which agrees well with the measured FF of 76.67% for this cell. When we take a homogeneous series resistance of 0.673 Ωcm^2, as extracted from the Quokka simulation, we get a FF of 79.34%. Consequently, the inhomogeneous series resistance leads to a FF-loss of approximately 3%. Adding these 3% to the average measured FF in Tab. 4.5 yields

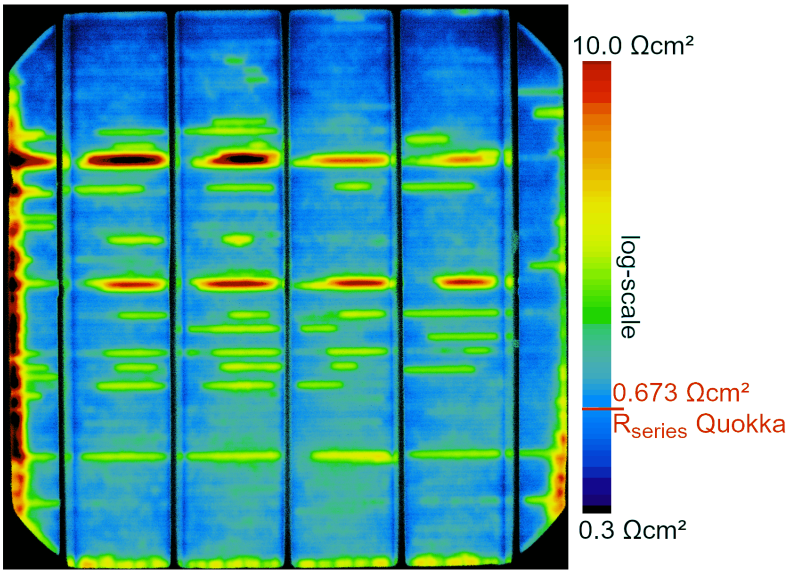

Figure 4.12: Series resistance image of one solar cell from the analyzed PERC+ cell batch. Blue regions correspond to a low series resistance. The scale shows the absolute value of the series resistance in log-scale. Marked on the scale is the series resistance extracted from the Quokka simulation.

$79.2 \pm 1.2\%$ and the comparison to the simulated FF yields an E_n-value of 0.64. The corresponding efficiency loss is 0.7%, which yields an E_n-value of 0.89 for the measured efficiency corrected for the inhomogeneous series resistance compared to the simulated efficiency.

Consequently, the Quokka unit cell simulation is well suited to analyze the remaining efficiency gains with a SEGA. The resulting efficiency gains and their respective uncertainties are shown in Fig. 4.13. The largest individual losses are front finger shading (0.9%), bulk recombination (0.52%) and the front contact resistance (0.5%). In addition, the synergistic effects between different recombination channels pose a large loss of 2.56%. The uncertainties in the input parameters translate to the SEGA results with an uncertainty of 0.2% for shading and the front contact resistance and 0.07% for the bulk recombination. Here we see that eliminating the outlier from the lifetime sample measurements reduced the uncertainty of the bulk recombination in comparison to the finger width and the front contact resistance. The remaining losses are determined with an uncertainty of 0.05% for the synergistic effects between the recombination channels and between the different groups, 0.04% for the 0.27% gain due to front contact recombination and less than 0.03% for all remaining gains. All gains combined with the 21.5% reference efficiency lead to an efficiency of 28.9%, which is the efficiency limit for 161 μm thickness and a base resistivity of 0.9 Ωcm.

The logical next steps for improving the cell are to work on reliable screen printing to reduce the impact of the inhomogeneity of the series resistance, shading and contact

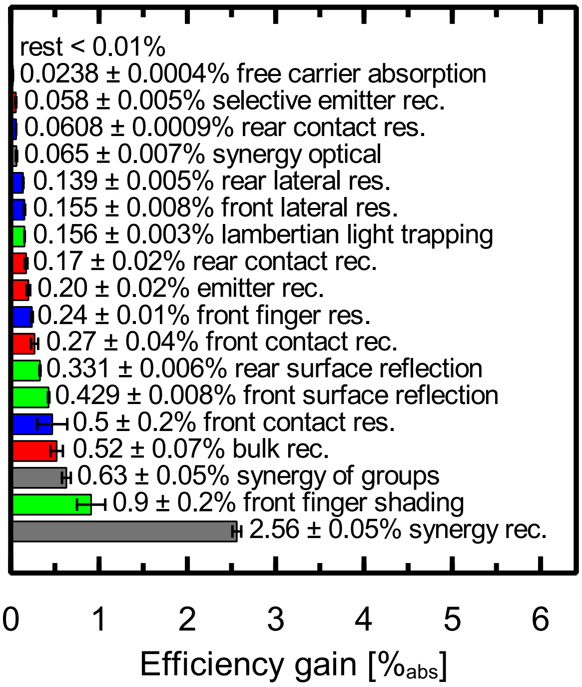

Figure 4.13: SEGA for the PERC+ cell batch analyzed in this section with the uncertainties for each loss shown as error bars. The red bars show recombination losses, the green bars optical and the blue bars resistive losses. The gray bars show synergistic losses between the different loss channels.

resistivity. These improvements promise a total efficiency gain of up to 2.1%, although it should be noted that, at least for contact shading, the full gain cannot be realized, because some shading is unavoidable in PERC cells. A further improvement step concerns the wafer material and processing. The low minority carrier lifetime, most likely caused by contamination of the wafer, promises a gain of up to 0.52% efficiency. This gain can, with good quality Si and clean process steps, be almost completely avoided as B-doped Cz-Si can reach minority carrier lifetimes of about a factor of 10 higher than measured in our characterization as discussed in the next chapter.

The large recombination losses due to synergistic effects between the different recombination channels represent another big lever in terms of higher cell efficiencies. The optimization of conventional contacts and diffusions is, however, limited and PERC cell efficiencies are expected to saturate at around 24% [70] with diffused contacts. Therefore, we discuss the implementation of passivating contacts into industrial solar cell in the next chapter.

5 Integration of poly-Si junctions into industrial solar cells

Research [70] suggests that the maximum efficiency for PERC+ is about 24%, mainly due the recombination at conventional diffusions and contacts. Next-generation solar cells, therefore, aim at higher efficiencies by the use of passivating contacts.

One of the approaches for passivating contacts are poly-silicon on oxide (POLO) junctions. Applying doped poly-crystalline silicon (poly-Si) to a crystalline silicon wafer with a thin oxide in between yields low surface recombination and, for contacted poly-Si, low contact resistivities. These POLO junctions are, therefore, a promising improvement over conventionally diffused junctions in terms of higher cell efficiencies. Concepts featuring POLO contacts or similar approaches have already achieved high efficiencies in lab-scale production [9, 71, 72] and pilot line production [73]. However, POLO contacts have not yet found their way into mass production. One of the reasons is the increased process complexity for many of the cell concepts featuring POLO contacts. The other reason may be the uncertainty in the expected cell efficiency. Therefore, we analyze different concepts for POLO implementation into new and existing production lines in this chapter. Parts of the content in this chapter are submitted for publication [Kruse2020].

5.1 Simulation parameter selection & optics

We aim at comparing different cell structures for their potential. Two major aspects have to be considered when evaluating new cell concepts for their potential economic benefit in large-scale production: The process complexity and the efficiency gain compared to proven concepts. To estimate the potential efficiency of each concept, we perform Quokka simulations. We choose equal input parameters for equal or comparable properties of the respective structures. For example, the recombination at a 200 nm-thick n-doped poly-Si junction (n-POLO) is always assumed to be $J_0 = 3\,\mathrm{fA/cm^2}$ although in reality this J_0 can vary for different cell structures due to the influence of other process steps on its passivation quality. We do this to allow for a fair comparison of the various cell types. In general, we choose state-of-the-art parameters achieved in research laboratories with industrial-type processes. We confine the analysis to screen-printed contacts.

For the optical performance of each structure we employ ray-tracing simulations using SUNRAYS (see section 2.3.2 on page 21). We simulate all unit-cells shown in Fig. 5.1 for the example of the p-Si n-POLO FJ structure introduced below. At the top the

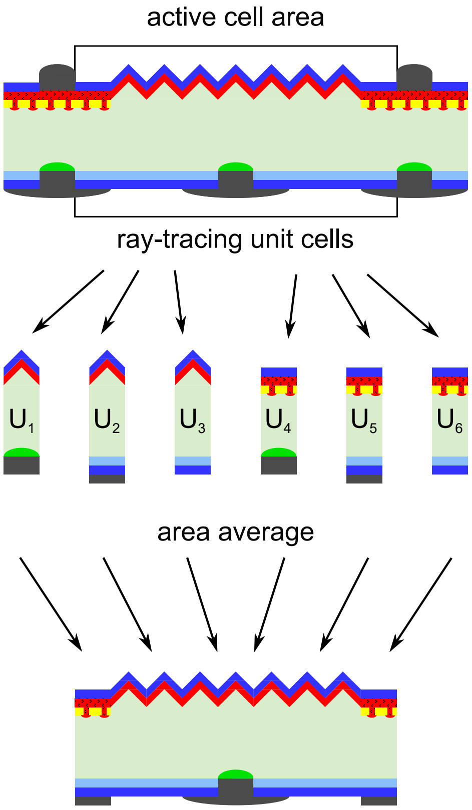

Figure 5.1: Cell regions that are separately modeled by ray-tracing for the determination of a generation profile. From top to bottom: Full cell structure with active cell area marked. The six unit cells required for the optical simulation of the example structure. Area averaging yielding the generation profile for the complete active cell area.

cell schematic is shown with the active cell area marked, that is the area between the contacts. Underneath the metal we assume that there is no generation. The active cell area is divided into separate unit cells for ray-tracing: In this example we have two different front surfaces, namely a SiN ARC on P-diffused and textured Si and planar poly-Si with SiN ARC. At the rear we have three different surfaces, namely the areas contacted with an Al-BSF and the areas with planar Al_2O_3/SiN passivation covered with metal and without metal. Two front and three rear surfaces yield the six unit cells $U_1 - U_6$ shown in the second row of Fig. 5.1. After the ray-tracing has been completed for all unit cells the results are averaged according to their area fractions. The resulting generation profile is, therefore:

$$g = f_{\text{text}}(f_{\text{BSF}}g_1 + f_{\text{metal}}g_2 + f_{\text{pas}}g_3) + f_{\text{POLO}}(f_{\text{BSF}}g_4 + f_{\text{metal}}g_5 + f_{\text{pas}}g_6) \tag{5.1}$$

where $f_{\text{text}}, f_{\text{POLO}}, f_{\text{BSF}}, f_{\text{metal}}$ and f_{pas} are the area fractions for the textured front surface, the front-side POLO, the rear contacted area, the rear passivation covered with metal and without metal, respectively ($f_{\text{text}} + f_{\text{POLO}} = 1$ and $f_{\text{BSF}} + f_{\text{metal}} + f_{\text{pas}} = 1$). g_1 through g_6 are the generation profiles determined by ray-tracing for the six respective unit cells. It should be noted that we simulate an external mirror with unity specular reflectance on the rear side to represent a reflecting measuring chuck or a white module back-sheet. The effect of this external mirror on the simulated efficiency is similar for all simulated structures, because all structures feature a textured front- and planar rear-side. If any structure had, for example, a textured rear side, the rear-side transmittance would increase and thus the impact of an external mirror would be larger for this structure.

5.2 Simulated cell structures

We consider ten different cell concepts featuring POLO contacts along with a PERC+ and a TOPCon [10] reference cell.

The two references serve to put the absolute simulated efficiencies in this work into the context of cell structures commonly studied by other research teams. The PERC+ cell also represents state-of-the-art industrial solar cells. The ten POLO cell structures feature either one POLO and one conventional contact or two POLO contacts either in front junction (FJ), back junction (BJ) or interdigitated back contact (IBC) configuration. These cell types address the main bottlenecks of the PERC+ structure discussed in section 4.3.4 on page 68. The first part of the notation that we use for the cell types describes the wafer type (n-Si or p-Si). The next part of the name describes whether one or both polarities are contacted with POLO (POLO or POLO^2). In case of the POLO concepts a n or p describes the polarity of the POLO layer (n-POLO or p-POLO). The last part of the notation describes whether the concept is a FJ, BJ or IBC cell concept.

Figure 5.2 shows the ten cell structures to be analyzed: a) the reference PERC+ cell, b) the reference TOPCon cell based on n-type Si with a diffused boron emitter and a full area n-POLO junction on the rear, c) the p-Si p-POLO FJ concept with a PERC+ front side and a full area p-POLO junction at the rear side, d) the p-Si n-POLO FJ structure, which is a PERC+ cell but with n-POLO under the front contacts, e) the p-Si n-POLO BJ structure, which features Al contacts on the front and a full area n-POLO on the rear side, f) the p-Si n-POLO IBC structure, which is an IBC concept featuring Al-BSF and n-POLO contacts, g) the p-Si POLO^2 BJ, which features local p-POLO contacts on the front side together with a boron-doped front surface field (FSF) and a full area n-POLO junction on the rear, h) the same p-Si POLO^2 BJ structure as in (g) but without FSF, i) p-Si POLO^2 IBC, which is an IBC concept with POLO contacts for both polarities and j-l) the same structures as (g-i) but with reversed polarities, therefore based on n-type Si.

Please note that for all cell types the structured layers underneath the contacts (selective emitter or POLO) are either wider than the metal contact or the metal is wider than the LCO in case of Al contacts. This accounts for alignment tolerances of the screen-printing metallization that we consider in our study. The Ag contacts for which we assume a printing width of 30 μm are printed on 75 μm-wide stripes of either POLO layers or the selective emitter. For the Al contacts we take an LCO width of 13 μm and 50 μm Al fingers. For the IBC cells we assume an emitter coverage of 80%. For all cell types we optimize the front contact pitches individually using the parameter variation ability of the SEGA-GUI (see section 4.2 on page 57). The optimized contact pitches are given in section 5.4. For the rear side, smaller contact pitches are in most cases preferable over larger pitches due to reduced resistance contributions. We, therefore, choose a rear contact pitch of 0.5 mm for all cell types.

5.3 Electronic input parameters

We choose, if available, state-of-the-art (i.e. best-measured) parameters measured at ISFH achieved with processes that can, at least in principle, be transferred to industrial-scale production, because for our in-house measurements we can evaluate whether the process is compatible with industrial process sequences.

For the recombination at a planar surface passivated with Al_2O_3/SiN and at the front contacts we take the values determined in section 4.3.3 with $J_0 = 1\,\mathrm{fA/cm^2}$ and $J_0 = 660\ \mathrm{fA/cm^2}$ and $k = 2.5$, respectively, as these values represent state-of-the-art solar cell production. The remaining parameters were all measured at ISFH on test structures similar to those shown in section 4.3 and with the characterization methods presented in chapters 2 and 3. For the boron diffusions we take values from the literature (References with the respective values below).

For the B-doped Cz-Si wafer material we measure $\rho_\mathrm{b} = 0.9\ \Omega\mathrm{cm}$ and mid-gap SRH lifetime parameters $\tau_\mathrm{n0} = 2000\ \mu\mathrm{s}$ and $\tau_\mathrm{p0} = 20000\ \mu\mathrm{s}$. These values are about one order of magnitude higher than the values determined in section 4.3.3 due to a greatly reduced impurity concentration. For the phosphorus-doped Cz-Si material we measure an injection independent SRH lifetime of $\tau_\mathrm{bulk} = 22000\ \mu\mathrm{s}$ with $\rho_\mathrm{b} = 3\ \Omega\mathrm{cm}$. The surface passivation quality of an Al_2O_3/SiN stack depends on the surface topology. For the textured surfaces passivated with an Al_2O_3/SiN stack we determine a J_0-value of 3 fA/cm^2 on p-type material. For n-type material we assume a passivation quality equal to that on p-type.

For the phosphorus-diffused surfaces we determine $J_0 = 22\ \mathrm{fA/cm^2}$ and $R_\mathrm{sheet} = 133\ \Omega/\square$ for the inter-finger region as published in Ref. 74. For the selective doping underneath the front contacts we determine $J_0 = 100\ \mathrm{fA/cm^2}$ and $R_\mathrm{sheet} = 95\ \Omega/\square$. Both values represent a reduction of about 20% compared to the values determined

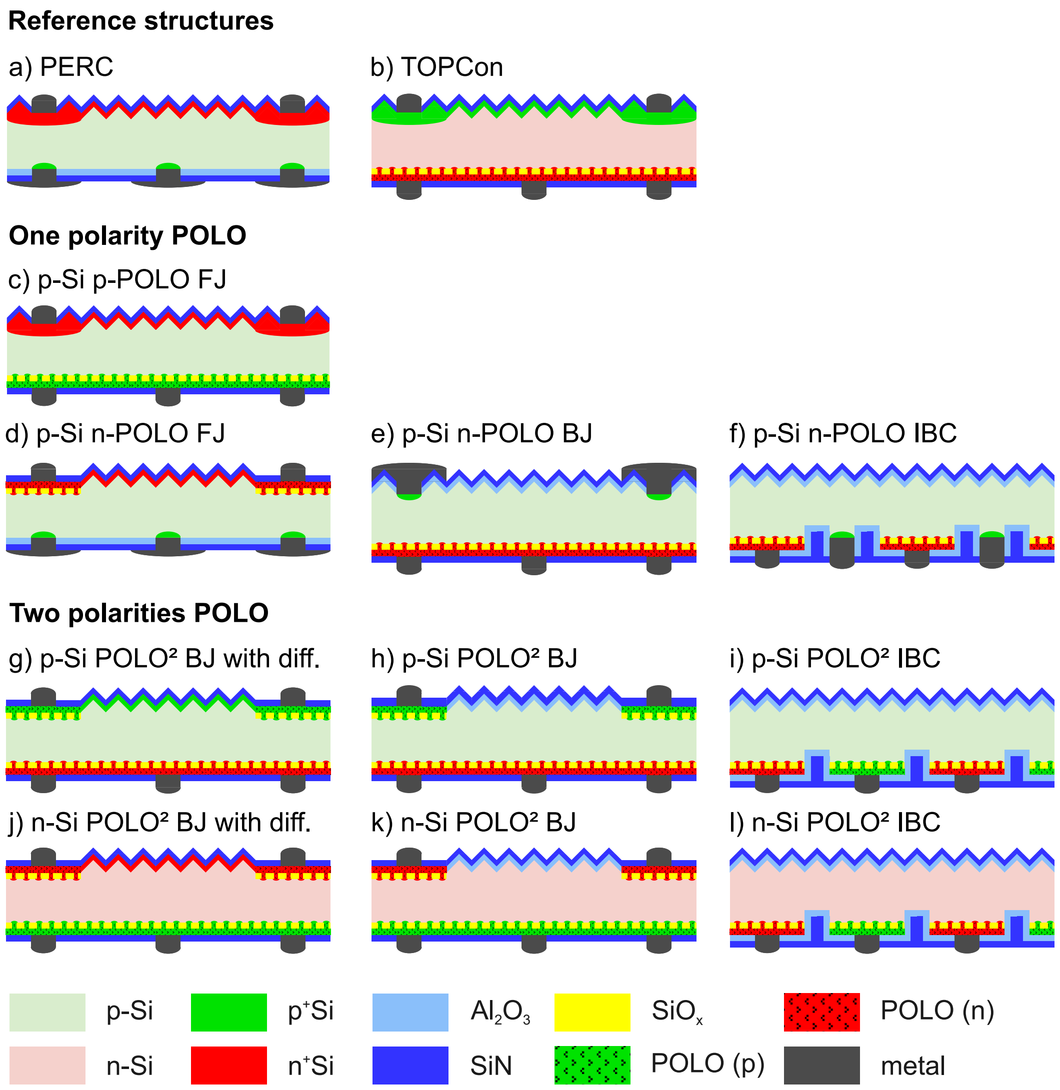

Figure 5.2: Cell structures discussed in this study. Top row: reference structures with a) the PERC+ cell and b) the TOPCon structure. 2nd row: c) concept featuring one polarity p-POLO in FJ configuration with a conventional emitter. 3rd row: concepts featuring n-POLO and conventional Al contacts in d) FJ configuration, e) BJ configuration and f) IBC configuration. 4th row: concepts featuring POLO junctions for both polarities based on p-Si g) in BJ configuration with a conventional B-diffusion, h) in BJ configuration without diffusion and i) in IBC configuration. 5th row: concepts featuring POLO junctions for both polarities based on n-Si j) in BJ configuration with a conventional P-diffusion, k) in BJ configuration without diffusion and l) in IBC configuration.

Table 5.1: Electronic input parameters for the device simulations presented in this chapter

Parameter	Recombination	Resistive
p-type (B) bulk	$\tau_{\mathrm{n0}} = 2000\ \mu$s $\tau_{\mathrm{p0}} = 20000\ \mu$s	$\rho_{\mathrm{b}} = 0.9\ \Omega$cm
n-type (P) bulk	$\tau_{\mathrm{bulk}} = 22000\ \mu$s	$\rho_{\mathrm{b}} = 3\ \Omega$cm
Pas. on p-Si (plan.)	$J_0 = 1\,\mathrm{fA/cm^2}$	n.a.
Pas. on p-Si (text.)	$J_0 = 3\,\mathrm{fA/cm^2}$	n.a.
Pas. on n-Si	$J_0 = 3\ \mathrm{fA/cm^2}$	n.a.
emitter P-diff.	$J_0 = 22\ \mathrm{fA/cm^2}$[74]	$R_{\mathrm{sheet}} = 133\ \Omega/\square$[74]
FSF P-diff.	$J_0 = 15\ \mathrm{fA/cm^2}$	$R_{\mathrm{sheet}} = 150\ \Omega/\square$
selective P-diff.	$J_0 = 100\ \mathrm{fA/cm^2}$	$R_{\mathrm{sheet}} = 95\ \Omega/\square$
emitter B-diff.	$J_0 = 14\ \mathrm{fA/cm^2}$ [75]	$R_{\mathrm{sheet}} = 135\ \Omega/\square$[75]
FSF B-diff.	$J_0 = 8\ \mathrm{fA/cm^2}$	$R_{\mathrm{sheet}} = 180\ \Omega/\square$
selective B-diff.	$J_0 = 110\ \mathrm{fA/cm^2}$ [76]	$R_{\mathrm{sheet}} = 95\ \Omega/\square$[76]
n-type POLO	$J_0 = 3\ \mathrm{fA/cm^2}$ [77]	$R_{\mathrm{sheet}} = 50\ \Omega/\square$
p-type POLO	$J_0 = 5\ \mathrm{fA/cm^2}$	$R_{\mathrm{sheet}} = 200\ \Omega/\square$
Ag on P cont.	$J_0 = 655\ \mathrm{fA/cm^2}$, k = 2.5	$\rho_{\mathrm{c}} = 1.5\ \mathrm{m\Omega cm^2}$
Al on Si cont.	$J_0 = 400\ \mathrm{fA/cm^2}$	$\rho_{\mathrm{c}} = 1.3\ \mathrm{m\Omega cm^2}$
Ag on B cont.	$J_0 = 740\ \mathrm{fA/cm^2}$ [78]	$\rho_{\mathrm{c}} = 2\ \mathrm{m\Omega cm^2}$ [79]
Ag on n-POLO cont.	Same as n-POLO	$\rho_{\mathrm{c}} = 0.9\ \mathrm{m\Omega cm^2}$
Ag on p-POLO cont.	Same as p-POLO [80]	$\rho_{\mathrm{c}} = 5\ \mathrm{m\Omega cm^2}$

in section 4.3.3, which shows that the emitter diffusion of the PERC+ batch analyzed in chapter 4 was reasonably good when compared to state-of-the-art parameters. As shown in Fig. 5.2 (g) the p-Si POLO^2 BJ can be processed with a FSF. Because this FSF does not need to provide the same lateral conductivity as an emitter diffusion we take parameters representing a weaker diffusion with $J_0 = 15\ \mathrm{fA/cm^2}$ and $R_{\mathrm{sheet}} = 150\ \Omega/\square$. For the boron emitter in the TOPCon concept we take literature values for the shallow doped emitter [75] with $J_0 = 14\ \mathrm{fA/cm^2}$ and $R_{\mathrm{sheet}} = 135\ \Omega/\square$ and the selective emitter [76] with with $J_0 = 110\ \mathrm{fA/cm^2}$ and $R_{\mathrm{sheet}} = 95\ \Omega/\square$. For the boron FSF required for structure j) we again take values representing a weaker diffusion with $J_0 = 8\ \mathrm{fA/cm^2}$ and $R_{\mathrm{sheet}} = 180\ \Omega/\square$.

For n- and p-POLO junctions we confine the analysis to planar POLO layers and assume 200 nm thickness for the calculation of the optical performance. We assume this thickness to be sufficient for a screen-printed POLO contact to retain its recombination properties. For planar n-POLO layers we measure a J_0 of 3 $\mathrm{fA/cm^2}$ and a sheet resistance of 50 $\Omega/\square$ as published in Ref. 77. For p-POLO layers we measure a J_0-value of 5 $\mathrm{fA/cm^2}$ and a sheet resistance of 200 $\Omega/\square$.

In contrast to the high contact resistivity measured in section 4.3.3, we measure low contact resistivity of $\rho_c = 1.5\ \text{m}\Omega\text{cm}^2$ for the state-of-the-art Ag on P contacts. For the Al-BSF contacts we determine $J_0 = 400\ \text{fA/cm}^2$ and $\rho_c = 1.3\ \text{m}\Omega\text{cm}^2$. While the recombination at Al-BSF contacts is about 50% smaller in state-of-the-art cells compared to the cell batch from chapter 4 the contact resistivity is approximately the same. For the Ag contact on B-diffusion we again refer to the literature with a $J_0 = 740\ \text{fA/cm}^2$ [78] and a $\rho_c = 2\ \text{m}\Omega\text{cm}^2$ [79]. For n-POLO contacts formed with firing-through pastes we see that the contacts do not show an increased recombination compared to the POLO layer. These contacts were measured with a resistivity of $\rho_c = 0.9\ \text{m}\Omega\text{cm}^2$. For p-POLO the firing-through pastes yield a high J_0 of around $250\ \text{fA/cm}^2$ as published by Mack *et al.* [81]. However, non-firing-through pastes lead to an insignificant recombination increase similar to n-POLO contacts with a resistivity of $\rho_c = 5\ \text{m}\Omega\text{cm}^2$ as measured at ISFH [9, 80].

5.4 Results and discussion

Table 5.2 lists the simulated parameters of the I-V-curve for each of the cell types shown in Fig. 5.2. The results show clear trends in terms of V_{OC} and J_{SC}: V_{OC} increases with the reduction of recombination losses at the conventional contacts and diffusions. Consequently, the POLO^2 concepts show the highest V_{OC} followed by the POLO concepts. However, POLO layers always lead to parasitic optical absorption. Therefore, concepts featuring structured POLO at the front show lower J_{SC} than those without. In addition, POLO layers on the rear also contribute to the parasitic absorption, leading to further J_{SC} reduction for concepts featuring full area rear POLO.

For the discussion whether a cell concept is a promising candidate for industrial production, the process complexity has to be evaluated along with the efficiency gain over today's PERC+ cells. However, here we analyze hypothetical cell structures, which have not been fabricated yet. Therefore, we can only discuss the main steps of potential cell processes along with a SEGA. The processes steps that we discuss are not specific in terms of deposition techniques, etching solution, protection layers and so on and are not the only option for manufacturing the respective cells. The hypothetical cell processes only serve to judge the process complexity qualitatively in comparison to PERC+.

The detailed results for each of the cell concepts will now be discussed: Our reference **PERC+** cell shows an efficiency of 23.8% and the industrial-type production sequence is shown on the left side of Fig. 5.3. First the wafer is prepared by cleaning and texture etching and after that both surfaces are doped with phosphorus. The front-side laser-doping for the designated contact areas is performed and in a next step the rear emitter removed. In the next steps the SiN and Al_2O_3/SiN passivation for the front- and rear-side, respectively, are applied. The remaining steps serve the contacting of the solar cell: laser contact openings on the rear side, Al and Ag print for the front- and rear-side, respectively and co-firing of both contacts. The optimized front contact pitch is 1.6 mm. The SEGA for the PERC+ cell is shown on the right side of Fig. 5.3. The main

Table 5.2: Simulated *I-V* parameters for the cell structures shown in Fig. 5.2

Cell type	η [%]	J_{SC} $\left[\frac{mA}{cm^2}\right]$	V_{OC} [mV]	FF [%]
PERC+	23.8	41.3	697	82.5
TOPCon	24.4	41.2	712	83.1
p-Si p-POLO FJ	23.8	41.2	700	82.5
p-Si n-POLO FJ	24.1	40.9	712	82.8
p-Si n-POLO BJ	24.7	40.6	736	82.7
p-Si n-POLO IBC	25.5	41.7	733	83.4
p-Si POLO^2 BJ with diff	24.6	40.6	734	82.7
p-Si POLO^2 BJ	25.0	40.6	742	83.0
p-Si POLO^2 IBC	25.9	41.7	742	83.5
n-Si POLO^2 BJ with diff.	24.5	40.9	722	83.0
n-Si POLO^2 BJ	25.1	40.9	737	83.3
n-Si POLO^2 IBC	25.8	41.9	738	83.3

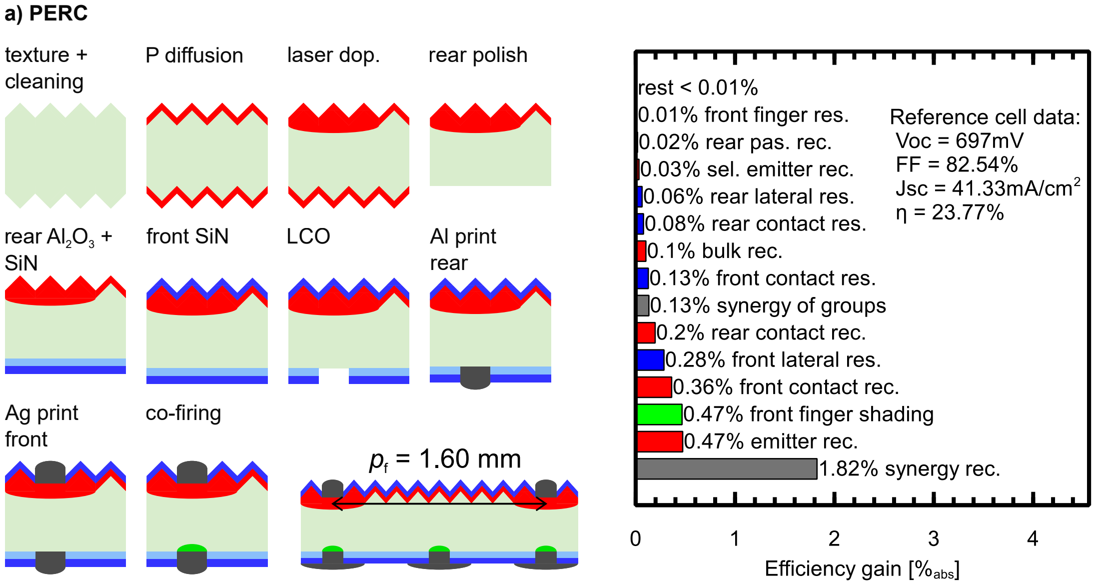

Figure 5.3: Main process steps and SEGA analyses for the reference PERC+ structure.

losses are the recombination within the emitter and at the front contacts. The front contacts are also responsible for the shading, which cause an efficiency loss equal to that due to emitter recombination. In addition, the PERC+ cell shows large synergistic recombination losses of 1.8%. The SEGA shows that the front surface, especially the contacts, poses a large potential efficiency gain when optimized. However, even the largest individual loss is below 0.5%, which makes the economic feasibility of any concept addressing only one of the losses questionable.

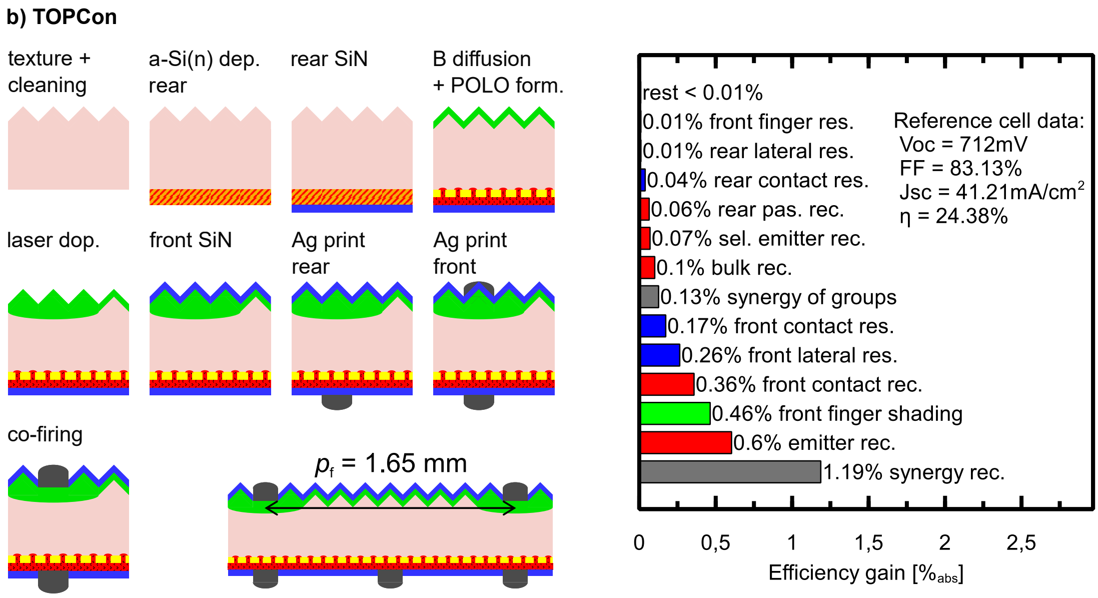

Figure 5.4: Main process steps and SEGA analyses for the reference TOPCon structure.

The main process steps for the **TOPCon** cell along with the respective SEGA are shown in Fig. 5.4. The process requires a full area a-Si(n) deposition on the rear with a protective SiN and a boron diffusion including laser-doping of the designated contact areas for the front side. The optimized front contact pitch is 1.65 mm. The TOPCon concept yields an efficiency of 24.4% (+0.6% in comparison to PERC+) in our simulation. The *n*-type material and the rear POLO junction reduce the bulk and rear contact recombination present in the PERC+ cell. Therefore, although the boron emitter and contacts show smaller recombination than the phosphorus counterparts in PERC+, the emitter recombination loss is even larger than in PERC+ with 0.6%. However, the synergistic recombination losses are greatly reduced by over 0.6%. Therefore, the V_{OC} is increased by 15 mV compared to PERC+ while the J_{SC} is approximately the same. The FF is also higher in the TOPCon structure compared to PERC+ due to the higher lifetime and reduced resistances at the rear side (lateral and contacts).

The process steps and SEGA for the **p-Si p-POLO FJ** structure are shown in Fig. 5.5. The process flow is similar to PERC+ except an a-Si(p) layer and SiN is deposited prior to the phosphorus diffusion. After printing Ag contacts for both front and rear the contact firing also forms the rear POLO layer. The optimized front contact pitch is 1.65 mm. Although the complexity of this process is comparable to that of PERC+ the efficiency is not higher either. The slight increase in V_{OC} (3 mV) is compensated by the loss in J_{SC} (0.1 mA/cm^2). The 0.2% gain simulated for avoiding the rear contact recombination in the PERC+ cell is, therefore, entirely compensated by the slightly increased recombination at the p-POLO layer compared to the Al_2O_3 passivation and

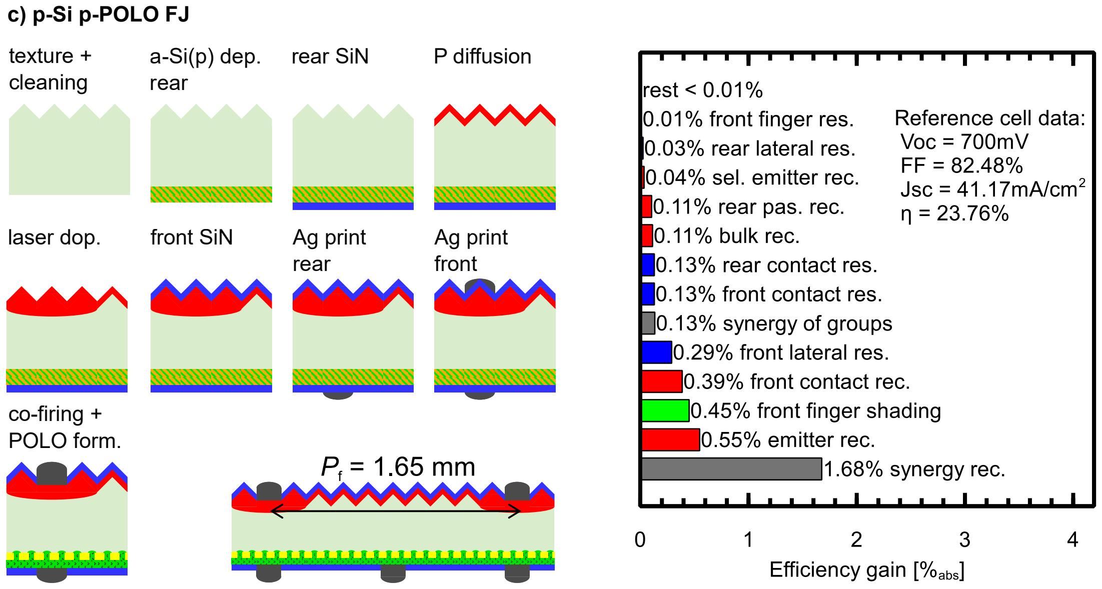

Figure 5.5: Main process steps and SEGA analyses for the p-Si p-POLO FJ structure.

the increased optical absorption. The p-Si p-POLO FJ concept is, therefore, not a promising option for industrial integration of POLO junctions.

In the analysis of the **p-Si n-POLO FJ** concept we see that replacing the selective emitter of the PERC+ concept with a local n-POLO layer yields an efficiency gain of 0.3% by yielding a higher open-circuit voltage (+ 15 mV) and fill factor (+0.3%) due to the reduced recombination and contact resistance thereby overcompensating the loss in the short-circuit current due to absorption and reflection at the POLO layer. It should be noted that the optimal front contact pitch is, with 1.3 mm, 0.3 mm smaller than for the PERC+ cell. This smaller pitch is a result of balancing the losses due to shading with the gains due to a reduced lateral resistance and recombination when using a smaller contact pitch. The increase in shading losses can be seen in the SEGA with 0.59% compared to 0.47% in PERC+ (see Fig. 5.3). The hypothetical industrial type production sequence is shown on the left in Fig. 5.6. The process is very similar to the PERC+ reference process except for the laser-doping of the selective emitter. This step is replaced with a full area a-Si deposition, which is subsequently structured prior to the phosphorus diffusion. While this may sound easy to implement, this structured a-Si deposition, is not a standard industrial process. It can, for example, be achieved using laser oxidation [82] or shadow masks [83] for a structured deposition. This challenging deposition step may render this cell concept uneconomic given the simulated efficiency gain is only 0.3%. However, ongoing research in structured a-Si deposition may lead to industrially feasible processes for this cell concept. We see, however, that the potential efficiency gain due to emitter recombination is 0.8%. This poses a a big lever in terms

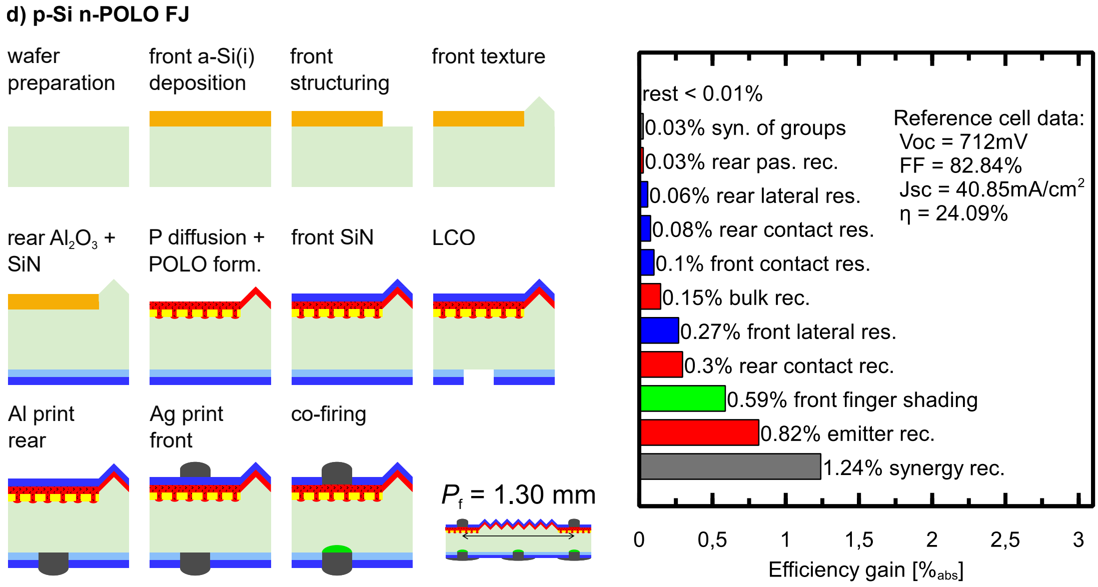

Figure 5.6: Main process steps and SEGA analyses for the p-Si n-POLO FJ structure.

of larger cell efficiencies and brings us to the following cell concepts, the p-Si n-POLO BJ and IBC concept.

The **p-Si n-POLO BJ** yields an efficiency 0.9% higher than the reference PERC+ process. The large shading losses of 0.71%, as show in the SEGA in Fig. 5.7, due to the 50 μm Al fingers are overcompensated by the large gain in the open-circuit voltage (39 mV), which rises from the avoided recombination at the conventional P-diffusion and Ag on P contacts. The greatly reduced recombination shows up in the SEGA by a small synergistic recombination gain of 0.47%. The largest individual recombination losses are now recombination within the bulk and at the textured front surface followed by recombination at the Al contact. The fact that these gains where negligible in the PERC+ SEGA shows the strength of the SEGA, because the p-Si n-POLO BJ yields a much higher efficiency than PERC+ due to reduced synergistic effects between the recombination channels. The main losses for this cell are the shading by the 50 μm wide Al contacts and the front lateral resistance due to the large optimum contact pitch of 1.8 mm. This cell concept can hypothetically be manufactured with a very lean process flow as shown in Fig. 5.7. After wafer preparation, which includes cleaning, texture and rear-side polishing, a full area a-Si(n) layer is deposited on the rear side. After that an Al_2O_3 passivation is deposited on the front side while the rear a-Si(n) layer is passivated with SiN. After that only the metallization steps remain, which include laser contact opening for the front side, metal screen-printing of Al and Ag for front and rear, respectively and co-firing, which also transforms the a-Si(n) layer into a POLO junction. Therefore, the comparably high efficiency gain comes in combination with a potentially very lean

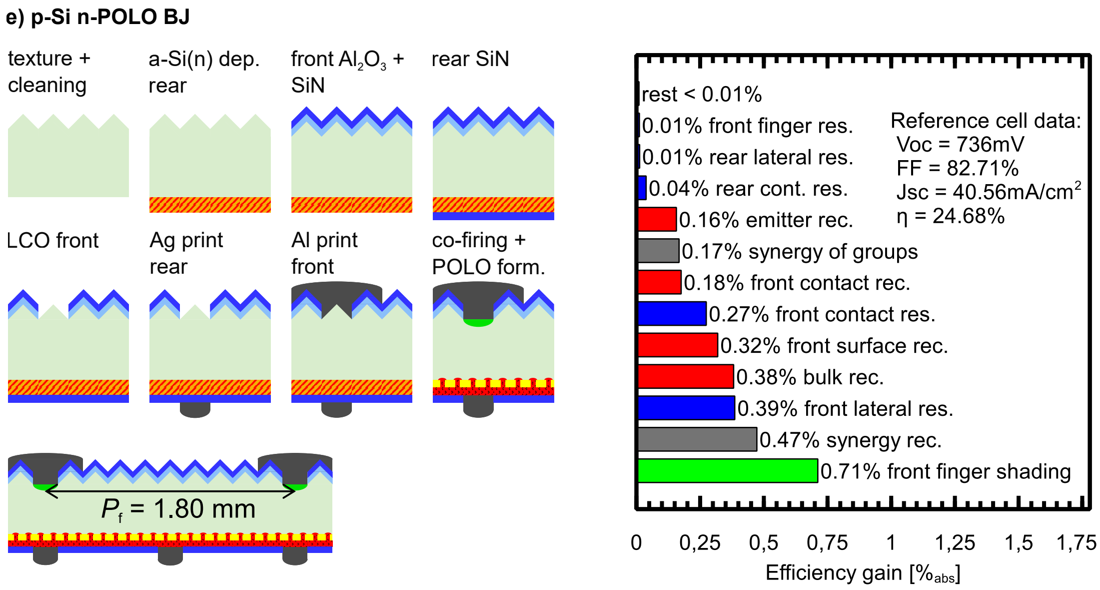

Figure 5.7: Main process steps and SEGA analyses for the p-Si n-POLO BJ structure.

process flow without structuring steps other than LCO and printing. However, printing narrow Al contacts (here 50 μm width) with good electrical properties is a challenging requirement for industrial production nowadays. Nevertheless, recent results have shown that Al fingers down to 50 μm width are indeed possible with screen-printing [84, 85]. Another critical parameter, especially for back junction concepts, is the bulk lifetime. The lifetime used in our analysis was measured on reference samples. The lifetime in the finished cell however, can differ from that on the reference samples due to different gettering processes within the cell process. To estimate the impact of different final lifetimes we run a variation of the bulk lifetime for all p-Si cell concepts in section 5.5.

The **p-Si n-POLO IBC** has the same advantages as the BJ version discussed above yielding a high V_{OC} of 733 mV. This V_{OC} is 3 mV lower than in the BJ version due to the smaller contact pitch on the rear. The smaller contact pitch, however, yields a 0.7% higher FF. In addition, this concept also avoids all shading, which is the main loss in the BJ version. All the effects combined yield an efficiency of 25.5%, which is 1.7% higher than the reference PERC+ cell and 0.8% higher than the BJ version. The remaining losses shown in the SEGA in Fig. 5.8 are dominated by recombination at the front surface, in the bulk and at the Al contact as well as the synergistic gains between them, adding up to 1.64% total. However, the recombination at the Al contacts is the only loss that can be addressed using POLO contacts. The other losses are caused by the already high quality bulk material and surface passivation. A hypothetical process sequence is shown in Fig. 5.8 on the left: After wafer preparation a full area a-Si(n) layer is deposited, which then has to be structured, for example using protective layers

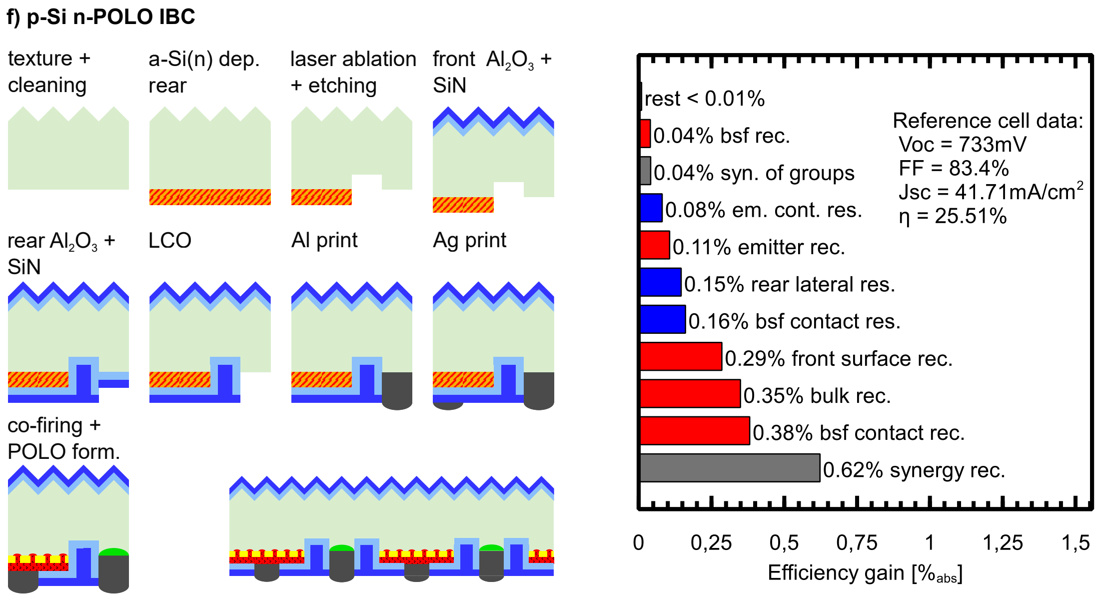

Figure 5.8: Main process steps and SEGA analyses for the p-Si n-POLO IBC structure.

and etching or laser ablation. After structuring, front and rear Al_2O_3/SiN passivation layers are deposited. The remaining steps are to apply the contacts: laser opening the designated base contact areas, Al and Ag print for base and emitter contacts, respectively and co-firing, which also forms the POLO layers. Therefore, the high efficiency gain can be achieved with a process, which may be slightly more complex than the PERC+ process due to the required rear-side structuring.

With conventional Al-BSF contacts a cell structure is ultimately limited to efficiencies around 25.5% as simulated above with the p-Si n-POLO IBC concept . The logical next step is to also replace the Al-BSF contacts with POLO contacts. Therefore, we introduce the p-Si POLO^2 concepts in BJ configuration with and without FSF diffusion and in IBC configuration. The **p-Si POLO² BJ with diffusion** concept yields an efficiency of 24.6%, which is 0.1% lower than for the p-Si n-POLO BJ concept. The optimized front contact pitch is 1.5 mm. The SEGA for this concept is shown in Fig. 5.9. The main loss is the recombination at the FSF with 0.79%, which is 0.47% higher than in the p-Si n-POLO BJ concept. The shading, however, is reduced by 0.19% yielding the simulated efficiency. The main steps of the potential cell process are shown on the left in Fig. 5.9. It requires a double-sided a-Si(n) deposition. The front side is then structured and textured in the regions without POLO. The FSF and the front p-POLO are then formed in a boron diffusion step. Given the efficiency is not higher than that of the p-Si n-POLO BJ concept and the process requires complex structuring steps, this structure is not a promising candidate in terms of industrial integration of POLO junctions.

Omitting the FSF diffusion leads to the **p-Si POLO² BJ** concept, which yields an

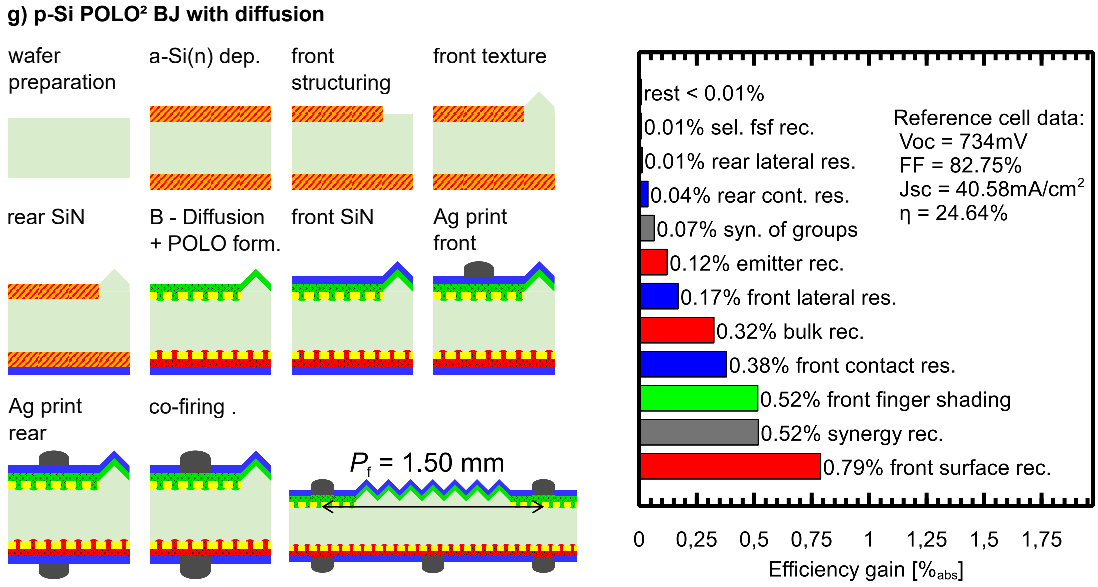

Figure 5.9: Main process steps and SEGA analyses for the p-Si POLO^2 BJ structure with a boron FSF.

efficiency of 25.0%, which is a gain of 1.2% in comparison to PERC+ and 0.3% in comparison with the p-Si n-POLO BJ concept. In comparison to PERC+ this efficiency gain rises mainly from the large voltage gain of 45 mV and in comparison to p-Si n-POLO BJ from the reduced shading and recombination by the Al-BSF contacts. The SEGA for this concept is shown on the right in Fig. 5.10. The shading loss is, with 0.54%, 0.17% lower than in the p-Si n-POLO BJ concept. In addition, the losses due to front contact recombination (-0.18%) and front lateral resistance (-0.17%) are reduced by the POLO contacts and the smaller front contact pitch of 1.45 mm compared to 1.8 mm for the p-Si n-POLO BJ concept. The main process steps for this cell structure are shown on the left in Fig. 5.10. It requires full area a-Si(n) and a-Si(p) depositions on the rear and front, respectively. The front side is then structured and textured, for example using laser oxidation and subsequent texture etching [82] or directly structured deposition using shadow masks [83]. After the structuring steps, only the passivation using SiN and metallization steps remain. Given the high efficiency with a gain of 0.3% compared to p-Si n-POLO BJ concept, this structure is a promising candidate for industrial integration of POLO junction into industrial solar cells. However, structured deposition or structuring after full area deposition of POLO layers is not yet a standard process and poses a technological challenge, which has to be overcome on industrial-scale production for the economic feasibility of this concept.

The **p-Si POLO^2 IBC** version of the POLO^2 concept yields the highest efficiency in our comparison with 25.9%, which is another 0.4% higher than the p-Si n-POLO IBC concept by avoiding the recombination at the Al-BSF contacts and 2.1% higher than

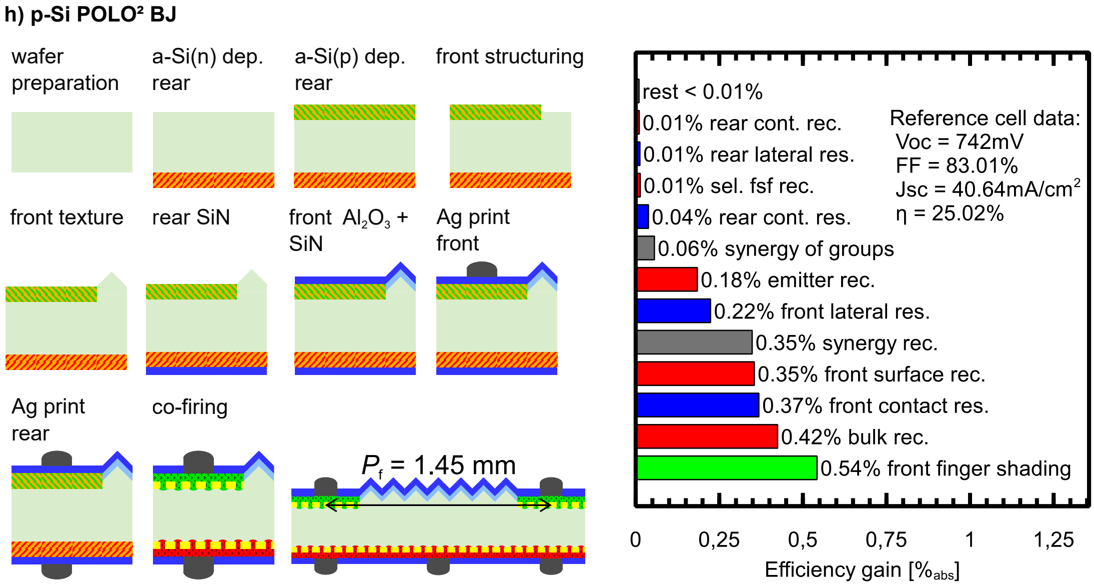

Figure 5.10: Main process steps and SEGA analyses for the p-Si POLO^2 BJ structure without FSF.

PERC+. The SEGA shown on the right side of Fig. 5.11 shows that the remaining losses are caused by recombination at the front surface and in the Si material. Further improvements can, therefore, only be achieved by improving the already very good wafer material and passivation quality. A hypothetical cell process for this concept is shown in Fig. 5.11: It requires structured deposition of a-Si(n) and a-Si(p) prior to Al_2O_3/SiN passivation steps for front and rear respectively and the metallization steps. We included a step for laser contact openings, because the metallization with firing-through pastes on p-POLO is not yet as good as the non firing-through pastes as discussed in section 5.3. The structured POLO layers required for the IBC concept can, for example, be achieved using structured a-Si(n) and a-Si(p) deposition using suitable masks or by depositing a full area a-Si(i) layer and masked doping for both polarities using ion implantation. The latter technique leaves an intrinsic a-Si area between both polarities. This concept has been realized in Ref. 66 with 26.1% efficiency. The industrial integration of this structure seems feasible with moderate process complexity. However, ongoing research is required to develop process sequences for structuring POLO layers and applying good quality screen-printed contacts to p-POLO with industrial type processes. Therefore, both the p-Si POLO^2 BJ without diffusion and the IBC concept are a further step in the development and will require more time for industrial integration than the p-Si n-POLO BJ and p-Si n-POLO IBC concepts.

The concepts discussed above are all based on *p*-type Si, which is the basis for most industrial cells nowadays. However, switching to *n*-type material may prove beneficial in terms of overall recombination due to the higher lifetime. The SEGAs and hypothet-

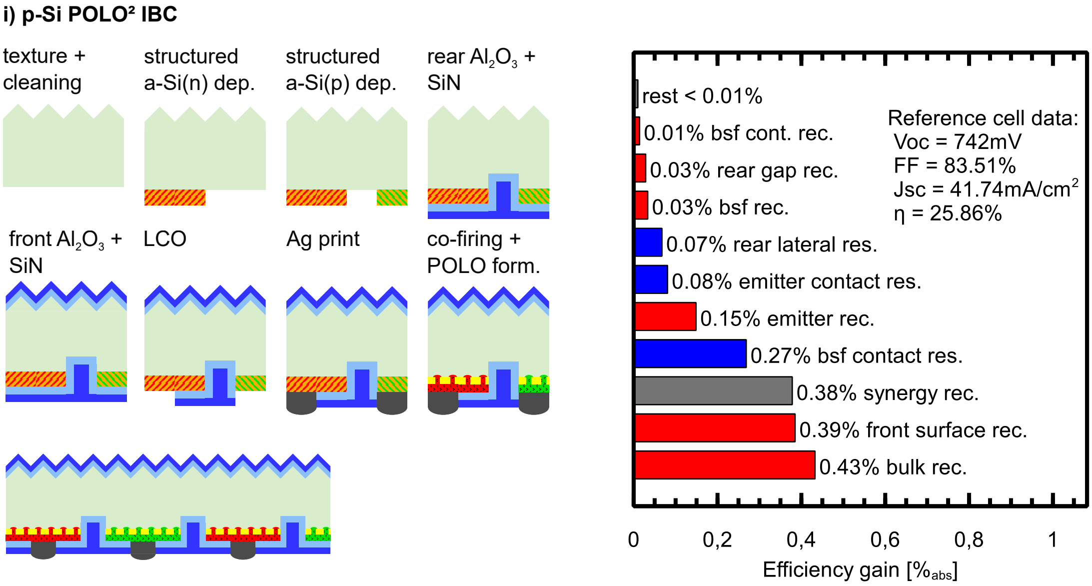

Figure 5.11: Main process steps and SEGA analyses for the p-Si POLO^2 IBC structure.

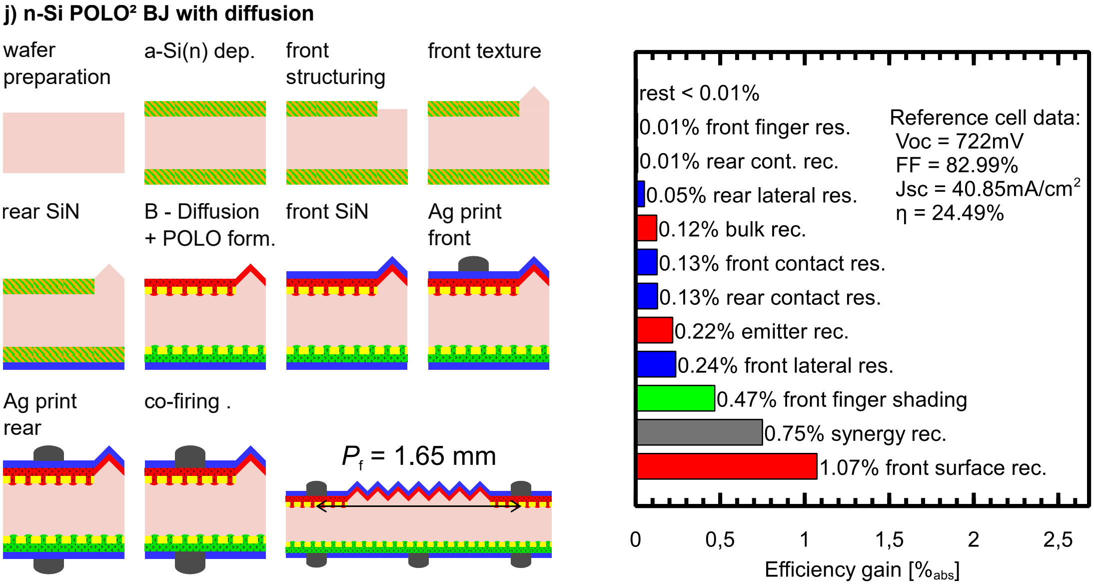

Figure 5.12: Main process steps and SEGA analyses for the n-Si POLO^2 BJ structure with a phosphorus FSF.

ical process flows for the **n-Si POLO^2 BJ with a FSF**, the **n-Si POLO^2 BJ** and the **n-Si POLO^2 IBC** concept are shown in figures 5.12, 5.13 and 5.14, respectively. The efficiencies are all within 0.1% deviation from the respective p-Si structures with

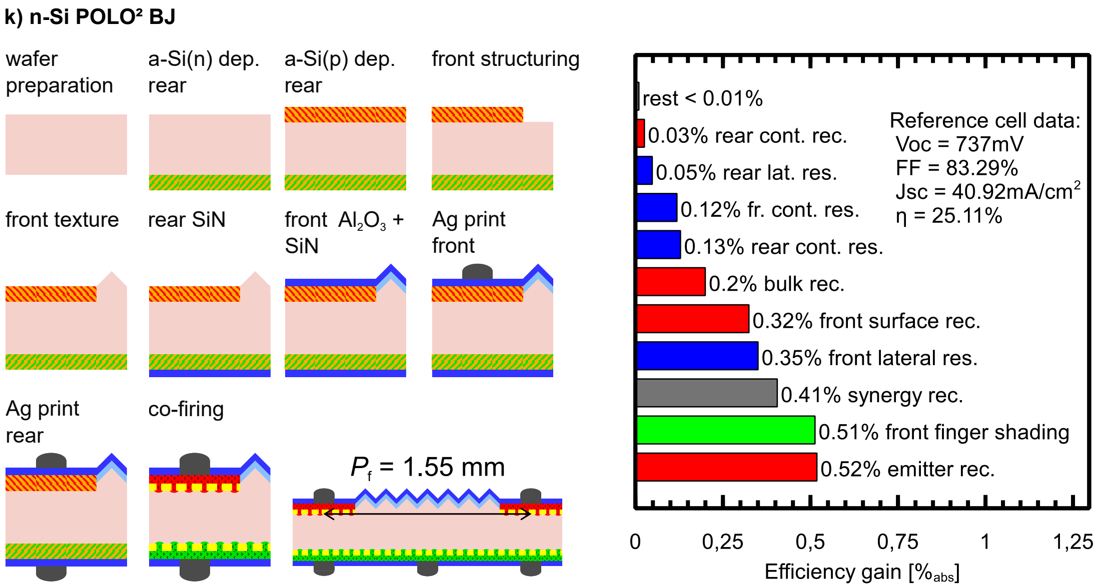

Figure 5.13: Main process steps and SEGA analyses for the n-Si POLO^2 BJ structure without FSF.

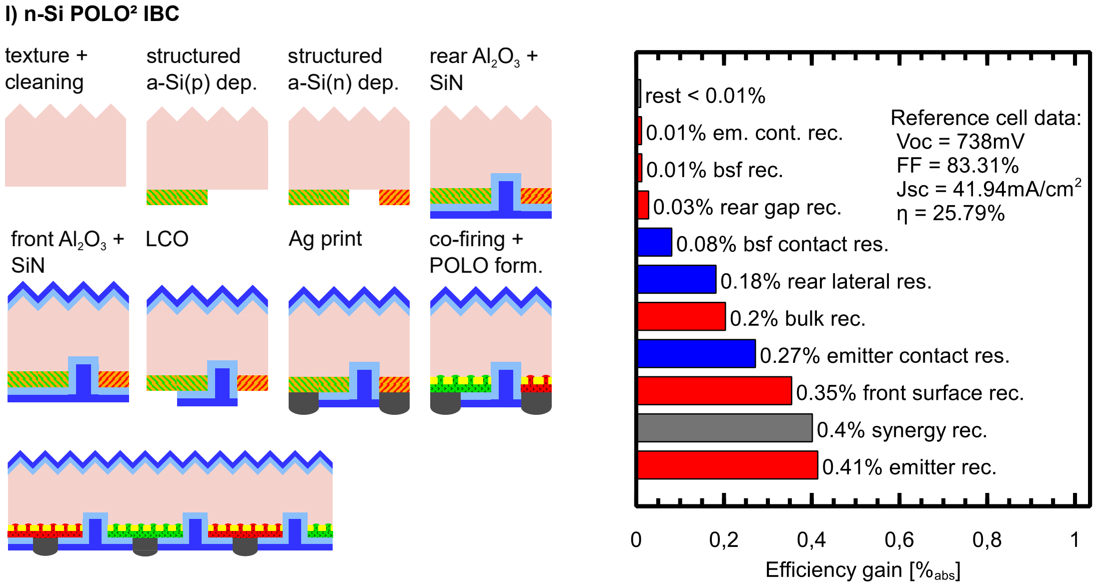

Figure 5.14: Main process steps and SEGA analyses for the n-Si POLO^2 IBC structure.

reversed polarities and the potential process steps are also very similar. The gain due to the increased n-type lifetime is compensated by the slightly higher recombination at the p-POLO emitter. In addition, n-type Si poses additional challenges in industrial production, for example varying resistivity and higher costs, which makes the economic feasibility of this concept questionable given boron-doped Cz-material is already the bases for large fractions of today's industrial solar cell production.

5.5 Bulk lifetime variation

The bulk lifetime is a critical parameter for the evaluation of the benefit of integrating POLO contacts into industrial production. However, the bulk lifetime, especially for B-doped material, is not independent of the cell process due to gettering effects and defect kinetics. Therefore, the final lifetime present in a cell cannot be stated in general. We perform a parameter variation for the bulk lifetime to analyze the efficiency gain of the individual p-Si POLO and POLO^2 concepts in comparison to PERC+ as a function of bulk lifetime. Figure 5.15 shows the efficiency of each cell concept as a function of a fixed, i.e. injection independent, bulk lifetime. The lifetime has only a small effect on the efficiency of both the PERC+ and the p-Si n-POLO FJ concept of less than 0.5% for lifetimes between 500 μs and 10000 μs. The benefit of integrating POLO into p-Si BJ and IBC cells however, depends strongly on the bulk lifetime. For a low lifetime of 500 μs the efficiency gain of the n-POLO BJ and IBC concepts are only 0.2% and 1.0%, respectively and for the POLO^2 BJ and IBC concepts 0.5% and 1.2%, respectively in comparison to PERC+. Compared to the expected efficiency gain at τ_{bulk} = 10000 μs, this is about 1.2% lower for the POLO concepts and 1.4% for the POLO^2 concepts and does probably hardly justify the increased product complexity. Thus, the economic feasibility has to rely on good quality Si and efficient gettering within the process sequence. However, full area POLO layers can serve as gettering layers in high temperature steps [86]. This allows high lifetimes provided the initial impurity concentration in the bulk is kept to a minimum.

5.6 Roadmap for further cell development

Figure 5.16 shows a development strategy for the integration of POLO junctions into industrial Si solar cells. This roadmap is the result of intense discussions on the basis of the simulated efficiencies and the hypothetical cell processes. The p-Si n-POLO BJ and IBC concept pose high efficiency gains of 0.9% and 1.7%, respectively, with potentially lean process flows. In addition, the process flows re-utilize many steps from the standard PERC+ process. Therefore, starting from our PERC+ process, we currently, work on the realization of the p-Si n-POLO IBC cell for the installation of new production lines. The high efficiency in combination with low process complexity makes this concept ideal for the implementation of new production lines in the next years. We simultaneously work on the p-Si n-POLO BJ cell, thereby exploiting the large synergy in the development of both structures. Although the simulated efficiency for the BJ type is 0.8% lower than for

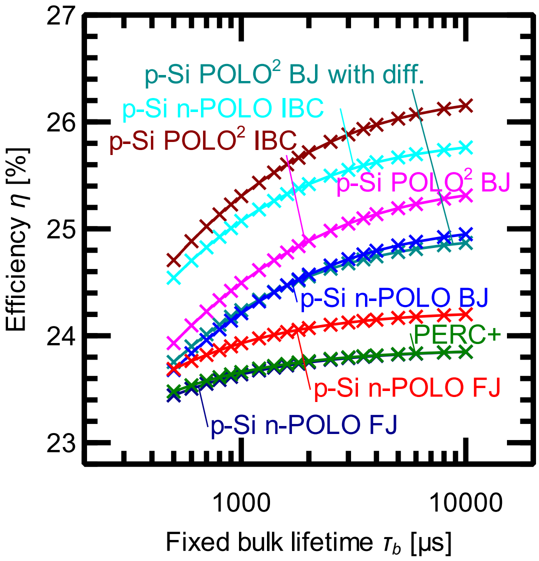

Figure 5.15: Conversion efficiency for the p-Si concepts discussed in this work as a function of an injection independent bulk lifetime.

the IBC type, the front and rear contacted BJ cell is closer to today's industrial PERC+ cells. This makes, for example, module integration of the BJ concept easier. As a next development step we focus on the p-Si POLO^2 concepts both as IBC and BJ structure, which increases the efficiency by another 0.3% to 0.4%, by avoiding the recombination at the Al contacts. We already fabricated a p-Si POLO^2 IBC cell with 26.1% efficiency [9] using lab-scale processes and evaporated contacts. We now work on the realization of this cell concept with industrial-type process flows. The p-Si POLO^2 concepts are, as shown in section 5.4, ultimately only limited by optical performance and material quality and, of course, the intrinsic optical transmission and thermalization losses. To address the intrinsic losses we focus our further research on the development of perovskite tandem cells with the Si POLO^2 concepts as bottom cells for 2 and 3 terminal devices. The analysis of these tandem cells is beyond the scope of this work but we estimate an efficiency of over 33% by adding an approximate 21% efficiency for the top and half of the efficiency simulated here for the bottom cell. We already achieved the experimental verification of important building blocks for the required POLO-process steps for both the n-POLO and POLO^2 concepts [82].

5.7 Conclusion

In this chapter we presented simulations to estimate the efficiency potential of ten different cell types for the integration of POLO junctions into industrial Si cells along with PERC+ and TOPCon reference structures. The ten structures covered concepts where

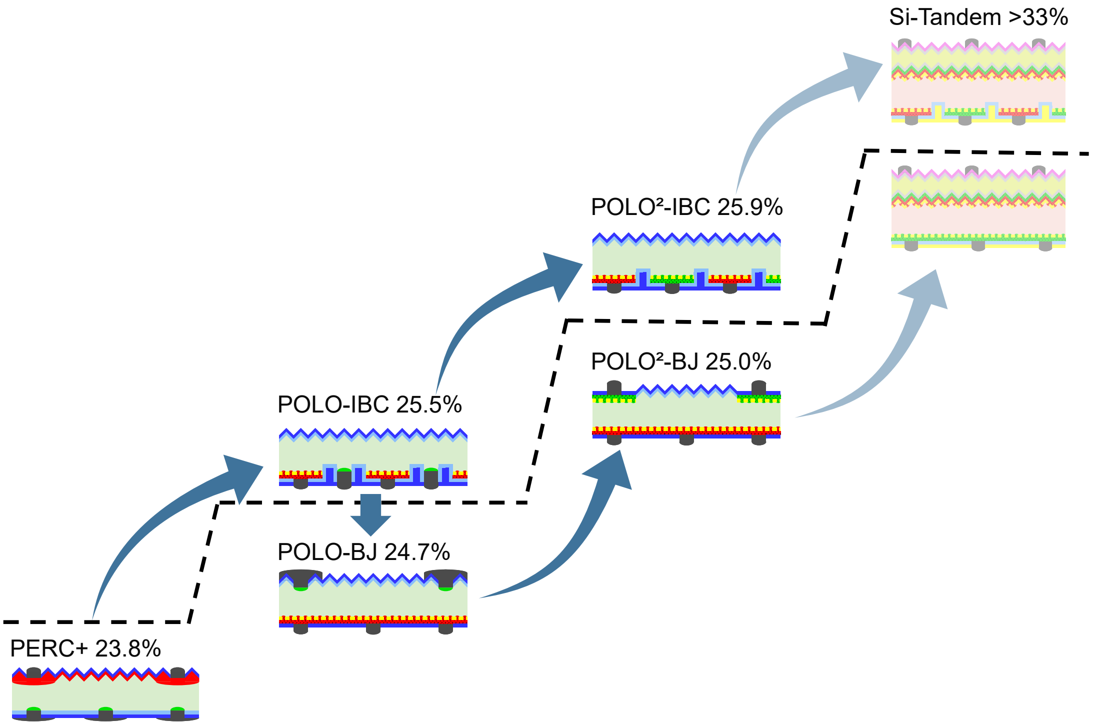

Figure 5.16: Roadmap for further cell development at ISFH: Starting from our PERC+ cells we focus on the p-Si POLO IBC structure for industrial Si cells in the near future. We also exploit the large synergy between the p-Si POLO IBC and BJ concepts to also realize the BJ concept as it has the benefit of being compatible with conventional cell interconnection. As a further development step we work on the p-Si POLO^2 concepts, which require development in terms of POLO structuring and screen-printing on p-poly-Si. The development step after the POLO^2 concepts is to combine the p-Si POLO^2 as bottom cells to perovskite tandem cells. Figure reprinted from [Kruse2020]

the contacts for one polarity are replaced by a POLO junction and concepts with POLO contacts for both polarities. We found that replacing the Al contacts of the PERC+ structure does not yield an efficiency gain due to the increased optical absorption. Applying n-POLO under the front contact of the PERC+ structure yields an efficiency gain of 0.3%, which may not be enough to render this concept economically feasible. Replacing the entire emitter including the contacts by n-POLO in BJ configuration, however yields an efficiency gain of 0.9% compared to PERC+. In addition, this cell structure can hypothetically be manufactured with very lean process flows, which makes this structure a promising candidate for industrial integration of POLO contacts. The main challenge for this concept is the screen-printing of thin Al fingers to avoid large shading losses. The shading is also avoided in the IBC version of this cell concept, which shows an 1.7% higher efficiency than the PERC+ cell. Replacing the Al contacts in the POLO BJ and IBC structures yields an additional efficiency gain of 0.3% to 0.4%. However, the respective structures require structuring of POLO layers and screen-printing on p-POLO layers, which requires further research for industrial implementation. Switching to *n*-type material in the POLO^2 concepts does not yield a significant efficiency gain and, therefore, does not yield any benefit for industrial POLO cells. The p-Si POLO^2 IBC is ultimately only limited by wafer material quality and front surface passivation. A possible way for further improvement is the application of perovskite tandem cells to overcome the intrinsic limitation of Si cells.

6 Summary

The goal of this work was to establish a standard characterization and loss analysis routine for PERC cells and to analyze ways of reducing the major recombination losses in PERC cells with passivating POLO junctions.

Determination of contact recombination parameters

We studied the analysis of contact recombination currents, including the requirements for appropriate test structures, the correct choice of measurement techniques and the evaluation methods for extracting contact recombination parameters from those measurements. We further introduced a new model for correctly describing the injection dependency of contact recombination.

The basis for determining contact recombination parameters is the comparison of the effective lifetime in sample areas with different metallization fractions. We found lateral lifetime inhomogeneities due to passivation or wafer quality to be the major sources of uncertainties. Large inhomogeneities make the determination of meaningful recombination parameters impossible. The reduction of such inhomogeneities is, thus, a primary concern when designing sample structures. Regardless of which method for the determination of $J_{0,\mathrm{cont}}$ is used, the different areas on the sample must be assumed to be independent of each other. We, therefore, developed a new model for calculating the coupling length x_c on which the quasi Fermi levels in a sample with different metallization fractions affect each other. x_c depends on the J_0-ratio between both areas as well as the illumination intensity and the lateral hole and electron conductivities. For an example sample with n-type diffusions in a p-type wafer we found x_c to be in the order of 5 mm. The metallization pattern on such samples must allow an evaluation at least 5 mm from each area boundary. The value of x_c can be calculated with eq. 3.7 on page 34.

The measurement of the spatially resolved effective lifetime is a standard approach in PV-characterization. The application of these techniques to samples with various metallization fractions on one wafer, however, had not been studied before. Therefore, we compared three measurement techniques, commonly used in PV-research, namely PC-PLI, dynamic ILM and dynamically-calibrated static ILM, for their applicability to samples with different metallization fractions. We found the PC-PLI setup with a short pass filter, which excludes optical effects of the rear side from the measurement, to be best suited for this task. We determined the deviation caused by this filter in comparison to the SSPC calibration to less than 5% for metallization fractions smaller than 50%. The dynamic ILM approach yields similar results but with a higher uncertainty and inherent systematic deviations for low and/or injection dependent lifetimes. The static ILM, calibrated with the dynamic measurement, shows a stronger decrease of the apparent lifetime with the metallization fraction than PC-PLI or dynamic ILM. The deviation of the lifetime measured with static ILM compared to PC-PLI was up to 50% for a metallization fraction of 21.6%. We were able to explain this systematic deviation with optical effects on the analyzed IR light caused by the rear-side metallization. The escape probability for IR photons is decreased by the rear-side metallization by a combination of FCA in the highly doped region underneath the metal and a reduced reflectivity at the Si-metal interface.

The extraction of contact recombination parameters with analytical models is only possible in low injection for either full line contacts or point contacts arranged in a square pattern. For this case we checked the applicability of Fischer's model [87] for determining contact recombination parameters and found an excellent agreement to within 5% deviation from numerical modeling. We also introduced a new numerical approach for the analysis of arbitrary contact patterns and injection densities. We found that for the Ag contacts in our work the injection dependency of the measured lifetime is not reproduced by the two commonly used models for recombination currents using either surface recombination velocities or saturation current densities. Therefore, we developed a new model, the J_0/k-model, for describing contact recombination currents, based on the superposition of recombination within the highly doped layer and the recombination at the Si-metal interface. The new model can accurately describe the injection dependency of the recombination at the Ag contacts.

Loss analyses of PERC cells

The free energy loss analysis (FELA) and the synergistic efficiency gain analysis (SEGA) are common approaches for analyzing power losses in solar cells. We compared both approaches and found important differences in the results, especially for recombination losses. For front-side losses the FELA underestimates the losses and the deviation exceeds 20% for large recombination losses of over 0.4 $\mathrm{mW/cm^2}$. For the remaining recombination losses the FELA overestimates the losses by up to 20%. The reason for the deviation is the voltage increase when avoiding recombination, which is not considered in the FELA. The difference between the increase in generated free energy and the increase of energy lost in other recombination channels determines whether the loss is over- or underestimated by the FELA as compared to the SEGA.

We also introduced a new simulation tool to easily perform the simulations required for a SEGA using Quokka. The SEGA-GUI is designed to enable a broad spectrum of users to perform SEGA simulations as no programming is required and all input parameters can be entered or varied using graphical user interfaces.

We have used the new findings on the determination of contact recombination to perform a SEGA analysis of a current PERC+ cell batch. We manufactured and analyzed solar cells and six types of test structures, including standard PV test structures and the newly defined structures for the $J_{0,\mathrm{cont}}$-analysis. We further analyzed the statistical uncertainty of the measured input parameters and determined the uncertainties of the SEGA results using a Monte-Carlo simulation. We found J_{SC} and V_{OC} to reproduce the measured values well ($E_{\mathrm{n}} < 0.3$) whereas the FF was not reproduced well ($E_{\mathrm{n}} > 2.5$). We, therefore, also showed how an analysis of inhomogeneities, in this case of the series resistance, can be used to extend the loss analysis, which is based on a unit cell simulation. In our example we analyzed the finger interruptions on our cell with a local impact analysis [69].

Integration of poly-Si junctions into industrial solar cells

The major losses in PERC solar cells are caused by recombination at the conventional diffusions and contacts. Therefore, we analyzed possible concepts for integrating passivating POLO contacts into industrial solar cells. We based the analysis on input parameters measured mostly at ISFH on samples representing the best lab-scale values available manufactured with industrial-type processes. For the optical properties we employed a ray-tracing approach in which we also took alignment tolerances of structured POLO layers for front-side screen-printing into account. In addition to the expected efficiency and the respective SEGA, we also qualitatively analyzed hypothetical process flows to estimate the process complexity required for manufacturing the respective cell structure. We analyzed ten concepts featuring POLO concepts along with PERC and TOPCon references. Two promising concepts for industrial realization are the p-Si n-POLO BJ (back junction) and IBC (interdigitated back contact) concepts, in which the P-diffused emitter of PERC cells is replaced with n-POLO. The simulated efficiency gains compared to PERC are 0.9% and 1.7%, respectively. Both concepts can potentially be manufactured with lean process flows. The most promising concepts in which both polarities are replaced by POLO are the p-Si POLO^2 BJ and IBC concepts with 1.2% and 2.1% efficiency gain compared to PERC, respectively. Both concepts pose a high efficiency potential and utilize development steps from the p-Si n-POLO BJ and IBC concepts. The potential processes for these structures are also reasonably lean but require further research in structuring POLO layers and contacting p-POLO junctions by screen-printing. These four concepts where combined into a two-stage (one and two polarities POLO) development roadmap for industrial-type POLO cells. The roadmap can be extended with tandem cells, because Si POLO cells are a good choice for a bottom cell in tandem applications.

Bibliography

[1] R. Brendel, S. Dreissigacker, N.-P. Harder, and P. P. Altermatt, “Theory of analyzing free energy losses in solar cells,” *Applied Physics Letters*, vol. 93, no. 17, pp. 3–5, 2008.

[2] J. H. Petermann, “Prozessentwicklung und Verlustanalysen für dünne monokristalline Siliziumsolarzellen und deren Prozessierung auf Modullevel,” Ph.D. dissertation, Fakultät für Mathematik und Physik, Leibniz University Hannover, 2014.

[3] R. Brendel, T. Dullweber, R. Peibst, C. Kranz, A. Merkle, and D. Walter, “Breakdown of the efficiency gap to 29% based on experimental input data and modeling,” *Progress in Photovoltaics: Research and Applications*, vol. 24, no. 12, pp. 1475–1486, dec 2016. [Online]. Available: http://doi.wiley.com/10.1002/pip.2696

[4] “LONGi Solar sets new bifacial mono-PERC solar cell world record at 24.06 percent Solar.” [Online]. Available: https://en.longi-solar.com/home/events/press_detail/id/89.html

[5] “International Technology Roadmap for Photovoltaic (ITRPV),” 2019.

[6] T. Dullweber and J. Schmidt, “Industrial Silicon Solar Cells Applying the Passivated Emitter and Rear Cell (PERC) Concept - A Review,” *IEEE Journal of Photovoltaics*, vol. 6, no. 5, pp. 1366–1381, 2016.

[7] S. Schäfer and R. Brendel, “Accurate Calculation of the Absorptance Enhances Efficiency Limit of Crystalline Silicon Solar Cells With Lambertian Light Trapping,” *IEEE Journal of Photovoltaics*, vol. 8, no. 4, pp. 1156–1158, jul 2018. [Online]. Available: https://ieeexplore.ieee.org/document/8352738/

[8] C. N. Kruse, K. Bothe, B. Lim, T. Dullweber, and R. Brendel, “Synergistic Efficiency Gain Analyses for the Photovoltaic Community: An Easy to Use SEGA Simulation Tool for Silicon Solar Cells,” in *Proceedings of the 35th European Photovoltaic Solar Energy Conference and Exhibition*, 2018, pp. 249–253.

[9] F. Haase, C. Hollemann, S. Schäfer, A. Merkle, M. Rienäcker, J. Krügener, R. Brendel, and R. Peibst, “Laser contact openings for local poly-Si-metal contacts enabling 26.1%-efficient POLO-IBC solar cells,” *Solar Energy Materials and Solar Cells*, vol. 186, pp. 184–193, nov 2018. [Online]. Available: https://linkinghub.elsevier.com/retrieve/pii/S0927024818303076

[10] F. Feldmann, M. Bivour, C. Reichel, M. Hermle, and S. W. Glunz, "Passivated rear contacts for high-efficiency n-type Si solar cells providing high interface passivation quality and excellent transport characteristics," *Solar Energy Materials and Solar Cells*, vol. 120, pp. 270–274, jan 2014. [Online]. Available: https://doi.org/10.1016/j.solmat.2013.09.017

[11] A. W. Blakers, A. Wang, A. M. Milne, J. Zhao, and M. A. Green, "22.8% Efficient Silicon Solar Cell," *Applied Physics Letters*, vol. 55, no. 13, pp. 1363–1365, 1989.

[12] T. Dullweber, C. Kranz, R. Peibst, U. Baumann, H. Hannebauer, A. Fülle, S. Steckemetz, T. Weber, M. Kutzer, M. Müller, G. Fischer, P. Palinginis, and H. Neuhaus, "PERC+: industrial PERC solar cells with rear Al grid enabling bifaciality and reduced Al paste consumption," *Progress in Photovoltaics: Research and Applications*, vol. 24, no. 12, pp. 1487–1498, dec 2016. [Online]. Available: http://doi.wiley.com/10.1002/pip.2712

[13] A. Goetzberger, "Optical confinement in thin Si-solar cells by diffuse back reflectors," in *Proceedings of the 15th IEEE Photovoltaic Specialists Conference*, 1981, pp. 867–870.

[14] M. A. Green, *Solar cells: operating principles, technology, and system applications*, 1982.

[15] J. Zhao and M. A. Green, "Optimized antireflection coatings for high-efficiency silicon solar cells," *IEEE Transactions on Electron Devices*, vol. 38, no. 8, pp. 1925–1934, 1991. [Online]. Available: http://ieeexplore.ieee.org/document/119035/

[16] H. Savin, P. Repo, G. Von Gastrow, P. Ortega, E. Calle, M. Garín, and R. Alcubilla, "Black silicon solar cells with interdigitated back-contacts achieve 22.1% efficiency," *Nature Nanotechnology*, vol. 10, no. 7, pp. 624–628, 2015. [Online]. Available: http://dx.doi.org/10.1038/nnano.2015.89

[17] K. J. Weber, A. W. Blakers, M. J. Stocks, and P. J. Verlinden, "Thin Silicon Cells Using Novel Lase Process," *Solar Energy*, pp. 2–4, 2003.

[18] R. Brendel and M. Ernst, "Macroporous Si as an absorber for thin-film solar cells," *Physica Status Solidi - Rapid Research Letters*, vol. 4, no. 1-2, pp. 40–42, 2010.

[19] J. Greulich, H. Höffler, U. Würfel, and S. Rein, "Numerical power balance and free energy loss analysis for solar cells including optical, thermodynamic, and electrical aspects," *Journal of Applied Physics*, vol. 114, no. 20, 2013.

[20] R. Brendel, "Modeling solar cells with the dopant-diffused layers treated as conductive boundaries," *Progress in Photovoltaics: Research and Applications*, vol. 20, no. 1, pp. 31–43, jan 2012. [Online]. Available: http://doi.wiley.com/10.1002/pip.954

[21] COMSOL AB, "COMSOL Multiphysics," Stockholm, Sweden. [Online]. Available: www.comsol.com

[22] Synopsis, "Sentaurus Device." [Online]. Available: https://www.synopsys.com/silicon/tcad/device-simulation/sentaurus-device.html

[23] A. Fell, "A Free and Fast Three-Dimensional/Two-Dimensional Solar Cell Simulator Featuring Conductive Boundary and Quasi-Neutrality Approximations," *IEEE Transactions on Electron Devices*, vol. 60, no. 2, pp. 733–738, feb 2013. [Online]. Available: http://ieeexplore.ieee.org/document/6387589/

[24] ——, "Quokka manual," 2016. [Online]. Available: https://www2.pvlighthouse.com.au/Resources/Quokka2/QM2/Quokkamanual.htm

[25] A. Goetzberger, J. Knobloch, and B. Voss, *Crystalline Silicon Solar Cells.*

[26] T. Trupke, M. A. Green, P. Würfel, P. P. Altermatt, A. Wang, J. Zhao, and R. Corkish, "Temperature dependence of the radiative recombination coefficient of intrinsic crystalline silicon," *Journal of Applied Physics*, vol. 94, no. 8, pp. 4930–4937, 2003.

[27] A. Richter, F. Werner, A. Cuevas, J. Schmidt, and S. W. Glunz, "Improved parameterization of Auger recombination in silicon," in *Energy Procedia*, vol. 27, Leuven, Belgium, 2012, pp. 88–94. [Online]. Available: http://dx.doi.org/10.1016/j.egypro.2012.07.034

[28] W. Shockley and W. T. Read, "Statistics of the recombinations of holes and electrons," *Physical Review*, vol. 87, no. 5, pp. 835–842, 1952.

[29] K. R. McIntosh and L. E. Black, "On effective surface recombination parameters," *Journal of Applied Physics*, vol. 116, no. 1, 2014.

[30] D. E. Kane and R. M. Swanson, "Measurement of the emitter saturation current by a contactless photoconductivity decay method," in *Conference Record of the 18th IEEE Photovoltaic Specialists Conference*, Las Vegas, 1985, p. 578.

[31] Pv-tools, "LOANA User manual," 2017. [Online]. Available: http://www.pv-tools.de/products/loana-system/loana-start.html

[32] C. N. Kruse, M. Wolf, C. Schinke, D. Hinken, R. Brendel, and K. Bothe, "Impact of Contacting Geometries When Measuring Fill Factors of Solar Cell Current–Voltage Characteristics," *IEEE Journal of Photovoltaics*, vol. 7, no. 3, pp. 747–754, may 2017. [Online]. Available: http://ieeexplore.ieee.org/document/7882654/

[33] H. H. Berger, "Contact resistance on diffused resistors," in *1969 IEEE International Solid-State Circuits Conference. Digest of Technical Papers*, vol. XII. IEEE, 1969, pp. 160–161. [Online]. Available: http://ieeexplore.ieee.org/document/1154702/

[34] ——, “Contact Resistance and Contact Resistivity,” *Journal of The Electrochemical Society*, vol. 119, no. 4, p. 507, 1972. [Online]. Available: http://jes.ecsdl.org/cgi/doi/10.1149/1.2404240

[35] Pv-tools, “TLM-SCAN user manual.” [Online]. Available: www.pv-tools.de

[36] H. Murrmann and D. Widmann, “Current Crowding on Metal Contacts,” *IEEE Trans Elec. Dev.*, vol. ED-16, no. 12, pp. 1022–1024, 1969.

[37] ——, “Messung des Übergangswiderstandes zwischen Metall und Diffusionsschicht in Si-Planarelementen,” *Solid State Electronics*, vol. 12, no. 11, pp. 879–886, 1969.

[38] L. K. Mak, C. M. Rogers, and D. C. Northrop, “Specific contact resistance measurements on semiconductors,” *Journal of Physics E: Scientific Instruments*, vol. 22, no. 5, pp. 317–321, may 1989. [Online]. Available: https://iopscience.iop.org/article/10.1088/0022-3735/22/5/010

[39] S. Eidelloth and R. Brendel, “Analytical Theory for Extracting Specific Contact Resistances of Thick Samples From the Transmission Line Method,” *IEEE Electron Device Letters*, vol. 35, no. 1, pp. 9–11, jan 2014. [Online]. Available: http://ieeexplore.ieee.org/document/6674983/

[40] R. Brendel, “Coupling of light into mechanically textured silicon solar cells: A ray tracing study,” *Progress in Photovoltaics: Research and Applications*, vol. 3, no. 1, pp. 25–38, 1995. [Online]. Available: http://doi.wiley.com/10.1002/pip.4670030103

[41] R. A. Sinton and A. Cuevas, “Contactless determination of current-voltage characteristics and minority-carrier lifetimes in semiconductors from quasi-steady-state photoconductance data,” *Applied Physics Letters*, vol. 69, no. 17, pp. 2510–2512, 1996.

[42] Sinton-Instruments, “Sinton Instruments WCT-120 User Manual,” 2012.

[43] S. Herlufsen, J. Schmidt, D. Hinken, K. Bothe, and R. Brendel, “Photoconductance-calibrated photoluminescence lifetime imaging of crystalline silicon,” *physica status solidi (RRL) - Rapid Research Letters*, vol. 2, no. 6, pp. 245–247, dec 2008. [Online]. Available: http://doi.wiley.com/10.1002/pssr.200802192

[44] J. Müller, K. Bothe, S. Herlufsen, T. Ohrdes, and R. Brendel, “Reverse Saturation Current Density Imaging of Highly Doped Regions in Silicon Employing Photoluminescence Measurements,” *IEEE Journal of Photovoltaics*, vol. 2, no. 4, pp. 473–478, oct 2012. [Online]. Available: http://ieeexplore.ieee.org/document/6226821/

[45] M. Bail, J. Kentsch, R. Brendel, and M. Schulz, “Lifetime mapping of Si wafers by an infrared camera [for solar cell production],” in *Conference Record of the 28th IEEE Photovoltaic Specialists Conference - 2000.* IEEE, 2000, pp. 99–103. [Online]. Available: http://ieeexplore.ieee.org/document/915763/

[46] K. Ramspeck, K. Bothe, J. Schmidt, and R. Brendel, “Combined dynamic and steady-state infrared camera based carrier lifetime imaging of silicon wafers,” *Journal of Applied Physics*, vol. 106, no. 11, p. 114506, dec 2009. [Online]. Available: http://aip.scitation.org/doi/10.1063/1.3261733

[47] K. Ramspeck, S. Reissenweber, J. Schmidt, K. Bothe, and R. Brendel, “Dynamic carrier lifetime imaging of silicon wafers using an infrared-camera-based approach,” *Applied Physics Letters*, vol. 93, no. 10, p. 102104, 2008. [Online]. Available: http://scitation.aip.org/content/aip/journal/apl/93/10/10.1063/1.2972122

[48] B. Min, A. Dastgheib-Shirazi, P. P. Altermatt, and H. Kurz, “Accurate determination of the emitter saturation current density for industrial P-diffused emitters,” *Proceedings of the 29th European Photovoltaic Solar Energy Conference and Exhibition, Amsterdam, The Netherlands*, pp. 463–466.

[49] H. Fischer and W. Pschunder, “Investigation of photon and thermal induced changes in silicon solar cells,” in *Proceedings ofthe 10th IEEE Photovoltaic Specialist Conference*, New York, 1973, pp. 404–411.

[50] V. Steckenreiter, D. C. Walter, and J. Schmidt, “Two-stage permanent deactivation of the boron-oxygen-related recombination center in crystalline silicon,” *Energy Procedia*, vol. 124, pp. 799–805, 2017. [Online]. Available: https://doi.org/10.1016/j.egypro.2017.09.350

[51] D. K. Schroder, R. N. Thomas, and J. C. Swartz, “Free carrier absorption in silicon,” *IEEE Transactions on Electron Devices*, vol. 25, no. 2, pp. 254–261, 1978.

[52] R. Dumbrell, M. K. Juhl, T. Trupke, and Z. Hameiri, “Extracting Surface Saturation Current Density from Lifetime Measurements of Samples with Metallized Surfaces,” in *2018 IEEE 7th World Conference on Photovoltaic Energy Conversion (WCPEC) (A Joint Conference of 45th IEEE PVSC, 28th PVSEC & 34th EU PVSEC).* IEEE, 2018, pp. 3243–3247. [Online]. Available: https://ieeexplore.ieee.org/document/8547720/

[53] ——, “Extracting metal contact recombination parameters from effective lifetime data,” *IEEE Journal of Photovoltaics*, vol. 8, no. 6, pp. 1413–1420, 2018.

[54] A. K. A.L. Blum, J.S. Swirhun, R.A. Sinton, “An Updated Analysis to the WCT-120 QSSPC Measurement System Using Advanced Device Physics,” in *Proceedings of the 28th European Photovoltaic Solar Energy*

Conference. WIP, nov 2013, pp. 1521 – 1523. [Online]. Available: https://www.eupvsec-proceedings.com/proceedings?paper=23364

[55] A. Kimmerle, J. Greulich, and A. Wolf, "Carrier-diffusion corrected J0-analysis of charge carrier lifetime measurements for increased consistency," *Solar Energy Materials and Solar Cells*, vol. 142, pp. 116–122, 2015. [Online]. Available: http://dx.doi.org/10.1016/j.solmat.2015.06.043

[56] B. Fischer, "Loss analysis of crystalline silicon solar cells using photoconductance and quantum efficiency measurements," Ph.D. dissertation, Universtät Konstanz, 2003. [Online]. Available: http://en.scientificcommons.org/31058651

[57] B. Gelmont, M. Shur, and R. Mattauch, "Disk and stripe capacitances," *Solid-State Electronics*, vol. 38, no. 3, pp. 731–734, mar 1995. [Online]. Available: http://linkinghub.elsevier.com/retrieve/pii/003811019400140B

[58] H. Plagwitz, "Surface passivation of crystalline silicon solar cells by amorphous silicon films," Ph.D. dissertation, Leibniz Universität Hannover, 2007.

[59] S. Karmalkar, P. V. Mohan, H. P. Nair, and R. Yeluri, "Compact models of spreading resistances for electrical/thermal design of devices and ICs," *IEEE Transactions on Electron Devices*, vol. 54, no. 7, pp. 1734–1743, 2007.

[60] R. Cox and H. Strack, "Ohmic contacts for GaAs devices," *Solid-State Electronics*, vol. 10, no. 12, pp. 1213–1218, dec 1967. [Online]. Available: https://linkinghub.elsevier.com/retrieve/pii/0038110167900639

[61] S. Meier, S. Unmüßig, A. Brand, P. Saint-Cast, T. Fellmeth, A. Wolf, and S. W. Glunz, "Experimental verification of internal resistance models for PERT-type solar cells," *Energy Procedia*, vol. 124, pp. 881–890, 2017. [Online]. Available: https://doi.org/10.1016/j.egypro.2017.09.248

[62] C. N. Kruse, K. Bothe, and R. Brendel, "Comparison of Free Energy Loss Analysis and Synergistic Efficiency Gain Analysis for PERC Solar Cells," *IEEE Journal of Photovoltaics*, vol. 8, no. 3, pp. 683 – 688, 2018. [Online]. Available: http://ieeexplore.ieee.org/document/8301422/

[63] B. Lim, T. Brendemühl, T. Dullweber, and R. Brendel, "Loss analysis of n-type passivated emitter rear totally diffused back-junction silicon solar cells with efficiencies up to 21.2%," *IEEE Journal of Photovoltaics*, vol. 6, no. 2, pp. 447–453, 2016. [Online]. Available: http://ieeexplore.ieee.org/lpdocs/epic03/wrapper.htm?arnumber=7400919

[64] F. Haase, F. Kiefer, S. Schäfer, C. N. Kruse, J. Krügener, R. Brendel, and R. Peibst, "Interdigitated back contact solar cells with polycrystalline silicon on oxide passivating contacts for both polarities," *Japanese Journal of Applied Physics*, vol. 56, no. 8S2, p. 08MB15, aug 2017.

[65] C. Messmer, A. Fell, F. Feldmann, N. Wöhrle, J. Schön, and M. Hermle, "Efficiency roadmap for evolutionary upgrades of perc solar cells by topcon: Impact of parasitic absorption," *IEEE Journal of Photovoltaics*, vol. 10, no. 2, pp. 335–342, 2020.

[66] C. Hollemann, F. Haase, S. Schäfer, J. Krügener, R. Brendel, and R. Peibst, "26.1%-efficient POLO-IBC cells: Quantification of electrical and optical loss mechanisms," *Progress in Photovoltaics: Research and Applications*, vol. 27, no. 11, pp. 950–958, nov 2019. [Online]. Available: https://onlinelibrary.wiley.com/doi/abs/10.1002/pip.3098

[67] W. Wöger, "Remarks on the En-criterion used in measurement comparisons," *PTB-Mitteilungen*, vol. 109, no. 1, pp. 19–27, 1999.

[68] T. Trupke, E. Pink, R. A. Bardos, and M. D. Abbott, "Spatially resolved series resistance of silicon solar cells obtained from luminescence imaging," *Applied Physics Letters*, vol. 90, no. 9, pp. 1–4, 2007.

[69] D. Hinken, K. Bothe, and R. Brendel, "Impact of lateral variations on the solar cell efficiency," in *Proceedings of the 25th European Photovoltaic Solar Energy Conference*, no. September, 2010.

[70] B. Min, M. Müller, H. Wagner, G. Fischer, R. Brendel, P. P. Altermatt, and H. Neuhaus, "A Roadmap Toward 24% Efficient PERC Solar Cells in Industrial Mass Production," *IEEE Journal of Photovoltaics*, vol. 7, no. 6, pp. 1541–1550, nov 2017. [Online]. Available: http://ieeexplore.ieee.org/document/8048349/

[71] A. Richter, J. Benick, F. Feldmann, A. Fell, M. Hermle, and S. W. Glunz, "n-Type Si solar cells with passivating electron contact: Identifying sources for efficiency limitations by wafer thickness and resistivity variation," *Solar Energy Materials and Solar Cells*, vol. 173, no. May, pp. 96–105, dec 2017. [Online]. Available: dx.doi.org/10.1016/j.solmat.2017.05.042

[72] K. Yoshikawa, W. Yoshida, T. Irie, H. Kawasaki, K. Konishi, H. Ishibashi, T. Asatani, D. Adachi, M. Kanematsu, H. Uzu, and K. Yamamoto, "Exceeding conversion efficiency of 26% by heterojunction interdigitated back contact solar cell with thin film Si technology," *Solar Energy Materials and Solar Cells*, vol. 173, no. June, pp. 37–42, dec 2017. [Online]. Available: http://dx.doi.org/10.1016/j.solmat.2017.06.024

[73] Y. Chen, "presented at the PV-CellTech conference," Kuala Lumpur, Malaysia, 2019.

[74] P. Jäger, U. Baumann, and T. Dullweber, "Impact of the thermal budget of the emitter formation on the pFF of PERC+ solar cells," in *AIP Conference Proceedings*, vol. 2147, no. 1, 2019, p. 140005. [Online]. Available: http://aip.scitation.org/doi/abs/10.1063/1.5123892

[75] V. D. Mihailetchi, H. Chu, J. Lossen, and R. Kopecek, "Surface Passivation of Boron-Diffused Junctions by a Borosilicate Glass and in Situ Grown Silicon Dioxide Interface Layer," *IEEE Journal of Photovoltaics*, vol. 8, no. 2, pp. 435–440, 2018.

[76] M. Dahlinger, S. J. Eisele, P. C. Lill, J. R. Kohler, and J. H. Werner, "Full area laser doped boron emitter silicon solar cells," in *Conference record of the 38th IEEE Photovoltaic Specialists Conference.* IEEE, jun 2012, pp. 1029–1031. [Online]. Available: http://ieeexplore.ieee.org/document/6317778/

[77] F. Haase, C. Hollemann, S. Schäfer, J. Krügener, R. Brendel, and R. Peibst, "Transferring the record p-type Si POLO-IBC cell technology towards an industrial level," Chicago, IL, USA, 2019.

[78] E. Lohmüller, S. Lohmüller (née Werner), N. Wöhrle, U. Belledin, and A. Wolf, "BBr3 diffusion with second deposition for laser-doped selective emitters from borosilicate glass," *Solar Energy Materials and Solar Cells*, vol. 186, pp. 291–299, nov 2018. [Online]. Available: https://doi.org/10.1016/j.solmat.2018.06.042

[79] J. Engelhardt, A. Frey, S. Fritz, G. Micard, S. Riegel, G. Hahn, and B. Terheiden, "Contact Formation on Boron Doped Silicon Substrates from Passivating PECV-Deposited Dielectric Doping Layers with Anti-Reflective Properties by Screen-Printing Ag Pastes for High-Efficiency N-Type Silicon Solar Cells," in *Proceedings of the 31st European Photovoltaic Solar Energy Conference and Exhibition*, 2015, pp. 351 – 354.

[80] Y. Larionova, R. Peibst, and R. Brendel, "Screen print- and PVD based metallization schemes for POLO junctions," Konstanz, 2017.

[81] S. Mack, J. Schube, T. Fellmeth, F. Feldmann, M. Lenes, and J.-M. Luchies, "Metallisation of Boron-Doped Polysilicon Layers by Screen Printed Silver Pastes," *physica status solidi (RRL) - Rapid Research Letters*, vol. 11, no. 12, p. 1700334, 2017.

[82] R. Peibst, C. Kruse, S. Schäfer, V. Mertens, S. Bordihn, T. Dullweber, F. Haase, C. Hollemann, B. Lim, B. Min, R. Niepelt, H. Schulte-Huxel, and R. Brendel, "For none, one, or two polarities—How do POLO junctions fit best into industrial Si solar cells?" *Progress in Photovoltaics: Research and Applications*, p. pip.3201, nov 2019. [Online]. Available: https://onlinelibrary.wiley.com/doi/abs/10.1002/pip.3201

[83] T. Dullweber, C. Kruse, F. Haase, M. Rudolph, M. Stöhr, P. Jäger, R. Peibst, and R. Brendel, “PERC + POLO solar cells minimizing carrier recombination at the Ag front contact with simulated efficiency potential up to 23 . 8 %,” in *29th International Photovoltaic Sience and Engineering Conference*, 2019.

[84] K. Tsuji, S. Suzuki, N. Morishita, T. Kuroki, M. Nakahara, M. Dhamrin, Z.-W. Peng, T. Buck, and N. Usami, “Fine line Al printing on narrow point contact opening for front side metallization,” in *AIP Conference Proceedings*, vol. 2147, no. August, 2019, p. 040019. [Online]. Available: http://aip.scitation.org/doi/abs/10.1063/1.5123846

[85] T. Dullweber, H. Hannebauer, B. Lim, P. Jäger, M. Rudolph, H. Schulte-Huxel, F. Haase, K. Bothe, M. Köntges, S. Kajari-Schröder, R. Peibst, and R. Brendel, “Bifacial PERC+ solar cells with conversion efficiencies above 22% and high energy yield,” Shanghai, China, 2018.

[86] J. Krügener, F. Haase, M. Rienäcker, R. Brendel, H. Osten, and R. Peibst, “Improvement of the SRH bulk lifetime upon formation of n-type POLO junctions for 25% efficient Si solar cells,” *Solar Energy Materials and Solar Cells*, vol. 173, pp. 85–91, dec 2017. [Online]. Available: https://linkinghub.elsevier.com/retrieve/pii/S0927024817302817

[87] B. Fischer, J. Müller, and P. P. Altermatt, “A simple emitter model for quantum efficiency curves and extracting the emitter saturation current,” in *28th European Photovoltaic Solar Energy Conference and Exhibition*, 2013.

List of publications

Refereed journal papers

1. R. Peibst, C. N. Kruse, S. Schäfer, V. Mertens, S. Bordihn, T. Dullweber, F. Haase, C. Hollemann, B. Lim, B. Min, R. Niepelt, H. Schulte-Huxel and R. Brendel, "For none, one or two polarities – how do POLO junctions fit best into industrial Si solar cells?", *Progress in Photovoltaics: Research and Applications*, 2019
2. C. N. Kruse, K. Bothe, and R. Brendel, "Comparison of Free Energy Loss Analysis and Synergistic Efficiency Gain Analysis for PERC Solar Cells", *IEEE Journal of Photovoltaics*, vol. 8, no. 3, pp. 683–688, 2018.
3. F. Haase, F. Kiefer, S. Schäfer, C. N. Kruse, J. Krügener, R. Brendel, and R. Peibst, "Interdigitated back contact solar cells with polycrystalline silicon on oxide passivating contacts for both polarities", *Japanese Journal of Applied Physics*, vol. 56, no. 8S2, p. 08MB15, 2017.
4. C. N. Kruse, M. Wolf, C. Schinke, D. Hinken, R. Brendel, and K. Bothe, "Impact of Contacting Geometries When Measuring Fill Factors of Solar Cell Current-Voltage Characteristics", *IEEE Journal of Photovoltaics*, vol. 7, no. 3, pp. 747-754, 2017.
5. (not in context of dissertation:) B. Dupé, C. N. Kruse, T. Dornheim and S. Heinze, "How to reveal metastable skyrmionic spin structures by spin-polarized scanning tunneling microscopy", *New J. Phys.*, vol. 18, no. 5, p.055015, 2016

Papers presented at international conferences

1. T. Dullweber, C. N. Kruse, F. Haase, M. Rudolph, M. Stöhr, P. Jäger, R. Peibst and R. Brendel, "PERC+ POLO solar cells minimizing carrier recombination at the Ag front contact with simulated efficiency potential up to 23.8%," *29th International Photovoltaic Sience and Engineering Conference*, 2019.
2. M. Rudolph, C. N. Kruse, H. Wolter, B. Wolpensinger, U. Baumann, S. Bräunig, M. Ripke, T. Falcon, R. Brendel and T. Dullweber, "PERC+ solar cells with screen-printed dashed Ag front contacts", *AIP Conference Proceedings*, vol. 2147, no. 1, p.060001, 2019

3. C. N. Kruse, K. Bothe, B Lim, T. Dullweber and R. Brendel, "Synergistic efficiency gain analysis for the photovoltaic community: An easy to use SEGA simulation tool for silicon solar cells", *Proceedings of the 35th European Photovoltaic Solar Energy Conference and Exhibition*, pp. 249-253, 2018
4. R. Brendel, C. Kruse, A. Merkle, H. Schulte-Huxel, F. Haase and R. Peibst, "Screening Carrier Selective Contact Combinations for Novel Crystalline Si Cell Structures", *Proceedings of the 35th European Photovoltaic Solar Energy Conference and Exhibition*, pp. 39-46, 2018
5. C. N. Kruse, M. Wolf, C. Schinke, D. Hinken, R. Brendel, and K. Bothe, "Impact of contacting geometries on measured fill factors", *Energy Procedia*, vol. 124, pp. 84-90, 2017.
6. B. Min, C. N. Kruse, C. Schinke, M. Wolf, M. Müller, H. Sträter, M. Wagner, K. Bothe, and R. Brendel, "Identifying the location of recombination from voltage-dependent quantum efficiency measurements", *Energy Procedia*, vol. 124, pp. 120-125, 2017.

Danksagung

Ich möchte mich an dieser Stelle bei allen bedanken, die zum Gelingen dieser Arbeit beigetragen haben:

Prof. Dr. Rolf Brendel für die Möglichkeit am ISFH zu promovieren, für die sehr gute Betreuung und viele angeregte Diskussionen zu spannenden physikalischen Problemen.

Prof. Dr. Rolf Haug und Prof. Dr. Armin Aberle für die Übernahme des Korreferats.

Prof. Dr. Olaf Lechtenfeld für die Übernahme des Prüfungsvorsitzes.

Karsten Bothe für die grossartige wissenschaftliche Betreuung, viele spannende Diskussionen und eine sehr gute Arbeitsatmosphäre in der Charakterisierungsgruppe.

Carsten Schinke für viele wissenschaftliche Diskussionen, die Unterstützung in vielen Bereichen der täglichen Arbeit und die sehr gute Arbeitsatmosphäre in der Simulationsgruppe.

Sören Schäfer für die Durchführung und viele Diskussionen zu den ray-tracing Simulationen.

Verena Mertens für die Unterstützung bei der Planung von Experimenten, Hilfe bei Messungen und die vielen Diskussionen zur PERC Charakterisierung.

Robby Peibst für die Anregung der Roadmap Simulationen und die vielen Diskussionen zu diesem Thema.

Felix Haase für die vielen Ideen, Vorschläge und Diskussionen zu möglichen Zellstrukturen und deren Herstellung.

Byungsul Min für viele Diskussionen und Anregungen zu verschiedensten Simulationen und Programmen.

Davin Hinken bei der Hilfe und Anregungen zu verschiedenen Messauswertungen und für den Support mit SCAN.

Hannes Wagner-Mohnsen für die gute Zusammenarbeit in GENESIS-Projekt und den vielen anderen kleineren Projekten.

Thorsten Dullweber für die Diskussionen zur PERC Optimierung .

Der Gruppe "Industrielle Solarzellen" für die Zell- und Probenprozessierung .

Martin Wolf für die Unterstützung bei zahlreichen "ungewöhnlichen" Messvorhaben und den Support an der LOANA und der ILM.

Boris Veith-Wolf, Dennis Bredemeier und Dominic Walter für die Diskussionen zu Lebensdauern, Volumendefekten und Oberflächenpassivierung.

Bianca Lim für viele Anregungen zur Analyse der Kontaktrekombination.

Robert Witteck, David Hinken, Carsten Schinke, Sören Schäfer und Karsten Bothe für das oft kurzfristige Korrekturlesen der Arbeit.

Allen ISFH-Mitarbeitern und den "Uni-Leuten" für eine tolle Arbeitsatmosphäre, die unkomplizierte Zusammenarbeit, die Grillabende und das "wöchentliche" Fussballspielen.

Der Charakterisierungs-Gruppe und der Simulations-Gruppe für viele gute Ideen und Anregungen zu den grösseren und kleineren Problemen, die während der Arbeit auftraten.

Bei meiner Familie für die tolle Unterstützung nicht nur während der Doktorarbeit, sondern auch davor.

Mein besonderer Dank gilt Merle für die super Unterstützung und Motivation, für ein offenes Ohr und die Ablenkung vom Arbeitsalltag.